Order Number 9009757

Studies of the mechanical properties of solids with random porosity

Li, Rong, Ph.D.

City University of New York, 1989

U·M·I
300 N. Zeeb Rd.
Ann Arbor, MI 48106

STUDIES OF THE MECHANICAL PROPERTIES OF SOLIDS WITH RANDOM POROSITY

by

RONG LI

A dissertation submitted to the Graduate Faculty in Physics in partial fulfillment of the requirements for the degree of Doctor of Philosophy, The City University of New York.

1989

This manuscript has been read and accepted for the Graduate Faculty in Physics in satisfaction of the dissertation requirement for the degree of Doctor of Philosophy.

9-13-89 — Date

Arthur Paskin — Chair of Examining Committee

9-18-89 — Date

Joel I. Gersten — Executive Officer

Karl Sieradzki

Arthur C. Damask

Narciso Garcia

Micha Tomkiewicz

Supervisory Committee

The City University of New York

Abstract

STUDIES OF THE MECHANICAL PROPERTIES

OF SOLIDS WITH RANDOM POROSITY

by

Rong Li

Advisor: Professor Arthur Paskin

The 2-D and 3-D mechanical behavior of a solid with random porosity was studied experimentally. For 2-D samples, the elasticity and fracture stress could be well described by an effective modulus derived from an effective medium theory (EMT) in the dilute crack region. The elastic modulus and fracture stress decrease linearly with increasing ϕ, the fraction of the missing bonds in the system where $E \sim (1-\alpha\phi)$, with $\alpha \approx 3.3$ for honeycomb lattice and ≈ 2 for square lattice. According to EMT, the initial slope of the fracture stress as a function of ϕ should be 3.6 for honeycomb lattice and 1.8 for square lattice. The fracture behavior of the system can be identified by the α value in the Weibull distribution, which describes the dispersion of crack-size distributions of the specimen. In the scaling region, the experimental results show that the elastic modulus exponent, f, equals 3.1 ± 0.2. The fracture exponent, F, obtained by applying the percolation concept to the Griffith relation, agrees with our experimental results which are 1.7 and 1.8 for honeycomb lattice and square lattice, respectively. The 3-D experiment involved a unique technique to prepare the specimen for a three-point bend test, namely an electrochemical dissolution process followed by an annealing process to form self-similar porous structures. The samples with larger-scale porosity had a lower Young's modulus and a higher fracture stress than samples with finer-scale porosity. In addition to these analytical differences in the sample, we discovered the existence of a ductile to brittle transition. We believe that this transition is effected by the size of the sample.

ACKNOWLEDGEMENTS

I would like to express my gratitude to my mentor Professor Karl Sieradzki for his guidance and encouragement during this study. His great efforts are highly appreciated. I wish to thank Professor Arthur Paskin for being my advisor, and for his continued concern with my education and thesis project over the past four years. I also wish to thank Professors Arthur Damask, Narciso Garcia , and Micha Tomkiewicz for their help, suggestions and discussion of this work. The help of Kenneth Sutter in preparing samples and the help from Robert Sabatini in characterizing and analyzing the samples is greatly appreciated. The assistance and help with mechanical testing from Donald Horne is acknowledged.

I would like to thank Dr. Reed Corderman for his valuable suggestion on data manipulation and I especially thank Janet Sieradzki for her kind concern. Dr. Hugh Isaacs, Dr. Kelvin Lynn, and colleagues working in Building 480 at BNL provided me with an excellent environment to write this thesis. Their constant encouragement and concern will be remembered. I am grateful to Dr. Avril Woodhead for reading and revising this manuscript. Professor Boxi Wu is thanked for helping me to come to the United States for my graduate studies. Finally, I would like to thank my parents for their full understanding and support.

This work was supported by the U.S. Dept. of Energy, Basic Energy Science, Division of the Material Sciences under contract No. DE-AC02-76CH00016.

TABLE OF CONTENTS

LIST OF FIGURES

LIST OF TABLES

1. INTRODUCTION

The purpose of this work was to develop a better understanding of the mechanical properties of a solid with random porosity. The 2-D and 3-D mechanical behavior of a solid with random porosity was studied experimentally.

We used two models of different configurations with random porosity to investigate the fracture behavior in two dimensions; to study materials in three dimensions, three-point bend tests of porous gold solids prepared by selective dissolution (dealloying) were carried out.

The mechanical properties of materials dependent on many factors [1-7], such as the proportion of the constituent elements in a solid system, the type of phases which are present, on prior deformation, and on environmental effects. Heterogeneous structures which contain weak or brittle constituents are unsatisfactory, since they provide continuous paths of easy fracture. A dispersed second phase embedded in a matrix can either harden or soften the matrix, and this technique has had wide industrial applications.

Heterogeneous materials can differ significantly in composition, mechanical, and physical properties. For example, in an ordinary plain carbon steel, the matrix is principally composed of α-Fe hardened by Fe_3C, In general, the greater the proportion of Fe_3C in the α-Fe matrix, the higher is the fracture strength of the steel. The heating of a solid near its melting temperature and subsequent quenching will produce vacancy clusters, forming a porous structure on an atomic scale, which can dramatically change the mechanical properties of the solids. Irradiation of a solid with charged heavy particles also produces vacancy clusters or disks inside materials. When the radiation is made up of alpha particles, helium gas can be entrapped in the solid to form a second phase, composed of vacancy disks. When such vacancy clusters are large enough,

they may collapse to form sessile dislocation rings which are strong obstacles to dislocation motion, and thus can contribute to hardening.

Several methods were used to analyze the experimental results: modified Griffith relations [1-7], which count the finite sample size with the array of the cracks of equal length and the equal center spacing oriented perpendicular to the tensile axis, a method based on the quasi thermodynamical equilibrium; statistical methods [8]; effective medium theory [9] which assumes that a single crack in the sample "sees" the whole sample; and the percolation theory [10, 11].

Three-point bend tests of porous gold beams prepared by an electrochemical dissolution process were used to study the elastic modulus and the fracture behavior of porus solids in three dimensions. Selective dissolution of silver-gold (Ag-Au) alloys in perchloric acid leaves porous Au in the solid. The distribution of the porosity could be altered by controlling the annealing temperatures and times. Samples with various porosities were characterized by scanning electron microscopy, digital image analysis, and energy dispersion X-ray analysis.

Characterization of the samples suggested that virtually all of the Ag was removed from the Ag-Au alloys by the dissolution process. Annealing of the as-corroded material led to self-similar coarsening of the de-alloyed structure. Mechanical testing showed that samples with larger-scale porosity had a lower Young's modulus and a higher fracture stress than samples with finer-scale porosity. In addition to these analytical differences in the sample, we discovered that there was a ductile to brittle transition that was dependent on the porosity of the sample.

The properties of porous solids are discussed and explained in terms of subtle differences in the ligament element (or pore) strength distribution and a brittle-ductile transition driven by the sample's size.

2. LITERATURE REVIEW

2.1 Concept of Griffith Energy Balance

Early in this century, Griffith [1-8] set up a model for a crack system in terms of a reversible thermodynamic process and developed the concept of an energy-balance. The Griffith energy criterion for fracture states that crack growth can occur if the energy required to form an increment of crack advance, da, can be delivered by the loading system. For a plate of unit thickness the condition for crack growth becomes [6]:

$$d(U_E - W_L + U_s)/da = 0 \quad \text{or} \quad d(W_L - U_E)/da = dU_s/da \tag{2.1}$$

where U_E is the elastic energy (strain potential) contained in the plate, W_L is the work performed by the external force, and U_s is the energy for crack formation. The idea of a reversible thermodynamic process is as follows.

Start with a crack-free state and assume that the elastic field is known. Make a cut along the ultimate crack plane, impose traction equal and opposite to the stresses already there to maintain the system in equilibrium. The only energy involved is the amount U_s supplied by the cutting process in creating the crack surface. Slowly relax the imposed traction to 0 (so that no kinetic energy is involved), then the mechanical energy released in achieving this final state is $(U_E - W_L)$. This process is reversible.

For a system with the fixed ends and for a system with free ends and constant load, the changes in mechanical energy during crack extension are the same:

$$\Delta(U_E - W_L) = -1/2 \cdot F^2 \cdot \Delta C \qquad (2.2)$$

where F is the applied load and C is the elastic compliance of the system.

When the plate has fixed ends the external load cannot do work; therefore the energy required for crack growth must then be delivered as a release of elastic energy. However, if the ends of the plate are free to move during crack extension, work is done by the external load. In this case, the elastic energy of the plate increases instead of decreasing.

Crack extension can occur when the energy supplied is equal to the energy required for crack growth. In a brittle material which fractures reversibly the energy for crack growth is the surface energy required to form the new free surfaces, *i.e.*:

$$U_s = 2\gamma a \qquad \text{and} \qquad R = dU_s/da = 2\gamma \qquad (2.3)$$

where R is the crack resistant force, which leads to:

$$\sigma_c = (2\gamma E/\pi a)^{1/2} \qquad (2.4)$$

the well-known Griffith criterion. Where σ_c is the critical value of stress to fracture a plate with a crack of size 2a, E is the elastic modulus of the plate.

Griffith derived his equation (2.4) for glass, which is a very brittle material. Therefore, he assumed that R consisted of surface energy only. In ductile materials, such as metals, plastic deformation occurs at the tip of crack. Much work is required to produce a plastic zone at the tip of an advancing crack. Therefore, for metals, R is mainly plastic energy. The surface energy is so small in comparison to the energy required to form the plastic zone that it can be neglected. The energy criterion is a

necessary, but not a sufficient criterion, for crack extension.

Consider a cracked plate of thickness, B, under a load P. Under the action of the load, the load-application points undergo a relative displacement η (η is the crack opening displacement (COD)). When the crack increases in size by an amount, da, the displacement will increase by an amount $d\eta$. Hence, the work done by the external force is $Pd\eta$. The crack driving force is then [6]:

$$G = d(W-U_E)/da = 1/B(Pd\eta/da - dU_E/da) \tag{2.5}$$

where U_E is the total elastic energy in a plate of thickness B. The deformations are elastic, leading to:

$$G = K_I^2/E \qquad \text{(plane stress)} \tag{2.6}$$

$$G_I = (1-\nu^2)K_I^2/E \qquad \text{(plane strain)} \tag{2.7}$$

where K is a stress intensity factor which describes the stress distribution around the crack tip and ν is the Poisson ratio. The subscript I represents the opening mode of the crack. Similarly, it can be shown that for mode II and mode III we will have the same type of expressions. The release rate of total energy in a combined mode cracking can easily be obtained by adding the energies from the different modes [6]:

$$G = G_I + G_{II} + G_{III} = [(1-\nu^2)/E] \cdot [K_I^2 + K_{II}^2 + K_{III}^2/(1-\nu)] \tag{2.8}$$

The different loading modes are shown in Figure 2.1.

Orowan [12] noted that the energy required for a crack to grow in a metal is much larger than the surface energy to create the new free surfaces. In metals, plastic

deformation occurs in front of the crack, and during crack extension energy is expended by the formation of a plastic zone. If the plastic energy R is the same for every crack increment, $R = dU_s/da$ is still a constant. Experimentally, this is approximately the case for plane strain cracks in small scale yielding [6]. Specimens containing cracks of various sizes appear to fail at the same value of G. This critical G value is denoted as G_{Ic} and it follows by analogy to the brittle criteria:

$$\sigma_c = (EG_{Ic}/\pi a)^{1/2} \tag{2.9}$$

For a particular stress, σ_1, the energy release rate, G_{Ic}, is proportional to the crack size, a. Here, the subscript I represents the mode I loading of cracks. Equation (2.9) could be rewritten as:

$$G = \pi\sigma^2 a/E \tag{2.10}$$

This equation represents the so-called "elastic energy release rate". The energy consumed in crack propagation is denoted by $R = dW/da$, which is called the crack resistance.

A modified form of the Griffith equation which accounts for finite sample-size effects in a plate of width W, containing a central crack of length $2a$ oriented perpendicular to the tensile axis (Figure 2.2) is given by [6]:

$$\sigma = [(2E\gamma/\pi a)\cot(\pi a/W)]^{1/2} \tag{2.11}$$

where 2γ is the work per unit area associated with forming the new crack surface. This approximation is based on the assumption that the crack length is small compared to the sample width W.

Where there is a problem of many cracks, the stress concentration around the tip of the cracks should be considered in interactions among cracks. The stress concentration is a function of the shape, orientation, and distribution of the cracks.

The fracture strength of a material is lower when cracks are present. The fracture strength decreases as the size of the cracks increases. The stress, σ_{ij}, at a point located a distance, r, from the crack tip and at an angle ϕ as measured counter-clockwise from the crack plane is given by [1-8] :

$$\sigma_{ij}=K_I * f_{ij}(\phi)/(2\pi r)^{1/2} \qquad (2.12)$$

where K_I is the stress intensity factor which describes the stresses at the crack tips, and $f_{ij}(\phi)$ is a function of geometry. This equation is an elastic solution, which will lead to an infinite stress at the crack tip when r equals zero. Practically, this cannot occur: plastic deformation or blunting taking place at the crack tip keeps the stresses finite [8].

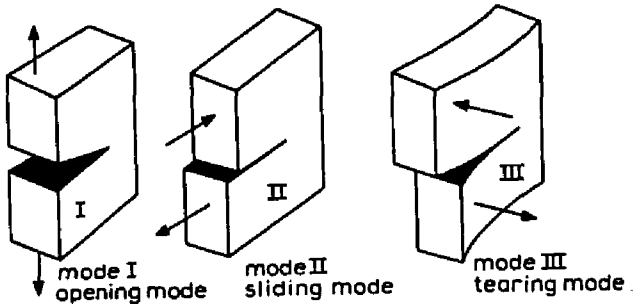

Figure 2.1 Modes of crack opening [6].

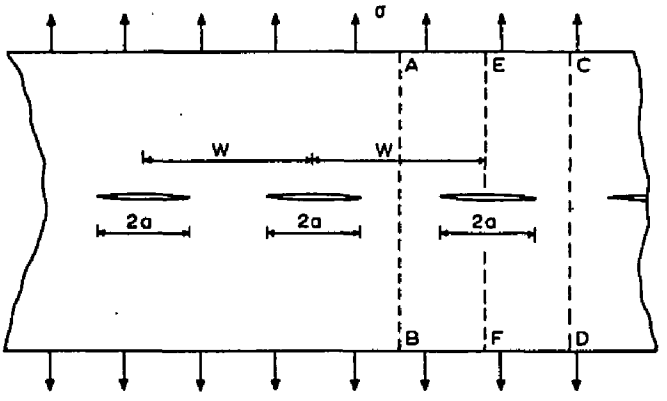

Figure 2.2 Crack array scheme [6].

2.2 Continuum Approaches

Budiansky and O'Connell [9, 13, 14] used a self-consistent approximation to calculate the elastic modulus of a solid with an isotropic distribution of cracks. The self-consistent energy approach assumed that:

$$\Phi = \Phi_0 + \Delta\Phi \tag{2.13}$$

where Φ_0 is the isothermal potential energy (strain energy plus load potential) of the uncracked body under prescribed loading, Φ is the corresponding quantity for the cracked body, and $\Delta\Phi$ is the potential energy change due to insertion of cracks. The effective elastic constant was then calculated by estimating $\Delta\Phi$ for various loading systems [see section 4.2].

Kachanov [15, 16] used a superposition technique and the ideas of self-consistency [17] to solve the stress intensity factors for both the 2-D and the 3-D problems with arrays of small cracks of arbitrary geometry. The superposition method assumed that the elastic solid with N cracks is subjected to remote loading and is equivalent to the one with traction applied to the crack faces where the stresses vanish at infinity. Therefore, the problem can be represented as a superposition of N problems, each involving only one crack but loaded by an unknown traction. By introducing a transmission coefficient Λ, the traction on a crack, **P**, could then be expressed as a function of the remote load and the transmission coefficient:

$$\langle \mathbf{P} \rangle = \mathbf{P}^{\infty} + \Sigma\, \Lambda^{(k)} \bullet \langle \mathbf{P} \rangle \tag{2.14}$$

where the summation is made over all the k cracks. The stress intensity factors were calculated and they are in good agreement with the exact solution for the periodic array of the cracks in the plate.

2.3 Statistics of Brittle Fracture Process

It is of considerable practical interest to understand the mechanical behavior in the dilute and intermediate regions of randomly disordered systems . In all real materials there is a finite number of disorders or defects, and when exposed to stress fields, the growth of cracks in materials occur from these "seeds". Such "seeds" are believed to be important in the mechanical behavior of real materials, and could be point defects, line defects, surface defects, and volume defects. Sizes, shapes, population, and the distribution of the defects will have a great influence on the mechanical properties of the materials.

The brittle fracture strength of a material under a homogeneous state of stress is related to the structure of its defects, that is, to the concentration and severity of defects and to the distribution of the defects in the specimen. Therefore, a statistical approach will lead to an effect of size on fracture strength: *i.e.*, if either a certain number or a certain severity of cracks is required to cause fracture, the occurrence of fracture depends on the statistical expectation of encountering the critical conditions in the specimen. This expectation is directly related to size of the specimen; the smaller the specimen, the less likely the critical condition is achieved.

Following Freudenthal [8], the probability of finding a severe crack in a certain area of the sample, denoted by A, is obtained as follows: Let $P^*(A)$ be the probability of non-occurrence of the critical crack in area A and $P^*(A_1)$, the probability of non-occurrence of the critical crack in area A_1 (which does not include A), then the probability of non-occurrence in the area $(A+A_1)$ is:

$$P^*(A+A_1)=P^*(A)\cdot P^*(A_1) \tag{2.15}$$

for the probabilities are statistically independent. Differentiation with respect to A leads to:

$$dP^*(A+A_1)/dA = P^*(A_1) \cdot dP^*(A)/dA \qquad (2.16)$$

and dividing equation (2.16) by equation (2.15) yields:

$$d[\ln P^*(A+A_1)]/dA = d[\ln P^*(A)]/dA = \text{constant} \qquad (2.17)$$

Equation (2.17) is valid for any arbitrary value of A_1. Then, $P^*(0)=1$, since the occurrence of a crack requires a finite area [if the area = 0, it is impossible to have a crack, so that the corresponding probability of finding a crack is then zero. In other words, the probability of non-occurrence is $P^*(0)=1$] and $P^*(\infty)=0$. In an infinite area there is at least one severe crack, so the probability of non-occurrence is zero. Integration of equation (2.17) produces the general relation:

$$P^*(A) = e^{-cA} \qquad (2.18)$$

where c has dimensions of $[\bar{A}^{-1}]$, and $c=\bar{A}$ represents the mean concentration of cracks. The smaller the value of $\bar{A}$, the average area per crack, and the larger their concentration, the more rapid is the decrease of $P^*(A)$ with A.

If the occurrence in the area A of a single crack of critical severity is assumed to produce a fracture of this area, then the probability of fracture can be expressed as an exponential function of the area:

$$P_F(A) = 1-P^*(A) = 1-e^{-cA} \qquad (2.19)$$

Equation (2.19) is independent of any assumption concerning the physical nature of cracks such as a shape, or orientation. To derive this equation we assume that the

occurrence of a single critical crack in the area A produces fracture. This assumption can be generalized by introducing a critical (minimum) number ($n>1$) of cracks that is required to produce fracture [8].

To apply this statistic theory to the distribution os dilute crack in the sample, we assume that:

1. There is no interaction or only a weak interaction between cracks, so that the individual effect of a crack in each area element can be analyzed, independently of those in any other area element, as if it were the only crack existing in the medium.
2. The strength of an area element is related to the severity of the crack it contains by Griffith's theory.
3. The strength of any specimen is uniquely defined by the strength of that area that contains the most severe crack.

From original Griffith relation $\sigma x^{1/2}=\text{constant}=k$, if the half-crack length, x, and the local tensile strength, σ, are considered as random, the relation between the probability distributions $F(\sigma)$ and F(x) can be determined as follows:

Let Σ and l be one of the local tensile strength and the half crack length. The probability of $\Sigma\le\sigma$, $Pr(\Sigma\le\sigma)$ is equal to the probability of $l\ge x$, $Pr(l\ge x)$, and the probability of $l\ge x$ is equal to the probability of $l\ge k^2/\sigma^2$, $Pr(l\ge k^2/\sigma^2)$. So, $Pr(\Sigma\le\sigma)=Pr(l\ge x)=Pr(l\ge k^2/\sigma^2)=1-Pr(l\le k^2/\sigma^2)$. These probability will lead to:

$$F(\sigma)=1-F(k^2/\sigma^2) \tag{2.20}$$

or

$$F(\sigma)=1-F(x) \tag{2.21}$$

Since F(x) is the probability Pr($l \le x$), we can define $\Phi_n(x)$ as the probability that all of the cracks (total n) with the half crack length l_i in a sample are less than x in half-crack length, then:

$$\Phi_n(x) = [F(x)]^n \tag{2.22}$$

which implies the probability that a specified value $l_i = x$ is the largest value in the sample.

To determine the distribution form of F(x), we construct m samples, each containing n cracks. The distribution of the largest value in the mn observations will approach the same asymptotic expression as the distribution of the largest value in samples with n cracks.

The two distributions are of the same form if they are related by a linear transformation. Thus, the probability that the largest value is below x can be set equal to a linear function of x of the form:

$$[F(x)]^n = F(a_n x + b_n) \tag{2.23}$$

Now we have to figure out the form of a_n, b_n and F(x). There are two typical solutions for this equation with respect to A: $a_n \neq 1$, $b_n = 0$; and B: $a_n = 1$, $b_n \neq 0$, respectively, which lead to different types of distribution function of F(x). We will discuss both cases.

A. The Case of $b_n=0$ and $a_n\neq1$

In the case of $b_n=0$ and $a_n\neq1$, from equation (2.23) we obtain:

$$\{[F(x)]^n\}^m=[F(a_nx)]^m=F(a_na_mx) \tag{2.24}$$

and,

$$\{[F(x)]^n\}^m=[F(x)]^{nm}=F(a_{nm}x) \tag{2.25}$$

therefore,

$$a_{nm}=a_na_m \tag{2.26}$$

which might be satisfied by the equation:

$$a_n=n^k \qquad k=\text{constant} \tag{2.27}$$

Thus,

$$\ln(n)+\ln[-\ln F(x)]=\ln[-\ln F(n^kx)] \tag{2.28}$$

We can interpret equation (2.28) as if x is increased by factor n^k (the right-hand side of the equation) or if ln(x) is increased by kln(n), ln[-lnF(x)] is increased by ln(n) (the left-hand side of the equation), so:

$$\frac{d\ \ln[-\ln F(x)]}{d\ \ln(x)} = \frac{\ln(n)}{k\ln(n)} \qquad (2.29)$$

by integrating once we obtain:

$$\ln[\ln F(x)] + \ln(x)/k = \text{constant} \qquad (2.30)$$

or,

$$\ln[\ln F(x)] = [-\ln(x) + \ln(u')]/k \qquad (2.31)$$

where u' is a constant. Therefore:

$$F(x) = \exp[-(x/u')^{1/k}] \qquad (2.32)$$

F(x) is the probability of the crack length less than x in the area A_0. $\Phi_n(x)$ is defined as the probability that x is the largest crack length in a sample with n cracks. Letting $\alpha = -1/k$, we obtain:

$$\Phi_n(x) = [F(x)]^n = \exp[-n(x/u')^{-\alpha}] = \exp[-(x/u'n^{1/\alpha})^{-\alpha}] \qquad (2.33)$$

This equation implies that if u' denotes the modal (typical) value of the largest crack length in the area elements A_0 [the corresponding distribution function is F(u') and the area element is A_0], the modal value of the crack length in the area $A = nA_0$ is equal to $u'(A/A_0)^{1/\alpha}$ [If we let $F^n(x) = F(n^k x) = F(\Omega)$, $u'(A/A_0)^{1/\alpha}$ can be considered as an effective crack length in the area A ; the factor $(A/A_0 = n)$ represents the magnifying effect of the area on the modal crack length].

The area-dependent distribution of strength is directly obtained from equation (2.33) and equation (2.20):

$$[F(\sigma)]^n = 1-[F(x)]^n$$

$$= 1-\exp[-(k^2/(\sigma^2 u' n^{1/\alpha}))^{-\alpha}]$$

$$= 1-\exp[-A/A_0(\sigma/v)^{2\alpha}]$$

$$= 1-\exp[-A/A_0(\sigma/v)^{2\alpha}]$$

$$= 1-\exp[-n(\sigma/\sigma_u)^{2\alpha}] \tag{2.34}$$

$$v = k/u'^{1/2} = \sigma_u \tag{2.35}$$

where σ_u is modal strength value, α is a constant, $A/A_0 = n$ is the number of cracks per unit area, and α is a measure of the dispersion of their distribution.

It is interesting that the distribution of local strength, which is proportional to $1/2\alpha$, is narrower than that of crack size, which is proportional to $1/\alpha$.

Assume that u' is the modal flaw size for some initial distribution of flaw size in a sample of area A. If this distribution is altered by external loading or any other means, the new modal value of the flaw size, u, is related to the old value u' by the relation implied by equation (2.33) and equation (2.34):

$$u = u' \cdot n^{1/\alpha} \tag{2.36}$$

Then, if u' is kept constant and n, the initial crack density, increases, the modal value of u, which determines the modal value of the local strength, will also increase; this increase will be the faster, the larger the dispersion of initial crack sizes, and the smaller the value of α. At constant crack density, n, the modal value, u, will increase with

increasing u', which implies an overall increase of initial crack length, as well as with decreasing α. We can interpret equation (2.36) as accounting for finite sample sizes by transforming this size effect into a scheme based upon differences in the distribution of flaw size. Thus, the modal local strength:

$$\sigma_u = k/u^{1/2} = (k/u'^{1/2})n^{-1/2\alpha} \tag{2.37}$$

will decrease with increasing initial crack density, and the smaller the value of 2α, the greater the rate of this decrease. Therefore, the parameter 2α is not a measure of crack density, but only of crack dispersion: the larger α, the more uniform the crack size, and the smaller, therefore, the effect of the crack density, which disappears completely for uniform crack size, and this is the result of the weakest-link concept.

B. The Case of $a_n = 1$ and $b_n \neq 0$

First, we determine b_n in a manner similar to that for case A. For $a_n = 1$ and $b_n \neq 0$, equation (2.23) becomes:

$$[F(x)]^n = F(x + b_n) \tag{2.38}$$

$$\{[F(x)]^n\}^m = \{F(x + b_n)\}^m = F(x + b_n + b_m) \tag{2.39}$$

$$\{[F(x)]^n\}^m = [F(x)]^{nm} = F(x + b_{nm}) \tag{2.40}$$

and comparing equation (2.39) with equation (2.40), we obtains

$$b_{nm} = b_n + b_m \tag{2.41}$$

The solution to this equation is:

$$b_n = k \cdot \ln(n) \qquad k = \text{constant} \tag{2.42}$$

Now we can determine the function type of F(x). Taking a double logarithm on both sides of equation (2.38), we have:

$$\ln(n) + \ln[-\ln F(x)] = \ln[-\ln F(x+b_n)] \tag{2.43}$$

This equation shows that if x increased by the amount of b_n, then ln[-lnF(x)] increases by the amount of ln(n), which leads to:

$$\frac{d\{\ln[-\ln F(x)]\}}{dx} = \frac{\ln(n)}{b_n} \tag{2.44}$$

then substituting $b_n = k \cdot \ln(n)$ into equation (2.44) and integrating, we obtain:

$$F(x) = \exp[-\exp(-x/u)] \tag{2.45}$$

where u is also a constant. This is the Duxbury [36] form of the strength distribution. Now, defining $\Phi_n(x)$ as the probability that x is the largest crack length in a sample with a total n cracks:

$$\Phi_n(x) = [F(x)]^n = \exp[-n \cdot \exp(-x/u)]$$

$$= \exp\{-\exp[-x/u - \ln(n)]\} \tag{2.46}$$

$$= \exp\{-\exp\,[-(x+u\cdot\ln(n))/u]\}$$

Comparing this equation with the equation (2.45), we conclude that if u is the modal value of the largest crack length in the area A_0 and x is the physical largest crack length in the sample with area $A=nA_0$, then effective largest crack length is extended by the amount of $u\cdot\ln(n)$.

The area dependent distribution of the strength is directly obtained from equation (2.46), and if we apply the Griffith relation ($\sigma x^{1/2}=k=$constant), then

$$\begin{aligned}[F(\sigma)]^n &= 1-[F(x)]^n \\ &= 1-\exp\{-n\cdot\exp[-(\sigma/\sigma_u)^2]\} \\ &= 1-\exp\{-\exp[-((\sigma/\sigma_u)^2 + \ln(n))]\}\end{aligned} \qquad (2.47)$$

where σ_u is modal strength value which is equal to $k/u^{1/2}$, and σ is random variable stress (σ is the local strength corresponding to the random crack length x). $A/A_0=n$ is the number of cracks per unit area. There is an equivalent decrease in σ_u with increasing crack densities.

C. Comparison of Case A and Case B

From the arguments made in Case A and Case B, we see that the enhancement of crack size results from the existence of other cracks. If we consider the effect of the crack densities only, both distribution forms are affected by the exponential term which is exp(-n). In case A, the result is to magnify the effect of the local modal crack length and to decrease the modal value of local fracture strength. In case B, the result is that increasing of the largest crack (in the sample, not local) length and increasing of the remote stress applied to the sample which certainly will increase the probability of the fracture of the material. In both cases, increasing the crack density will weaken the strength of material. For fracture behavior in case A, the more important factor is not crack density but is the dispersion of crack size which is reflected by α value (discussion in detail in the next chapter), and the larger the value of α, the more uniform distribution of the crack size; in case B, crack density plays a important role in the behavior of fracture strength. In our analysis of experimental data, we will use the solution for case A only.

2.4 Percolation Concepts

Percolation concepts [11, 18, 19] have been developed and improved in recent years, and the application of percolation theories to study the behavior of the elastic modulus and fracture stress of a random porous solid has been the focus of several theoretical investigations.

The simple picture of the percolation process is that of a fluid flowing through a porous medium such as a filter; if the fluid can find any channel allowing it to move from one side of the filter to the other, we say this porous medium is percolated.

Percolation theory, which describes the properties of classical particles interacting with an infinite random medium near its percolation threshold, provides a simple picture of critical behavior and is widely used to examine the critical behavior of classical particle systems.

There are two different types of percolation problems, the bond percolation problem and the site percolation problem. In the former, the random porosity of the medium is introduced by blocking or damming some of its bonds randomly. In the site or atom percolation problem, all the bonds are unblocked and the stochastic mechanism consists in blocking sites chosen at random, any site having a fixed probability $q=1-p$ of being blocked, where p is the fraction of unblocked sites. The fluid cannot flow through a blocked atom or site.

The bond percolation problem is similar to a simple model of the flow of a fluid through a porous material or a current flowing through an electrical network, while the site problem arises in simplified models of random binary alloys or in dilute ferromagnetic crystals.

The percolation probability, P, is defined as the probability that fluid from a single source atom or site, chosen at random, will wet infinitely many other atoms.

The critical probability, p_c is defined as the threshold of the percolation probability, that is, for $p<p_c$ the fluid spreads only locally. For $p>p_c$, the cluster is of infinite size, or the percolation channel spreads through the medium. This phenomenon has significant physical implications. For example [19], in a dilute ferromagnet, p_c is the lower bound to the concentrations of spins required for the ferromagnetic phase transition to occur. When $p=p_c$ the Curie point may occur at zero temperature while for $p<p_c$, there is no ferromagnetism. In another example, a dilute electrical network, the system will have an electrical breakdown under a certain value of applied voltage for $p>p_c$, but when p approaching to p_c, this value approaches zero.

The behavior of the elastic modulus of such porous solids was the focus of recent theoretical investigations and several experimental studies. A principal result of the theoretical studies is that the elasticity exponent, f, which governs behavior near the percolation threshold, p_c as $E\sim(p-p_c)^f$, in 2-D is approximately 3.5 for the discrete lattice model and $f+3/2$ for the " Swiss Cheese " continuum model. The conventional area of interest in fracture has been the regime where the density of cracks is such that they are considered not to interact. Weibull statistics [8] has been used to treat the brittle fracture problem in this regime.

In 1984, Kantor [20] studied the geometrical properties of singly connected bonds (SCB) in a LxL square lattice ($2\le L\le 140$) by Monte Carlo numerical simulation using the 'nodes and links' model [21]. The SCB character is applicable when the correlation length ξ is much larger than the sample's linear dimension L. This model has the character of a percolation system, eg., for p approaches to p_c, $\xi\sim(p-p_c)^{-\nu}$, where ν is 4/3 in two dimensions according to the percolation theory. If a single connected bond is cut, the cluster breaks into two parts. Kantor reported that the simulation showed that the lower boundary of the critical exponent of elasticity is around 3.6. Kantor and Webman [22] proposed a new model for elasticity of a percolating lattice network in which the elastic energy is given by:

$$H=(G/4)\Sigma_{ijk}K_{ij}K_{ik}\delta\phi_{ijk}^{2}+Q/(4a^{2})\Sigma_{ij}K_{ij}(U_i-U_j)\|^{2} \qquad (2.48)$$

The first term is associated with the bending forces, $\delta\phi_{ijk}$ is the change in the angle between the bonds (i,j) and (j,k) connected to the site i,k is equal to 1 if the bond exists and equal to 0 if the bond is missing. The second term is associated with central forces, which function like a spring. G and Q are local elastic constants. When forces are applied to the system, the relative changes $\delta\phi_i$ in the orientations of the bonds could be found by minimization of $W=H-F\cdot(R_n'-R_n)$. Kantor and Webman predict that there is a lower bound on the elastic exponent $t>(d-2)\nu+2$.

Halperin, Feng and Sen [23] discussed two different types of the percolation problems showing different transport exponents. The continuum percolation model, which is usually described as the "Swiss-cheese" model, has significantly larger exponents than that of the conventional discrete-lattice percolation model in both the 2-D and 3-D problems. For the shear modulus, $\mu\sim(p-p_c)^F$, they found $F=d\cdot\nu+5/2=f+3/2$ for $d=2$, and $F\approx d\cdot\nu+7/2=f+5/2$ for $d=3$. Here, f represents the exponent for discrete-lattice model and F, for continuum model, and ν is the critical exponential of the correlation length, defined as $\xi\sim(p-p_c)^{-\nu}$.

Sornette [24] also used a bent beam model [23] to study the mechanical failure of the two different types of percolation problems. When a stress, σ, is applied at the boundary of the specimen, the force F supported by a micro-link is:

$$F\approx\sigma\xi^{(d-1)} \qquad (2.49)$$

and the torque M is:

$$M\approx F\cdot\xi\approx\sigma\xi^{d} \qquad (2.50)$$

where ξ is the percolation (correlation) length $\xi \approx (p-p_c)^{-\nu}$. Using the expression $E \approx (1/2)\gamma\theta^2$ for the bending energy of the bond, where γ is the bond-bending force constant, the relation $M \approx \partial E/\partial\theta$ yields a relation between the moment and the bend angle $\theta \approx \gamma^{-1}M$ with $\gamma \approx (\delta/a)^{d+1/2}$, and δ and a are related to the macroscopic configuration of the system. Sornette derived the exponent of fracture stresses of three rupture criteria. He found that the critical exponent on the fracture stress, $F=(d+1/2)\cdot\underline{d}/a+d\cdot\nu$, where $\underline{d}$ equals to 1 or 0 for continuum or discrete-lattice models, respectively; a equals 2 if the rupture criterion is set for the bending elastic energy and equals 1 if the criterion is set for the bending angle. If the criterion is set for torque, the lattice result $F=d\cdot\nu$ is recovered.

Berg,nan [25] and Kantor [26] used a 2-D Sierpinski gasket fractal model to investigate the critical behavior of a random isotropic elastic medium. Hooks law was applied to the system, and the exponent on the elastic modulus was determined. An independently distributed, random-bond honeycomb network, with both bond stretching and bond bending forces, was used in computer simulation to study the critical exponent of the elastic moduli near percolation.

Feng and Sen [27, 28] studied the bond percolation on elastic networks with pure central forces by numerical simulations. The Born model was used to describe the potential energy of the lattice, *i.e.*:

$$V=1/2(\alpha-\beta)\Sigma_{ij}[(U_i-U_j)\cdot r_{ij}]^2 g_{ij}+1/2\beta\Sigma_{ij}(U_i-U_j)^2 g_{ij} \qquad (2.51)$$

where U_i and U_j are the displacements of node i and j, $g_{ij}=1$ for bonds the that are occupied with a probability p and 0 for the bonds that are missing with the probability $1-p$, and r_{ij} is the unit vector from site i to site j. The pure isotropic Born model, which has $\beta=\alpha$, reduces a scaler problem as the first term in equation (2.51) vanishes. The x component of force on site i can be written as:

$$(F_i)_x=\beta\Sigma_j(U_i-U_j)_x g_{ij} \qquad (2.52)$$

this equation is identical to Kirchhoff's equation for an electrical network if U is voltage, β the conductance, and F is the current on a node. The pure central force model, which has $\beta=0$, means that forces are involved only when a bond stretches or contracts, exactly like a spring. The pure central force model is rotationally invariant. As Feng and Sen pointed out for this model (pure central force, basically a network of springs), employing simple cubic lattice or a square lattice yield an elastic threshold of $p_c=1$, so that meaningful studies with this model are limited to certain lattices such as triangular and fcc. Physically, for a system composed of springs with free hinges arranged in a square lattice or a sc lattice, the system can freely deform without consuming any energy if there are no bending forces, *i.e*, the system is unstable to shear.

Feng and Sen [29] later studied the 2-D elastic networks with rotationally invariant bond-bending forces, using a potential energy of the form:

$$V=\alpha/2\Sigma_{i,j}[(U_i-U_j)\cdot r_{ij}]^2{}_{ij}+\gamma/2\Sigma_{ijk}(\delta\Theta_{ijk})^2 g_{ij}g_{ik} \qquad (2.53)$$

The second term represents the bond-bending forces and the first term represents the contribution of Hooks law . The bond-bending forces between two connected nearest-neighbor occupied bonds, *ij* and *ik*, are given in terms of the change in angle $\delta\Theta_{ijk}$ at site *i*. γ is a bond-bending force constant, and values of $\gamma=0.1\alpha$ and $\gamma=\alpha$ were employed in the simulations of a square lattice with sizes $3<L<50$, where L is the linear dimension of the sample. Feng and Sahimi [30] also examined the same model using a position-space renormalization method and obtained the same results as Feng and Sen [*29*] obtained in their computer simulations.

Feng, Thorpe and Garboczi [31] used an effective-medium theory to study the central-force elastic networks. A constraints method, a static method, and a coherent-potential approximation were used in conjunction with effective medium theory. First, applying a constraints argument, for small p, the system consists of disconnected pieces and has many so-called "zero-frequency" modes whose number is given by the number of degrees of freedom minus the number of constraints, then fraction of zero-frequency mode is given by:

$$f=(Nd-1/2\cdot zNp)/Nd=1-zp/(2d) \tag{2.54}$$

where d is the dimensionality of the system, N is total number of bonds, and z is the number of nearest neighbors. For the triangular system, z=6. When f goes to zero, equation (2.54) leads to the threshold $p_{cen}=2d/z$. The static method was used to develop a mean-field theory for the elastic constants for $p>p_{cen}$. The authors introduced a "wrong bond" with a modified force constant to the missing bond and assumed that this missing bond "sees" the effective medium. They then calculated the effective force constant. In the coherent potential approximation, the Hamiltonian of the system is:

$$H=H_0+V \tag{2.55}$$

where,

$$H_0=\Sigma_i(P_i)^2/(2M)+\alpha_m/2\Sigma_{ij}[(\mathbf{u}_i-\mathbf{u}_j)\cdot\mathbf{r}_{ij}]^2 \tag{2.56}$$

and,

$$V=(\alpha-\alpha_m)/2[(\mathbf{u}_1-\mathbf{u}_2)\cdot\mathbf{r}_{12}]^2 \tag{2.57}$$

represents a single defect bond in an effective medium; here, α_m and α represent the force and modified force constant, respectively. This method produces the same result as the result they obtained in the static method.

Ray and Chakrabarti [32] used a molecular dynamic simulation to study the critical behavior of the fracture properties of dilute brittle solids near the percolation threshold of a 20x20 Lennard-Jones system. The Lennard-Jones potential is represented as:

$$V(r) = \epsilon[(a/r)^{12}-2(a/r)^{6})] \qquad (2.58)$$

The variation of average fracture stress with bond dilution concentration, p, is then calculated, for the square lattice, applied $p_c=0.5$ for bond percolation, $\epsilon = a = 1$, $\tau \approx 1$, a much lower exponent value of the fracture stress was obtained. They also [33] simulated a 400-atoms square Lennard-Jones system, and then compared the results with the results from the Weibull formula for the average fracture strength. In the dilute region, ($p<.1$), their results agree with the prediction of the Weibull analysis [see section 2.3]. In the percolation region, their results are far from the theoretical prediction.

2.5 The Fuse Network Analog of Brittle Fracture

There is an extensive literature on the topic of the percolating network. The model which has been employed by most people to study the failure in disordered media is a random resisters network [34,35]. First, consider a fuse network, where each fuse has the same resistance (for example, 1Ω, which has been used mostly for convenience); if the voltage on any one of the fuses is great than 1V, the fuse burns out and becomes an insulator. To make a random fuse system, one can place electrically identical fuses on the bonds of a regular lattice until a prescribed fraction of the bonds, p, is occupied. In other words, each bond has a probability, p, to be occupied by a fuse, and a probability $(1-p)$ to be replaced by an insulator. If p_c represents the threshold of bond percolation, below p_c the network functions like an insulator, while above p_c, if a sufficiently large voltage is applied to the network, some of the fuses will burn out or become insulators, and the network may break down. The resistivity of the system becomes infinite if enough fuses burn out.

"Fracture" is defined when the conductivity of the network becomes zero. The distribution of the voltages at the nodes is typically found by applying Kirchhoff's law. The fuse with a voltage over its burn-out limit is usually called a red bond or a hot fuse; it can burn out and become an insulator. If the applied voltage is large enough this process will continue until the "fracture" occurs. The distribution of breakdown strength or the "fracture" strength is then described by several forms as follows.

The Weibull distribution [8,36], which is used in mechanical engineering to study the fracture strength of brittle materials, is of the following form:

$$F = 1-\exp[-c_1 L^d (V/L)]^m \qquad (2.59)$$

where L is the linear dimension of the network, V is the applied voltage, c_1 and m are constants, and d is the dimensionality of the network. F is the probability of "fracture", which also is the probability of breaking of the first fuse or bond under the external voltage V in the system of length L. For the brittle fracture, there is no "plastic deformation" in the system, and once a fuse or bond breaks, the system will collapse if all the fuses have identical values. The distribution of the cracks or the dispersion of the crack distribution described by the Weibull distribution is a power law.

Duxbury, Beale and Leath [36] used the random fuse network as a percolation model to break down a quenched random system to study its fracture properties. Numerical and analytical studies based on the "most critical" defect in the network, combined with percolation theory led to a new distribution of the breakdown strength. They suggested that when p is above p_c in the percolation network, the probability of fracture has the form :

$$F = 1-\exp[-c_2 L^d \cdot \exp(-nL/V)] \tag{2.60}$$

where L, V, and d have same meaning as in the Weibull distribution, and c_2 and n are constants. This distribution implies that the dispersion of cracks or the distribution is exponential instead of governed by the power law assumed in the Weibull distribution. Duxbury and his coworkers claimed that this distribution fitted the computer simulation data better than did the Weibull distribution. They showed that this distribution is correct when the distribution form from which the extreme values are drawn is exponential, as is the case in the percolation problem away from p_c. If this model is mapped to brittle fracture, the fracture probability will be:

$$F(\sigma_b) \sim 1-\exp\{-cL^d \cdot \exp[-k(1-/\sigma_b)^{1/\alpha}]\} \tag{2.61}$$

in the large L (sample linear dimension) limit, where σ_b is the average failure stress of the network, *i.e.*:

$$\sigma_b \sim 1/[a+b(\ln L)^{\alpha}] \tag{2.62}$$

with $1/[2(d-1)] \le \alpha_b \le \alpha_1 \le 1$ as it was for the fuse network, and $n_b = N_b/L^{d-1} = O(1)$ for p away from percolation threshold p_c. n_b represents the number of the bonds broken in the breakdown process and N_b is the total number of the bonds in the system.

In 1988, Beale and Srolovitz [37] studied the 2-D triangular lattice with nearest-neighbor harmonic springs system. A statistic approach and a local fracture criterion is used to model crack growth. Both the Weibull and the Duxbury distribution forms were checked against the results of computer simulations. Beale and Srolovitz reported that the Duxbury form fitted the data better than did the Weibull form, because the size distribution function for the cluster in their percolation model is an exponentially decreasing function of cluster size. They also found nonlinear elastic modulus behavior in their constant strain simulations. At a fixed p, the fracture stress, σ, is a slowly decreasing function of the sample size, L.

Beale and Duxbury [38] also studied the dielectric breakdown in metal-loaded dielectrics. A two-dimension square lattice system with sizes L=50, 70, and 100 was analyzed. The Laplace's equation for such a system is:

$$\Sigma_{ij} C_{ij}(V_i - V_j) = 0 \tag{2.63}$$

where the constant C_{ij} is equal to 1 if sites i and j are connected by a capacitor, and equal to 10^6 if they are connected by a conductor. The distribution function of the breakdown has the same form as equation (2.60) which dependents on the sample's size. They found that, in general, the complete breakdown field is the same as the initial

breakdown field, which means that the fracture is very brittle.

Recently, Stephens and Sahimi [39] investigated the fracture behavior for two different kinds of distribution functions. In their system, each fuse is assigned a conductance, g, which is selected at random from a probability density function f(g). For one case, the distribution was:

$$f(g)=(1-\alpha)g^{-\alpha}, \qquad 0<\alpha<1 \tag{2.64}$$

where α is a constant and g is the conductance. Also, Halperin, Feng and Sen [23] showed that this distribution describes the conductance of channels in the random void model of continuous media. This model is a nonlinear system, which means that the resistors in the system do not have equal resistivity. The other distribution function examined was:

$$f(g)=(2\lambda)^{-1} \tag{2.65}$$

where the conductance, g, is uniformly distributed in the interval $(1-\lambda, 1+\lambda)$. Stephens and Sahimi also examined the predictions of the Weibull distribution and that used by Duxbury. Based upon their results from computer simulation they claimed that neither of the distributions could fit the data satisfactorily for their nonlinear system, but the distribution of Duxbury *et al.* accurately predicted the fracture strengths for the linear system.

Kahng, Batrouni, Redner and coworkers [40] used a random fuse system with continuously distributed breaking strength to investigate breakdown properties. In their resistor-fuse network, each resistor is of the same resistance and the threshold voltage is uniformly distributed over the range $v_- = 1-w/2$ to $v_+ = 1+w/2$ for $0<w<2$. They found that the breakdown properties depend crucially on w and on the linear dimension of

sample size L. The fracture is brittle for sufficiently small w, and ductile for a large w which is close to 2. They studied the w dependence of the average number of bonds that have failed, $<N_b>$, when the breaking point of the network is reached; actually, they considered the scaled quantity $\chi = <N_b>/L$-1 for convenience. They found that for the larger value of w ($w > 1.5$), χ is an increasing function of L for all values of L attainable in their simulations, which they claimed is indicative of ductile behavior. For intermediate values of w and whit L sufficiently small, the network seems to be in the ductile regime of the phase diagram, and χ is an increasing function of L. However , for larger values of L, the network is predicted to cross over to brittle behavior, and χ will correspondingly vanish as L approaches to ∞.

2.6 Review of Previous Experiments

So far, there have been are only a few 2-D and only one 3-D experiments to measure the elasticity and fracture strength (fracture strength was not measured in three dimensions experiment) of the percolation system.

2.6.1 The 2-D Experiments

In 1984, Benguigui [41] performed a 2-D experiment to measure the critical exponential of elastic constants (and conductivity) of porous solids near the percolation threshold. Foils of copper and aluminum of 0.2 mm thickness and of 20 x 20 cm^2 were used, with random holes of 1 cm in diameter punched on sites corresponding to a square lattice. The measurement showed that near the percolation both elasticity and conductivity follow a power law behavior. The elasticity exponential is $T=3.7\pm0.2$ for Cu, and $T=3.3\pm0.2$ for Al, and the conductivity exponential is $t\approx1.1\sim1.2$. This was the first experimental work showing that the elasticity exponential is much larger than the conductivity exponent, and that they belong to different universality classes. As pointed out by Kantor [20], this experimental result fits the computer simulation which showed that $T\approx3.5$.

We emphasize that in Benguigui's experiment [41], their sample was constrained to stay in an x-y plane and was moving in a y direction only. since the sample was not allowed to rotate, an extremely large amount of torque might have to be applied to the sample to prevent its spinning, especially when the p value is near the percolation threshold. We already know that the electrical fuse network has the same pattern of breakdown as the mechanical network provided that the central force assumption is applied. In this case, Benguigui's experiment might alter the true mechanics of the

system to a certain degree.

In 1987, Benguigui, Ron, and Bergman [42] measured the strain and the stress of a perforated metal foil and of a dilute elastic network near the percolation threshold. First, they used sheets of 21 x 21 cm in which they randomly punched holes of 1.1 cm diameter on a square lattice of 1 cm unit cell. The sample was elongated at a speed of 0.05 mm/s, and the fracture stress and fracture strain as a function of $(p\text{-}p_c)$ were recorded. The authors claimed that they always found that the stress at the first break is also the largest stress. Thy reported the critical exponent of fracture stress, $T_f = 2.3 \pm 0.5$, and the critical exponent of fracture strain, $T_u = 1.5 \pm 0.5$. Second, they used a sample made of copper in which they made a uniform square lattice of 900 (30 x 30) holes. Inter-hole bonds then were cut at random. A known force was applied and the corresponding strain was measured. The force was then increased by small increments until the sample ruptured. They could not observe the fracture quantitatively in this experiment because the fracture of the rapidity with which it occurred. The critical indices of $T_f = 2.5 \pm 0.4$ and $T_u = 1.4 \pm 0.2$ were reported.

We notice that in Benguigui's experiments [42], the first type of sample is similar to the continuum percolation model. The unit cell of square lattice is 1 cm and the hole punched is in 1.1 cm diameter, therefore, overlap occurs. The second type of sample is a discrete lattice percolation model. According to Sornette [24], we expect to see different critical values of the fracture exponent for the two different types of percolation model, except where the rupture criterion is set for torque. This seems to be the case for $F = d\nu$, when $\nu = 4/3$, $F \approx 2.67$.

Allen, Golding, and Haemmerle [43] in 1987 made dynamic measurements of the shear modulus for a 2-D bond percolation system. The model was tested on cylindrical samples with a length/diameter ratio of 3.5 (the length was approximately 10 cm), patterned with holes of 0.17 cm in diameter arranged in a square lattice which had 3480 bonds, and in a hexagonal lattice which had 5200 bonds. The top of the

samples was fixed and the bottom was attached to a flywheel; the system was a torsional pendulum with the mass of the flywheel. The torsional oscillation was driven at frequency ω by electrodes mounted on opposite side of the flywheel. By measuring the resonant frequency of the sample which obeys the simple relationship $\omega \sim (\mu/I)^{1/2}$, where I is the moment of inertia of the wheel, the shear modulus, μ, as a function of ϵ, which is defined as $\epsilon \sim (p-p_c)/p_c$, were then obtained. The experiment was performed in the range of $0.2 < \epsilon < 0.6$ and the shear modulus exponential of $\tau \sim 3.6$ was obtained.

2.6.2 The 3-D Experiment

In 1985, Deptuck, Harrison, and Zawadzki [44] measured the electrical conductivity and Young's modulus of sintered, submicron silver powder beams. The volume fraction of the beams varied from 0.097 to 0.291. A three-point bending test was performed to measure the Young's modulus, and the experimental results showed that the modulus followed:

$$Y \sim (f-f_c)^{\tau} \tag{2.66}$$

where $\tau = 3.8 \pm 0.5$ and $f_c = 0.062$. Here, f represents the fraction (silver powder) of the volume.

3. 2-D EXPERIMENTS

3.1 Experimental Set Up

Two different configurations were used to examine the mechanical properties of random porous 2-D solids; the honeycomb and the square lattice systems. The honeycomb lattice results have already been reported [45], our idea was to take a perfect 2-D solid, to generate or randomly populate it with cracks, then to see how its mechanical properties (elastic modulus, or stiffness, and the fracture stress, or strength) vary with the distribution of crack sizes and densities.

The sample sizes we used were limited, and therefore, the size of cracks that could be created are limited. We chose to study the honeycomb lattice because that we were able to have more sites or bonds (closed packed structure in 2-D) in the sample, which provides for meaningful statistics. On the other hand, the square lattice provides a "sharp" cracked system which differs from the conventional lattice model or "nodes-links" model employed in computer simulations.

Fig. 3.1 shows the Young's modulus, E, and fracture stress, σ, for a system composed of a 2-mm-thick plate of aluminum with holes drilled at position corresponding to a honeycomb lattice of 21 rows and 20 columns. The samples contain 1230 ligaments (or bonds) which link the voids arranged in the triangular lattice. Each bond in the sample with a given address was assigned a random number, n, between 0 and 1. The bonds for which $n>p$ were cut, where p decreased successively from 1, and the elastic modulus and fracture stress were measured.

The tests were performed on a Instron model 4202 universal testing machine, which was interfaced with a Hewlett-Packard 86B desk-top computer. The lower boundary of the sample was fixed in the lower grip of the machine . The upper side of

the sample was connected to the loadcell in the upper part of machine by a universal joint which prevented lateral force or torque during testing. The elongation of the specimen was measured by attaching an extensometer to its lower and upper bounds. Tension was applied by fixing the lower grip and pulling the upper grip at a speed of 0.002 inch per minute. As the sample is pulled, the load and the extension of the sample were measured by the Hewlett-Packard computer, and the load-displacement curve was plotted.

Measurement of Young's modulus was made in the linear-elastic portion of the load-displacement curves; the elastic behavior was confirmed by unloading and checking for resultant plastic strains. Each datum point for the Young's modulus represents an average of at least three separate load-displacement curves. The fracture stress, σ, was determined by obtaining the full load-displacement curve for the sample to failure. The fracture stress is defined as the maximum in-load of the load-displacement curve. The behavior of Young's modulus was examined using two realizations. A single sample was used for the first realization and E was determined for successive descending values of p. In order to implement the second realization, eighteen identical samples ($p = 1$) were prepared from a template. Bonds were cut in each sample according to a prescribed value of p, and the Young's modulus determined for that sample. Following Young's modulus determination, we measured the load-displacement curve of the sample to failure.

The square lattice system was composed of a 2-mm-thick plate of aluminum with the cracks cut at positions corresponding to a 11 rows and 10 columns square lattices (Figure 3.2). The sample size was 11 x 9 cm. There were 200 "non-exist or possible cracks" which lay between the nearest "sites" in the square lattice. A random number, n, between 0 and 1, was assigned to each "invisible crack" and the "cracks" for which $n \geq p$ were cut to form the real cracks, each crack was about 1cm long and .01 cm in width, where p decreases successively from .975 down to 0.49 and the

measurement of the elastic modulus and fracture stress was made for each p value.

The experiment were carried out on a Instron stress testing machine using a 5,000 lbs loadcell. The upper grip was fixed and connected to the upper side of the samples; the samples were limited to the minimum rotation by not using the universal joint in the grip as we did in the 2-D honeycomb test. The lower boundary of samples were hooked to the lower grip. The tensions were applied by pulling down the lower grip of the system, pulling at a rate of 0.002 inches per minute. The elongation of the samples along tensile axis was recorded by attaching an extensometer to the central line of upper and lower parts of the specimen, which is parallel to the tensile axis. The reason we used the fixed upper grip instead of the universal joint is that this sample is tougher than that in the 2-D honeycomb test, and the sample's rotation (or open in one side and close in the other side) due to the uneven distribution of the cracks will cause the extra amount of the load to the load-displacement curve. In this experiment, all the initial cracks looked like very narrow slots, the small amount of negative displacement due to the spin of the sample would close the cracks and make contacts between the upper and the lower surface of such a line-shape crack, the extra amount of energy would be then stored in the sample, and this is the case we wished to avoid.

To ensure that the modulus would be obtained in the elastic region, we used 10 samples to perform a pretest, so that the situation of having fatigue crack growth would not happen in the formal modulus test.

We were not able to test the "perfect" sample in our experiment. Physically, the testing of a perfect sample requires something to fix or to hold the sample, and if this connection between the sample and machine is not careful prepared, the test will become a test of the strength of the connecting. There are some ways to do this like welding the connection or using a high vacuum-sucker connection, but such modifications make the simple test very complicated and difficult.

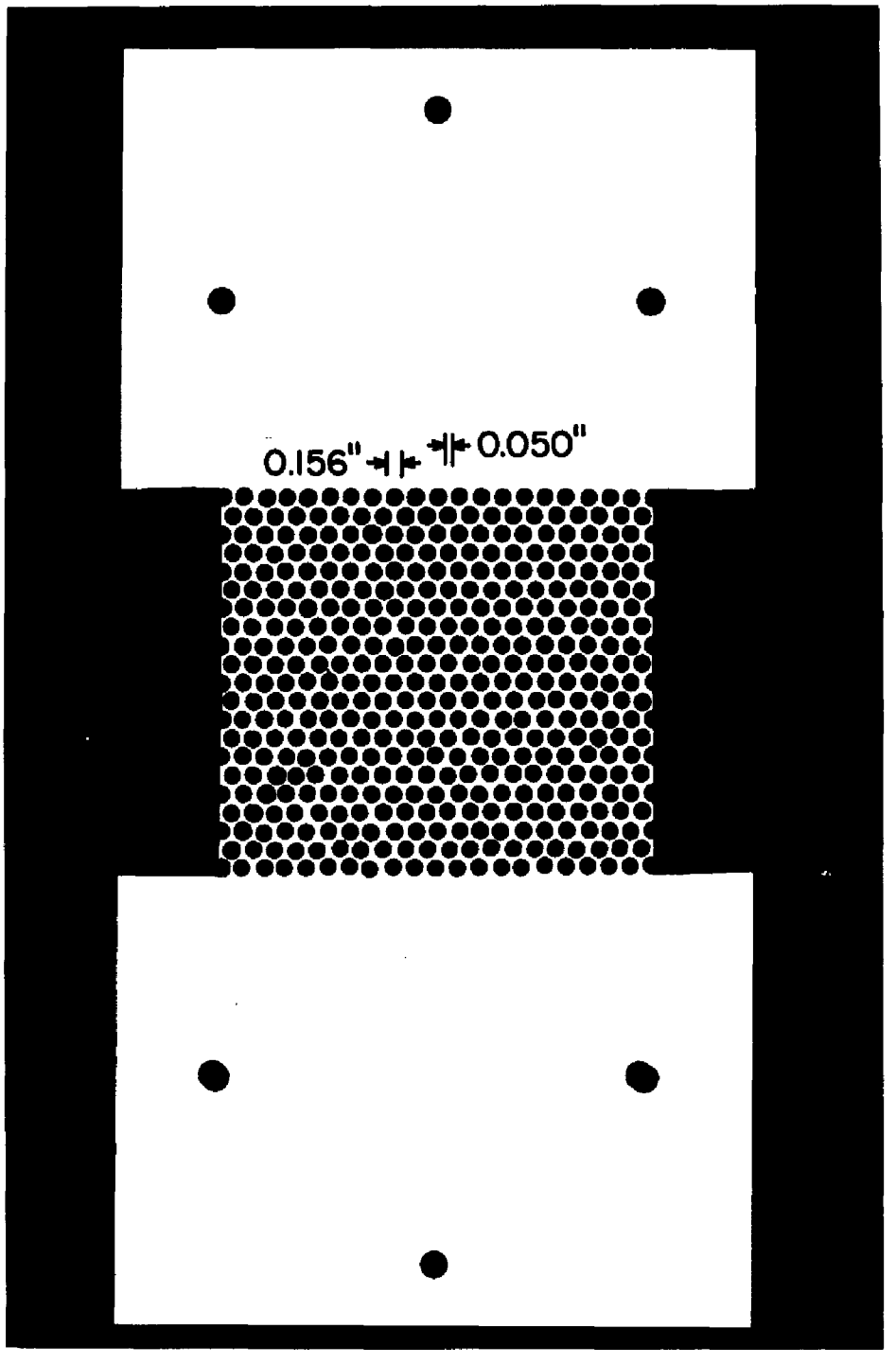

(a) $p = 1.00$

Figure 3.1 The configuration of the 2-D honeycomb network. The ligaments connecting the voids are randomly cut forming cracks, as described in the text. (a)$p = 1.0$, (b)$p = 0.74$, (c)$p = 0.64$.

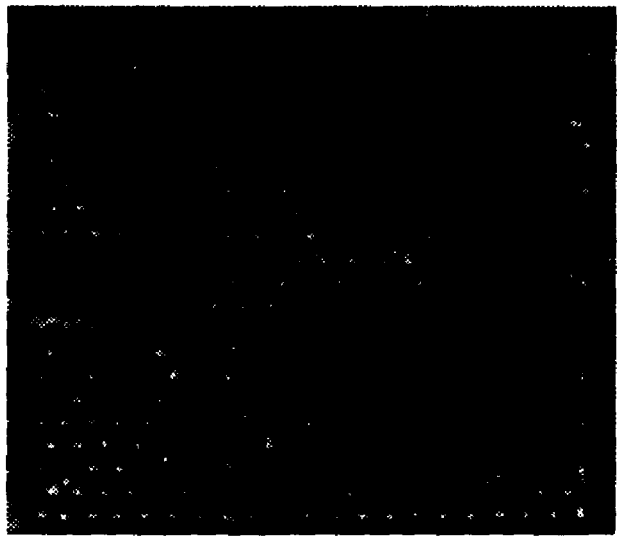

(b) p =0.74

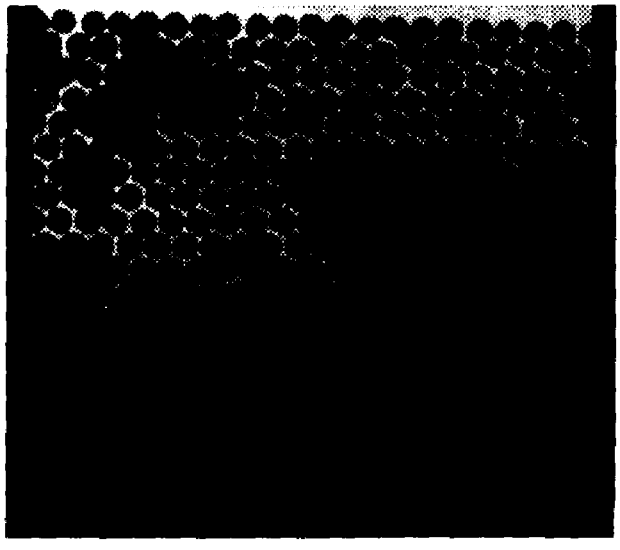

(c) p =0.64

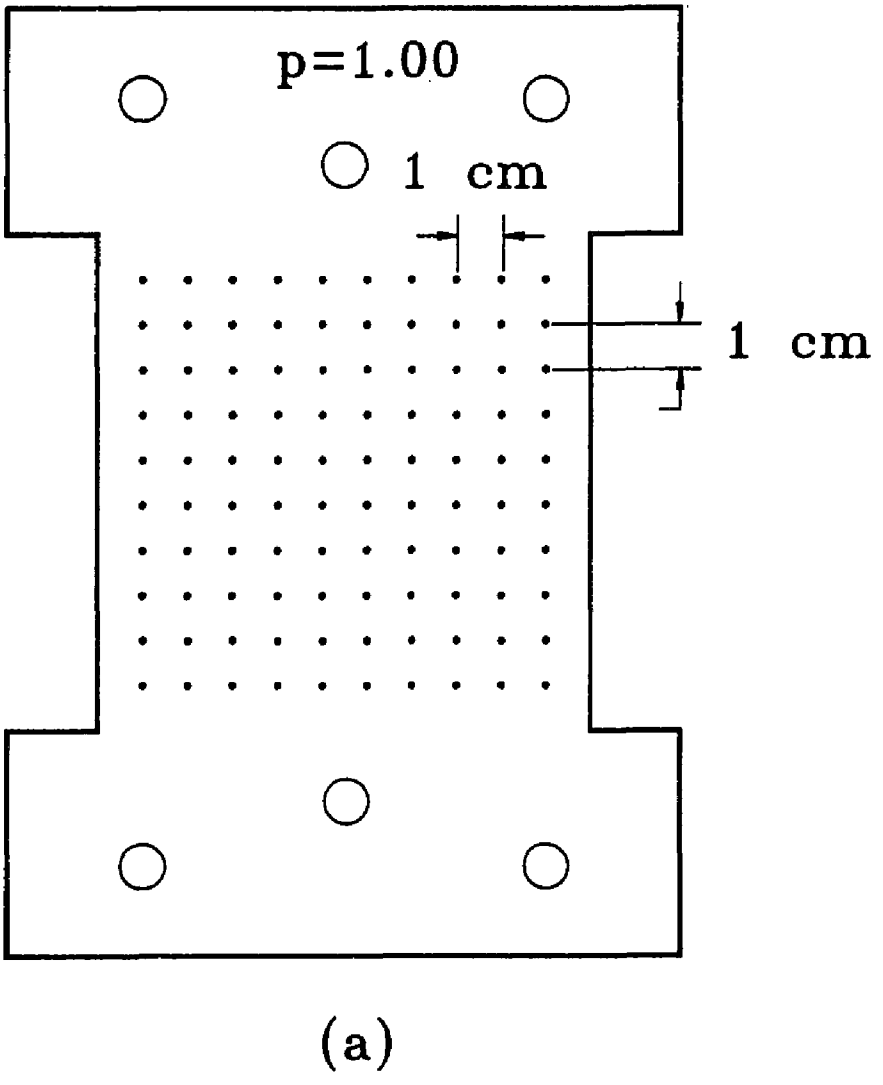

Figure 3.2 The configuration of the 2-D square lattice.

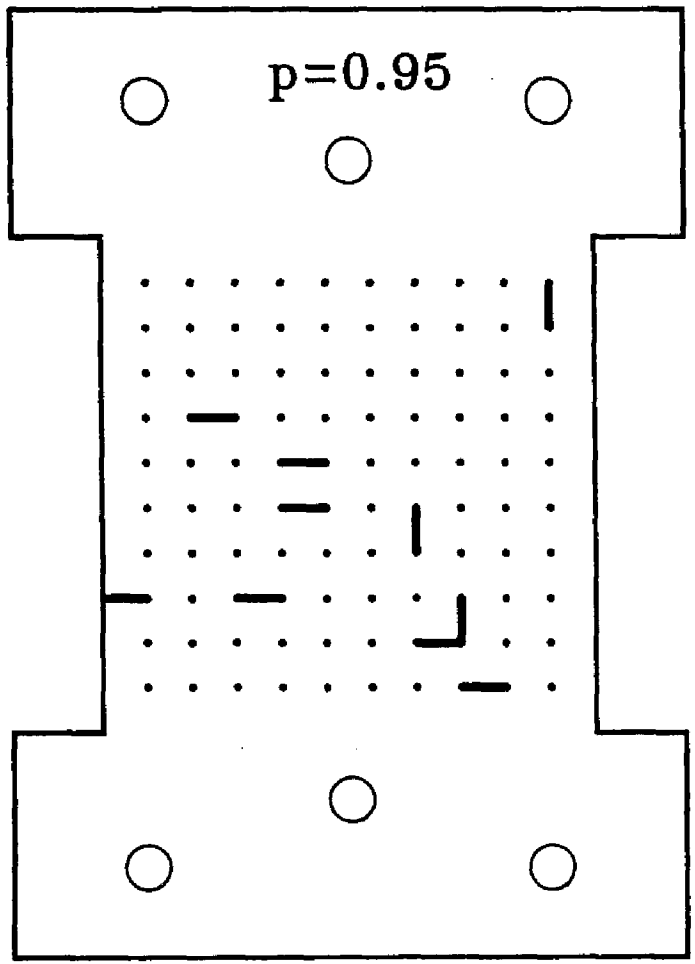

(b)

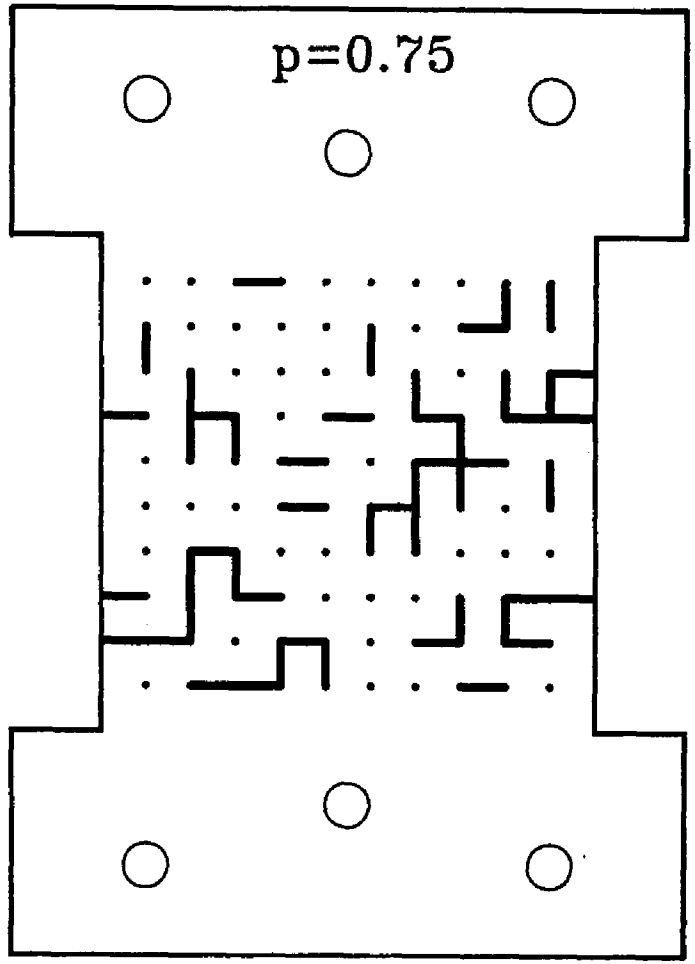

(c)

3.2 Results With The Honeycomb Lattice

Table 3.1 shows the results of the mechanical test of the honeycomb lattice, where E_0 and σ_0 represent the elastic modulus and fracture stress of a "perfect" sample with $p = 1$. E is the average value of the elastic modulus over three measurements, and ΔE is the deviation of the elastic modulus from the average value.

Table 3.1 Results of the mechanical test of the honeycomb lattice.

p	E	ΔE	E/E_0	$\Delta(E/E_0)$	σ	σ/σ_0
	$Dynes/cm^2$			%	$Dynes/cm^2$	
1.0000	2.76E+10	1.38E+09	1.00E+00	5.00	8.07E+08	1.00E+00
0.9996					7.33E+08	9.07E-01
0.9992					6.32E+08	7.83E-01
0.9927					5.89E+08	7.30E-01
0.9837	2.62E+10	3.45E+08	9.50E-01	6.32		
0.9756					5.17E+08	6.41E-01
0.9650	2.47E+10	6.89E+07	8.97E-01	5.28		
0.9463	2.32E+10	6.89E+07	8.41E-01	5.30	5.00E+08	6.19E-01
0.9260	2.23E+10	5.52E+08	8.07E-01	7.48		
0.9065	1.93E+10	6.89E+07	7.01E-01	5.36	3.28E+08	4.06E-01
0.8902	1.86E+10	6.89E+07	6.75E-01	5.37		
0.8805	1.79E+10	2.07E+08	6.50E-01	6.15	2.31E+08	2.86E-01
0.8764	1.68E+10	6.89E+07	6.08E-01	5.41		
0.8585	1.52E+10	2.07E+08	5.52E-01	6.36	1.81E+08	2.24E-01
0.8561	1.49E+10	2.07E+08	5.40E-01	6.39		
0.8366	1.35E+10	3.45E+07	4.91E-01	5.25		
0.8317	1.21E+10	3.45E+07	4.39E-01	5.28	1.51E+08	1.87E-01
0.8228	1.18E+10	1.38E+08	4.27E-01	6.17		
0.8203	1.14E+10	1.38E+08	4.12E-01	6.21	1.35E+08	1.67E-01
0.8024	1.02E+10	1.38E+08	3.69E-01	6.38		
0.8000	9.33E+09	1.38E+07	3.38E-01	5.15	1.22E+08	1.51E-01
0.7927	9.72E+09	2.07E+07	3.52E-01	5.21		
0.7829	7.14E+09	3.45E+08	2.59E-01	9.83	8.04E+07	9.96E-02
0.7642	4.48E+09	1.03E+08	1.63E-01	7.31		
0.7610	4.55E+09	6.89E+07	1.65E-01	6.52	7.04E+07	8.72E-02
0.7537	2.22E+09	5.52E+07	8.05E-02	7.48		
0.7447	2.21E+09	3.45E+07	8.00E-02	6.56		
0.7374	1.94E+09	3.45E+07	7.05E-02	6.77		
0.7260	1.72E+09	1.38E+07	6.25E-02	5.80	4.60E+07	5.69E-02
0.7175	1.25E+09	1.38E+07	4.52E-02	6.10		
0.7041	1.17E+09	1.38E+07	4.23E-02	6.18		
0.6902	8.62E+08	3.45E+07	3.12E-02	9.00	3.25E+07	4.02E-02
0.6813	4.41E+08	3.45E+07	1.60E-02	12.81		
0.6699	3.45E+08	3.45E+07	1.25E-02	15.00		
0.6512	1.99E+08	3.45E+07	7.21E-03	22.34		

The results for Young's modulus and the fracture stress are shown in Figure 3.3. E_0 and σ_0 are the measured values of these quantities when all the bonds are present ($p=1$). For the honeycomb lattice, the theoretical bond percolation threshold is $p_c=0.653$. In our experiments the measured value of p_c in the first realization was 0.625, and in the second realization was 0.630 which are in good agreement with the theoretical value. In the region far away from p_c the modulus behavior is well described by $E/E_0=1-3.3\phi$ (where $\phi=1-p$) which is in good agreement with effective-medium theories.

Figure 3.4 is a log-log plot of E and σ vs $p-p_c$ in the scaling region assuming $p_c=0.63$, the value of p at which the sample become geometrically disconnected. The slopes of log-log plot represent estimates of the exponents and were determined by using data points with values of $p-p_c$ such that the percolation correlation length was smaller than the macroscopic sample size, L. The elasticity exponent f is 3.1 ± 0.1. The fracture stress also displays power-law behavior in this regime and the fracture stress exponent, F, is 1.7 ± 0.1. The first three points on the fracture strength curve in Figure 3.3 are important. The first point is the fracture strength of a perfect sample with $p=1$, the second point is the fracture strength of a sample with a single diagonal cut, while the third point corresponds to the fracture strength of the sample with a single horizontal bond cut. Figure 3.3 shows that a cut horizontal bond in the very dilute region plays much more important role than that of diagonal bond in fracture behavior. This behavior is quite similar to that of an electrical resistor or fuse in a network. In a perfect electrical fuse network (for simplicity, a square lattice system), according to the Kirchhoff's equation, the voltage across each horizontal fuse is zero, so that a single cut in a horizontal fuse will not affect the current distribution of the system, but a single cut in a vertical fuse will dramatically change the current and voltage distribution of the network. In our analysis of experimental results we will discuss the reasons and the mechanisms.

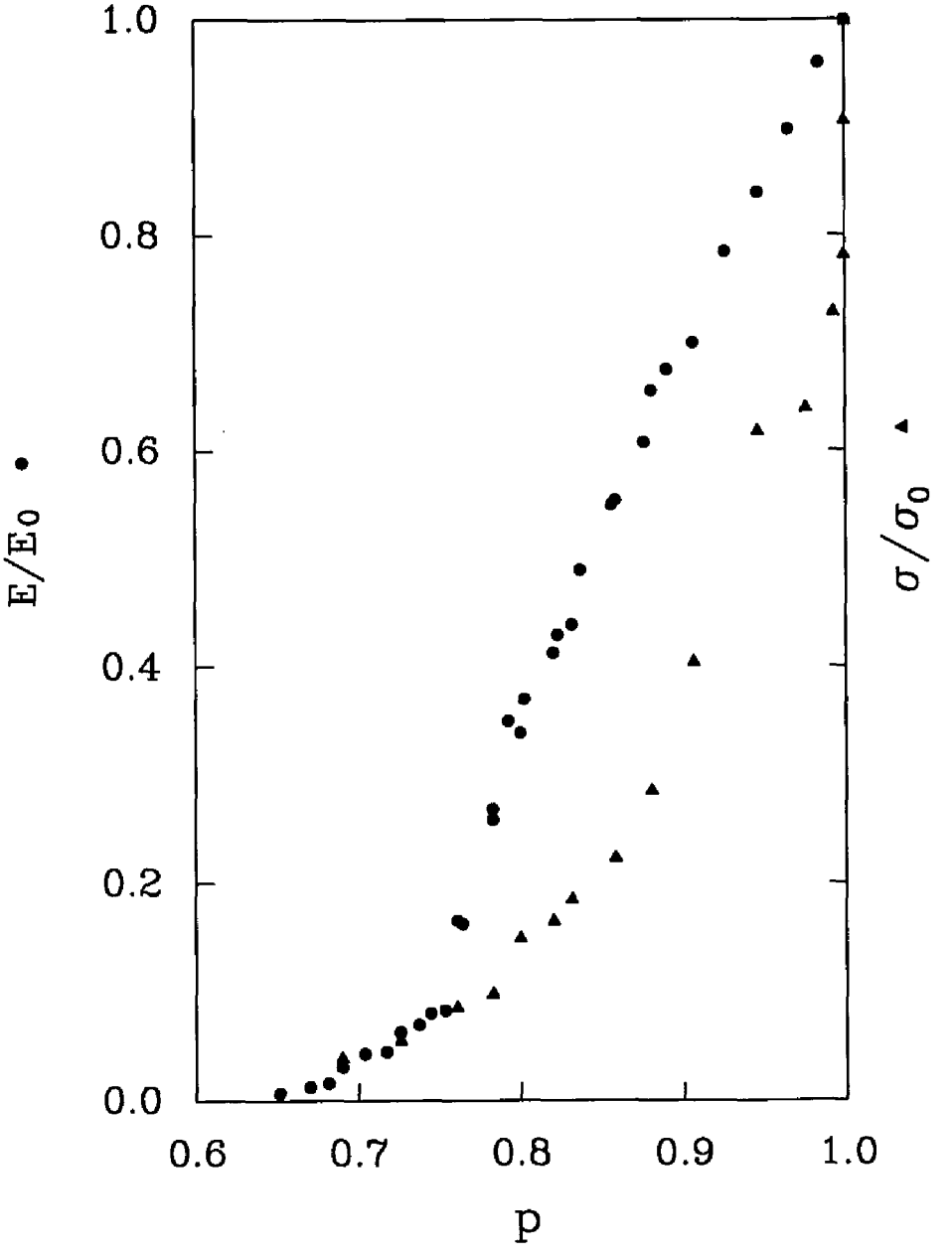

Figure 3.3 Normalized Young's modulus, E/E_0, and fracture stress, σ/σ_0, as functions of p for the honeycomb lattice.

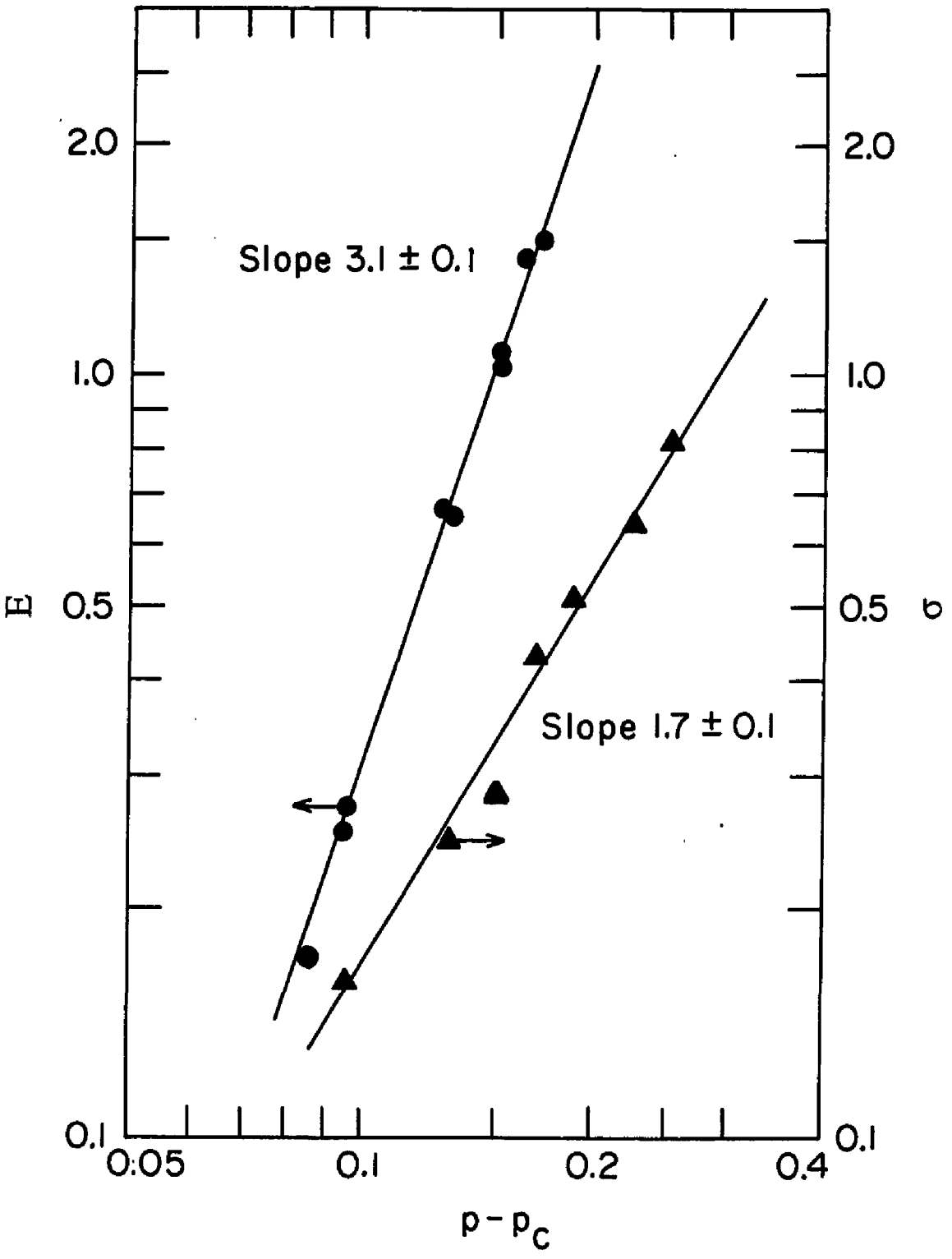

Figure 3.4 Double logarithmic plot of elastic modulus, E, and fracture stress, σ vs $(p\text{-}p_c)$ for the honeycomb lattice, $p_c = 0.63$.

3.3. Results With The Square Lattice

Table 3.2 shows the results of mechanical test with the square lattice, where E is the average elastic modulus over three measurements, and P_f represents the fracture load which is defined as the maximum load on the load displacement curve.

Table 3.2 Result of mechanical test of the square lattice

p	E	ΔE	P_f	σ
	Dynes/cm^2	%	Lbs	Dynes/cm^2
1.000	5.20E+11	3.23	12000	3.47E+09
0.975	4.11E+11	2.70	9500	2.74E+09
0.950	3.71E+11	2.33	8150	2.35E+09
0.925	4.22E+11	2.78	7850	2.27E+09
0.900	4.22E+11	2.78	7500	2.17E+09
0.875	3.90E+11	4.76	5600	1.62E+09
0.850	3.63E+11	2.38	5550	1.60E+09
0.825	3.63E+11	7.50	4300	1.24E+09
0.800	3.47E+11	4.65	4000	1.16E+09
0.775	2.94E+11	3.64	2750	7.94E+08
0.750	2.79E+11	1.82	2750	7.94E+08
0.725	2.36E+11	1.54	2040	5.89E+08
0.700	2.08E+11	6.25	1020	2.95E+08
0.675	1.88E+11	6.41	1060	3.06E+08
0.650	1.71E+11	9.64	1000	2.89E+08
0.625	1.59E+11	7.69	1000	2.89E+08
0.600	1.01E+11	3.13	740	2.14E+08
0.575	8.92E+10	7.89	780	2.25E+08
0.550	7.43E+10	8.70	750	2.17E+08
0.535	6.78E+10	20.69	700	2.02E+08
0.525	3.90E+10	29.82	450	1.30E+08
0.505	7.80E+09	13.04	230	6.64E+07
0.500	.57E+09	21.74	190	5.49E+07
0.490			100	2.89E+07

Figure 3.5 and Figure 3.6 show the experimental results. We see from the elastic modulus and fracture stress curve in Figure 3.5 that when $p>0.7$, both elastic modulus and fracture stress decrease linearly with decreasing p. When $p=0.7$, the elastic modulus keeps decreasing, while there is a plateau in fracture stress. In this region, the fracture stresses seems "saturated", which might indicate a finite sample-size effect (It might be due to deviation in σ. Experimentally, σ was a single measurement. The last four points show that σ decreases again). The sample size of the square lattice (total of 200 bonds) is much smaller compared with that of honeycomb lattice (1230 bonds).

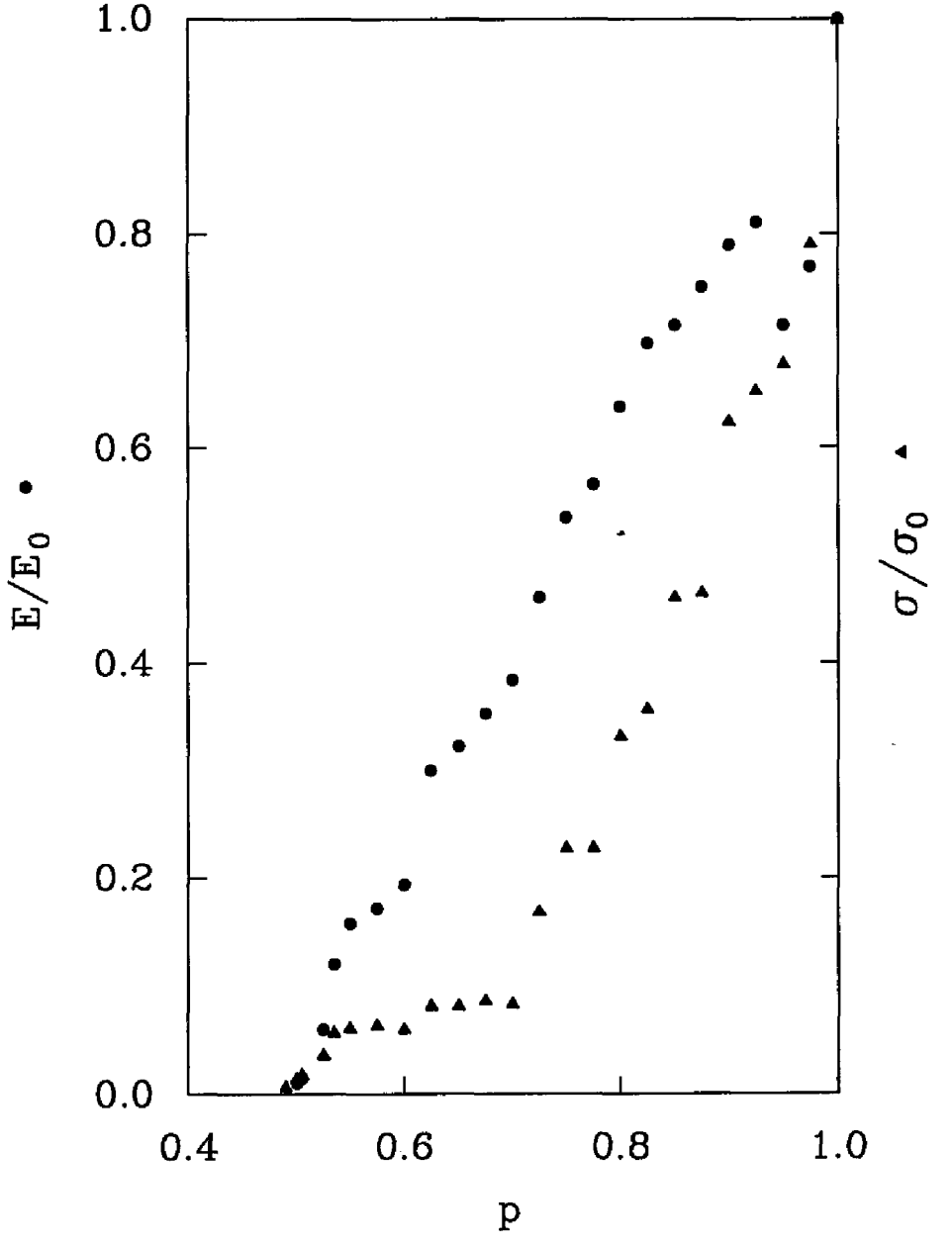

Figure 3.5 Normalized Young's modulus, E/E_0, and fracture stress, σ/σ_0, vs p for square lattice.

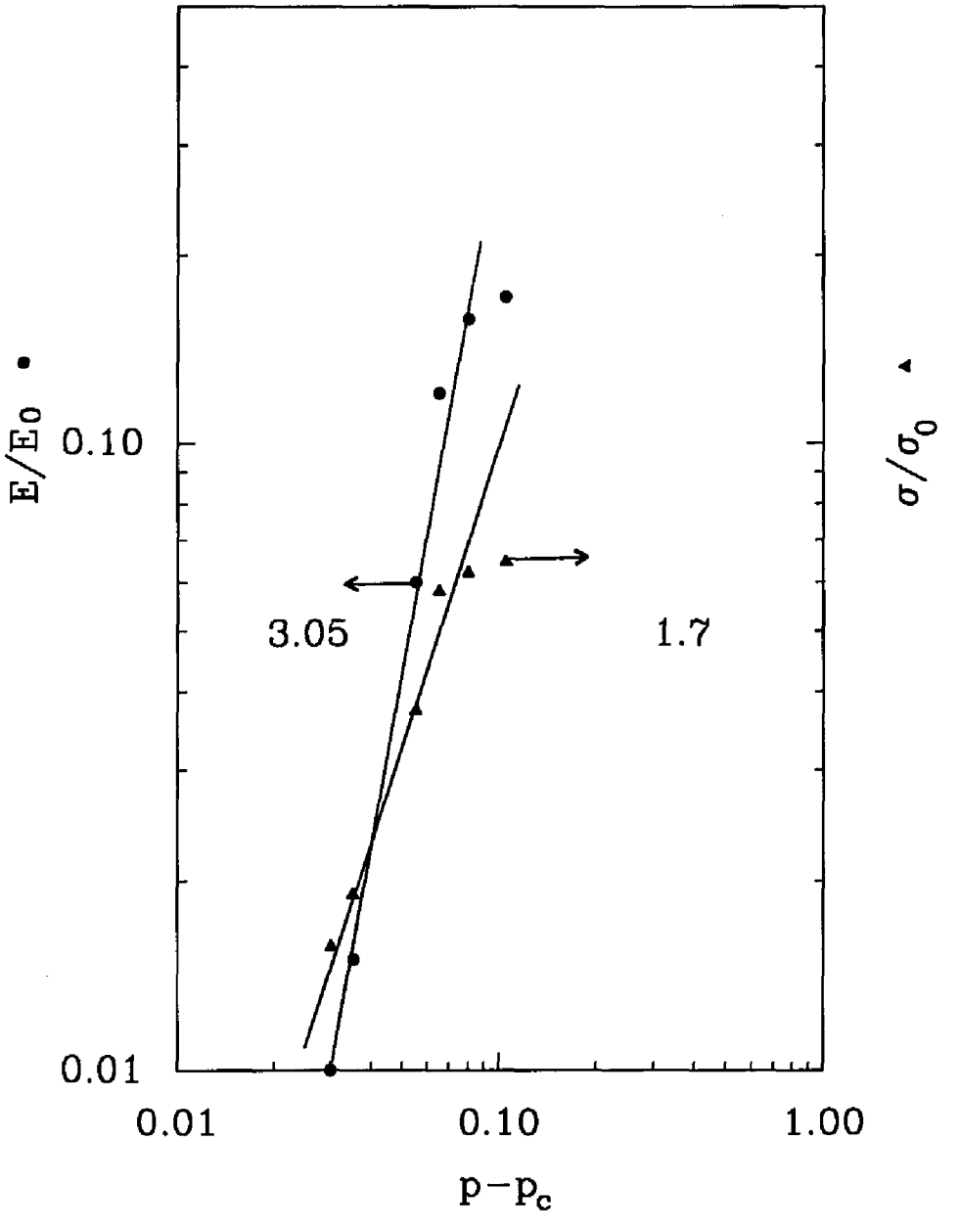

Figure 3.6 Double logarithmic plot of normalized elastic modulus, E/E_0 and fracture stress σ/σ_0 vs $(p\text{-}p_c)$ for the square lattice, $p_c=0.48$.

4. 2-D ANALYSIS

4.1 Introduction

We consider the fracture behavior of the system in three regions, *i.e.*, the very dilute region, where only few cracks exist and there are no crack interactions; the medium dilute region, where crack interactions became stronger; and the scaling region, where the sample is approaching geometrical breakdown and "crack" percolation.

In the very dilute region, an effective medium theory will be used to estimate the elastic modulus and fracture stress for the systems we examined. In the scaling region, we will employ the percolation theory in conjunction with the Griffith relation to study the behavior of the fracture stress. We will also examine the behavior of fracture stress in the dilute regions (very dilute and medium dilute) from the viewpoint of Weibull statistics.

The square lattice system we employed is quite different from the honeycomb lattice system. In the square lattice, there is a continuum sheet and therefore no real "bonds in the system. The stress-concentration plays a very important role in this system, as we observed during testing. Because there are no real bonds connecting lattice sites, the detailed mechanism of the cracking is different in this system compared to the honeycomb system.

In the honeycomb lattice, the cracks grow when the bonds are broken under a applied load and the diagonal bonds are less important than the horizontal bonds in causing the crack to expend. This is because the former "see" less load than the horizontal bonds. Physically speaking, the geometrical structure of the sample

(triangular voids array) reduces the interaction between the cracks in certain orientations and favors interaction along other directions. Only bonds transfer the forces in this system. For the square lattice at lower p, both vertical and horizontal cracks play important roles in determining crack interactions (this statement would not apply to the very dilute region, where horizontal cracks dominate the fracture and elastic behavior of the specimen). The cracks interacts with each other via the distribution of continuum stress fields instead of through bonds which link voids, as in the honeycomb lattice. The cracks grow through the path where the "bonds" do not exist and this could not happen in the honeycomb lattice system in which the voids can not transmit the forces or loads. Generally speaking, there is no favored orientation of the interaction between cracks in our square lattice system. This phenomena implies that the shape of the cracks only affects the "effective" crack size and not the physical breakdown properties around the percolation threshold, as we observed during our experiments.

4.2 Effective Medium Estimate of the Elastic Modulus Behavior in the Dilute Crack Region

Following the method of O'Connell and Budiansky [9] we estimate the elastic modulus of a 2-D solid with many cracks. The strain energy of a perfect specimen [4] is:

$$U = S^2A/(2E_0) \tag{4.1}$$

where S is the applied stress, A is sample area, and E_0 is the Young's modulus. The strain energy of a specimen with cracks is [46]:

$$U' = S^2A/(2E_0) + \pi S^2l^2/E_0 \tag{4.2}$$

where the second term of the right-hand side of equation (4.2) is the extra energy due to the presence of a central crack of length $2l$ in the solid. Treating the cracked sample as a "black box" we can write the strain energy of the sample as:

$$U' = S^2A/(2E) \tag{4.3}$$

where E is the effective modulus for the cracked plate. Equating equation (4.2) with equation (4.3) and solving for E/E_0 we get:

$$E/E_0 = 1-2\pi l^2/A \tag{4.4}$$

For a system containing N non-interacting cracks the strain energy is given by:

$$U' = S^2A/2E_0 + (\pi S^2/E_0)\cdot\Sigma l_i^2 \tag{4.5}$$

Here, summation is over all of the cracks in the cracked body, and l_i is the half crack length of crack i. Solving for the reduced modulus, E/E_0 yields:

$$E/E_0 = 1 - (2\pi/A)\cdot\Sigma l_i^2 \tag{4.6}$$

For the system with many non-interacting equivalent cracks of equal length, $2l$, Σl_i^2 may be represented by:

$$\Sigma l_i^2 = N^*\phi l^2 \tag{4.7}$$

where N^* is the total number of possible bonds, and ϕ is equal to the fraction of the missing bonds. The Griffith equation for two different configurations of the cracks in an infinite plate are as follows. For a crack of length $2l$ sitting in an infinite plate or a crack of length l sitting on the edge of a semi-infinite plate, the stress intensity factors have the same expression:

$$K=\sigma(\pi l)^{1/2} \tag{4.8}$$

A crack lying on the edge oriented perpendicular to the tensile axis acts as a crack with double the length of a crack in the center of a plate. In the very dilute region, each cut tends to create a new crack instead of connecting two smaller cracks and forming a larger crack, which implies that all of the cracks in the dilute region will have an equal

crack length $2l$. With $\phi = 1-p$, we obtain an effective medium estimate of the reduced Young's modulus:

$$E/E_0 = 1-(2\pi l^2/A)\cdot N^*\phi \qquad (4.9)$$

A. The Honeycomb Lattice

N^* is the total number of effective bonds and is equal to 820 in the honeycomb lattice system. As we mentioned before, the total number of bonds was 1230 of which 410 were horizontal bonds, and 820 were diagonal ones. At the low ϕ region where $\phi \leq .15$, experimental data show that the horizontal bonds play a much more important role in determining the mechanical properties of the material than the diagonal bonds. The diagonal bonds have only half the length of the horizontal bonds and, therefore, two diagonal bonds act as one horizontal bond. The effective number of the total bonds then becomes 820 in honeycomb sample.

With $\phi = 1-p$, from equation (4.9), using $N^*=820$, $A=4x3.6$ $(inch)^2$, and $l=0.1$ inch for our configuration, and taking the derivative of (E/E_0) with respect to ϕ, we obtain:

$$d[E/E_0]/d\phi = -3.58 \qquad (4.10)$$

This result compares favorably to the experimental data as shown in Figure 3.3 where the initial slope of the elastic modulus is about -3.3.

B. The Square Lattice

In square lattice system, N^* is equal to 130. The total number of the "imaginary" bonds was 200, of which 110 of were horizontal bonds and 90 were vertical ones. Among the 110 horizontal bonds, 20 of them were on the edges. A crack on the edge acts as a crack with double length in the body, and this is why we have $N^* = 130$. We simply use $l = 0.5$ cm because in the very dilute regime, each cut tends to create a new crack instead of connecting two smaller cracks and forming a larger crack.

With $\phi = 1-p$, using $N^* = 130$, $A = 11x9 = 99cm^2$ and $l = 0.5cm$, and taking the derivative of (E/E_0) with respect to ϕ, from equation(4.9):

$$d[E/E_0]/d\phi = -2.06 \tag{4.11}$$

This result yields an initial slope of approximately equal to -2 and is in good agreement with the experimental data as shown in Figure 3.5 .

To conclude, we believe that in this region, effective modulus behavior can be described by:

$$E = (1-\alpha\phi)\cdot E_0 \tag{4.12}$$

with α equal to approximately 2 in a square lattice, and 3.6 in a honeycomb lattice, where E_0 is the elastic modulus for the perfect sample, and $\phi = 1-p$ represents the fraction of missing bonds.

4.3. Effective Medium Theory Estimate of Fracture Stress

We will estimate the fracture stress by applying an effective medium theory in the dilute region as we did in estimating the elastic modulus.

If we consider a system with many cracks with each crack of length $2l$, the average size of area occupied by a crack is $A/(N^*\phi)$, *i.e.*, there are $N^*\phi$ miniature tensile samples, each with central crack of length $2l$. The width, W, of each block or tensile sample is then:

$$W=[A/(N^*\phi)]^{1/2} \tag{4.13}$$

A modified form of the Griffith equation which accounts for the finite sample size effects in a plate of width, W, containing a central crack of length $2l$ oriented perpendicular to the tensile axis is given by (see section 2.2):

$$\sigma=[2E\gamma/(\pi l)\cdot\cot(\pi l/W)]^{1/2} \tag{2.11}$$

where, σ is the stress, E is the elastic modulus, and 2γ is the work per unit area associated with forming the new crack surface.

The effective modulus of the system could be described by the modulus of the perfect sample, E_0, and the fraction of the missing bonds or cracks. Substituting equation (4.12) into equation (2.11), we obtain:

$$\sigma/\sigma_0=[(1-\alpha\phi)\cdot\cot(\pi l/W)]^{1/2} \tag{4.14}$$

where

$$\sigma_0=[2E\gamma/\pi l]^{1/2} \tag{4.15}$$

$$\pi l/W=\pi l\cdot(N^*\phi/A)^{1/2} \tag{4.16}$$

In the very dilute region of the square lattice, $2l$ is a constant and equal to a single crack length according to our equal length assumption, A is a sample area, and N^* is effective number of the cracks.

Consider a plate of width, W, containing a central crack of length $2l$, oriented perpendicular to the tensile axis, the stress intensity factor K is given by:

$$K=\sigma[\pi l\cdot\tan(\pi l/W)]^{1/2} \tag{4.17}$$

In terms of K, the Griffith equation is expressed as:

$$K^2=2E\gamma \tag{4.18}$$

where σ is the fracture stress, E is elastic module, and 2γ is the work per unit area associated with forming the new surface of the crack.

Substituting equation (4.18) into equation (4.8), the Griffith relation can then be expressed as:

$$\sigma=(2E\gamma)[1/W\cdot\cot(\pi l/W)]^{1/2} \tag{4.19}$$

In our case this equation is not strictly applicable since the cracks were not in line along the x axis, but were in different orientations and of various center-to-center spacing.

As we examine the sample's geometrical configuration, we see that most of the cracks will be formed in the direction which is not perpendicular to the tensile axis. Statistically speaking, the horizontal bonds and the diagonal bonds have the same probability of being cut. Will those cracks formed by cutting the diagonal bonds be as severe as the perpendicular ones, or should we assign them a smaller contribution to the elastic and fracture properties of the system? When a larger crack is formed by several unit-length cracks, it could cross over several rows. How shall we treat this crack with regard to the crack length and orientation, and what is the center-to-center spacing between two such cracks?

We wished to map this configuration to a reasonably equivalent and solvable system, *i.e.*, to a periodical array of cracks with effective crack length $2l$ and center spacing of W, so that we could apply the modified Griffith relation to our system.

Consider the sample with the total area A, and total number of bonds, N, for a perfect sample where none of the bonds has been cut. Let ϕ indicate the percentage of the bonds being cut.

We have determined the projected (on to the x-axis) crack length (perpendicular to the tensile axis) for the region $.02 \le \phi \le .14$ in our samples as shown in Figure 4.1. The relation between the average projected crack length and ϕ is reasonably represented by the straight line:

$$2l = (A^{1/2}/21) \cdot (4.69\phi + 0.80) \qquad (4.20)$$

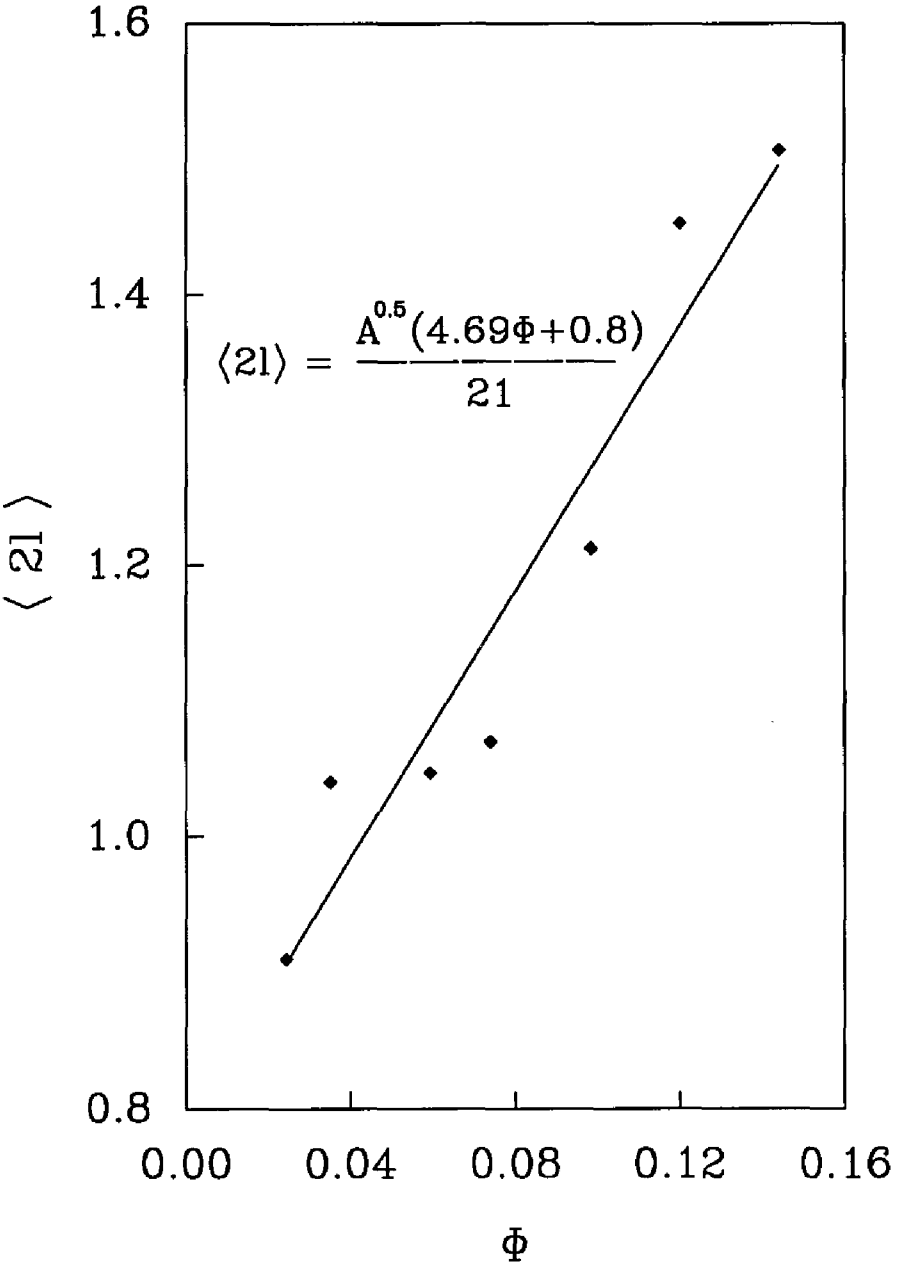

Figure 4.1 Average crack length, <2*l*> as a function of ϕ for the honeycomb lattice, where $\phi = 1\text{-}p$.

If the distribution of the blocks in the specimen is uniform, the average effective area occupied by each block is denoted by πr^2 and the linear dimension of such a block in any orientation is denoted by d (d=2r) so that:

$$\pi r^2 = (A/N_b) \tag{4.21}$$

where N_b represents the total number of the blocks, and r is a radius from the center of the block. Within this radial range, we will not hit the boundary of other blocks. Let W be the average d parallel to x axis given by:

$$W = d\langle\cos\theta\rangle = 2d/\pi = 4\cdot[A/(N_b\cdot\pi^3)]^{1/2} \tag{4.22}$$

where $\langle\cos\theta\rangle$ is the result of average projection. As shown in Figure 4.2, the total number of cracks or blocks, N_b, is reasonably proportional to the percentage of the bonds being cut, which is denoted by ϕ in this regime. The curve in Figure 4.2:

$$N_b = 495\phi + 15 \tag{4.23}$$

which leads to,

$$W \approx 0.718\cdot[A/(495\phi + 15)]^{1/2} \tag{4.24}$$

By substituting equation (4.24) and equation (4.20) into equation (4.19), we determine the fracture stress as function of ϕ. Figure 4.3 gives the results for the calculations and shows that this approximation is in reasonable agreement with our measurements. The deviations are within 10%. If we normalized the fracture stresses to that of the perfect sample, σ_0, then the initial slope of the fracture stress is:

$$d(\sigma/\sigma_0)/d\phi \approx -3.6 \tag{4.25}$$

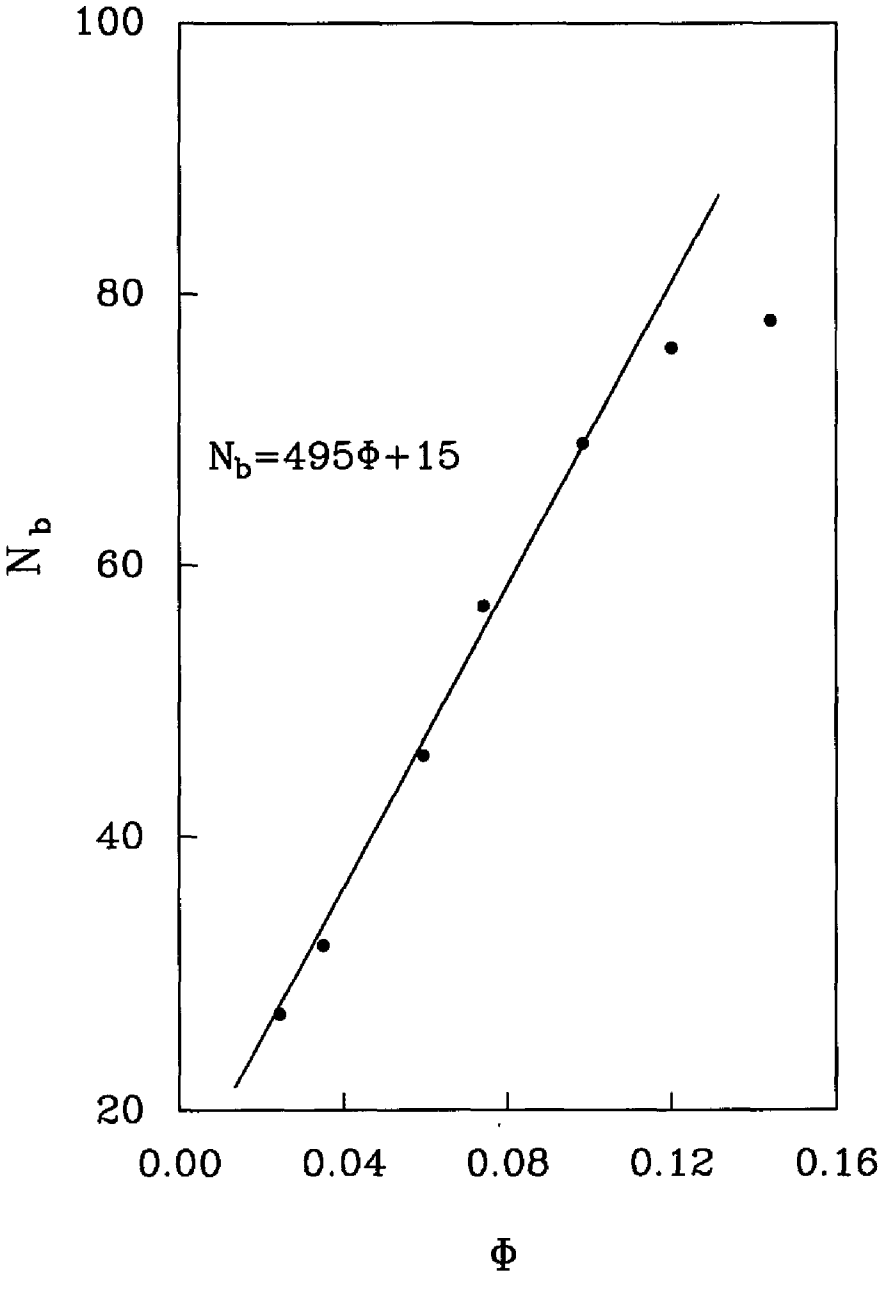

Figure 4.2 Number of the broken bonds, N_b, as a function of ϕ for the honeycomb lattice, where $\phi=(1-p)$.

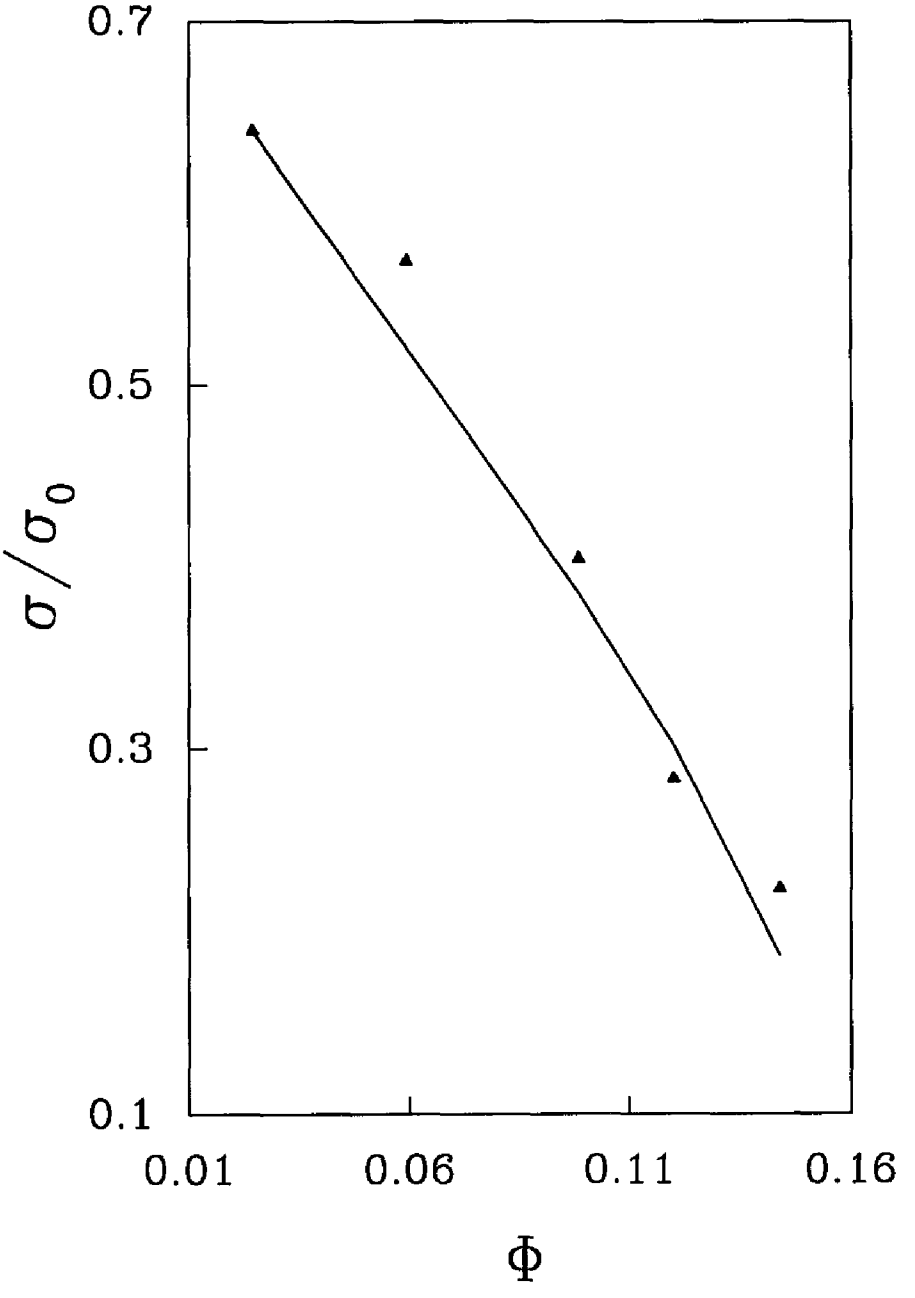

Figure 4.3 The fracture stress, σ, vs ϕ for the honeycomb lattice. The points represent the experimental data and the curve represents the data obtained from equation(4.19).

If we stay with the argument that all the cracks are equal in length, the following argument applies. The modified Griffith equation (2.11) can be written as:

$$\sigma = [2E\gamma/(\pi l)\cdot\cos(\pi l/W)]^{1/2} \tag{4.26}$$

For $E=E_0(1-\alpha\phi)$ with $\alpha=2$ for a square lattice, and $\alpha=3.6$ for a Honeycomb lattice, we obtain:

$$\sigma/\sigma_0 = [(1-\alpha\phi)\cdot\cos(\pi l/W)]^{1/2} \tag{4.27}$$

where,

$$\sigma_0 = [2E_0\gamma/(\pi l)]^{1/2} \tag{4.28}$$

Let A be a sample area, and N* the effective number of cracks. Each crack of length $2l$ is considered to occupy an average areal size $A/(N^*\phi)$. $N^*\phi$ is the miniature tensile samples, each with the central crack length $2l$. The width, W, of each block or tensile sample is $W=[A/(N^*\phi)]^{1/2}$. Then we obtain:

$$\begin{aligned} \pi l/W &\approx 2.37\cdot\phi^{1/2} \qquad \text{(Honeycomb)} \\ \pi l/W &\approx 1.80\cdot\phi^{1/2} \qquad \text{(Square)} \end{aligned} \tag{4.29}$$

Inserting equation (4.29) into the modified Griffith equation (4.27) and taking a derivative of σ/σ_0 with respect to ϕ, we obtain:

$$\begin{aligned} d(\sigma/\sigma_0)/d\phi &\approx -3.1 \qquad \text{(Honeycomb)} \\ d(\sigma/\sigma_0)/d\phi &\approx -1.8 \qquad \text{(Square)} \end{aligned} \tag{4.30}$$

Figure 3.3 and Figure 3.5 show that the linear plot of σ/σ_0 vs ϕ in the region of $.025 \le \phi \le .125$ is reasonably linear with a slope approximately -3 and -2, respectively.

In this dilute region, the spacing between two adjacent crack, W, is bounded by the finite sample size ($W \le L \approx A^{1/2}$) so that the expression developed for W is applicable in the range $0.04 \le \phi \le \phi_s$, where $\phi_s \approx 0.14$. In our block scheme, ϕ_s represents the crack density for which $W \le 2l$. For $W = 2l$, the adjacent cracks are connected forming larger cracks, and the assumption of equal crack size is no longer applicable. Near ϕ_s crack condensation and overlap is common.

4.4. Behavior of Fracture Stress in the Scaling Regime

We employed the percolation theory to analyze the fracture stress near the percolation threshold. The elastic modulus and the fracture stress near percolation follow power-law behavior. To estimate the exponential value of fracture stress, the Griffith equation is used:

$$\sigma = [2E\gamma/\pi l]^{1/2} \tag{2.4}$$

then replace l with average half crack length $<l>$, where:

$$<l> = \Sigma_i n(l_i) l_i^2 / \Sigma_i [n(l_i) \cdot l_i] \tag{4.31}$$

where, $n(l_i)$ is the number of the cracks with length $2l_i$ and the summation is over all of the cracks in the specimen.

We examined the experimental data for average half-crack length, $<l>$, and the elastic modulus E near percolation. The average crack size and elastic modulus obey the following relations in power law:

$$<l> \sim (p-p_c)^{-m} \tag{4.32}$$

$$E \sim (p-p_c)^{f} \tag{4.33}$$

Inserting equation (4.32) and equation (4.33) into the Griffith equation(2.4), yields:

$$\sigma \sim (p-p_c)^F \tag{4.34}$$

with

$$F=(f+m)/2 \tag{4.35}$$

A. The Honeycomb Lattice

We evaluated the behavior of the average crack spanning length perpendicular to the tensile axis by examining equation (4.31). Let l_i be the spanning length perpendicular to the loading axis of crack i, and $n(l_i)$ the number of cracks of length l_i. As shown in Figure 4.4, the double logarithmic plot of average crack length, $<l>$, vs $(p-p_c)$ shows that:

$$<l> \sim (p-p_c)^{-m}, \quad m=0.9\pm0.1 \tag{4.36}$$

Figure 4.4 shows that as the average crack length increase, the total number of cracks, n, decreases according to:

$$n \sim (p-p_c)^b, \quad b=0.5\pm0.05 \tag{4.37}$$

In the scaling region, new cuts will increase the size or length of cracks by disconnecting the linkage between the adjacent blocks. Unlike the behavior in the dilute region, most of the new cuts in the scaling region contribute to enlarging the existing cracks instead of forming new ones. Also, most of the clusters are so close (large crack size) that the probability of that any single cut might connect two smaller blocks to form a larger one is high.

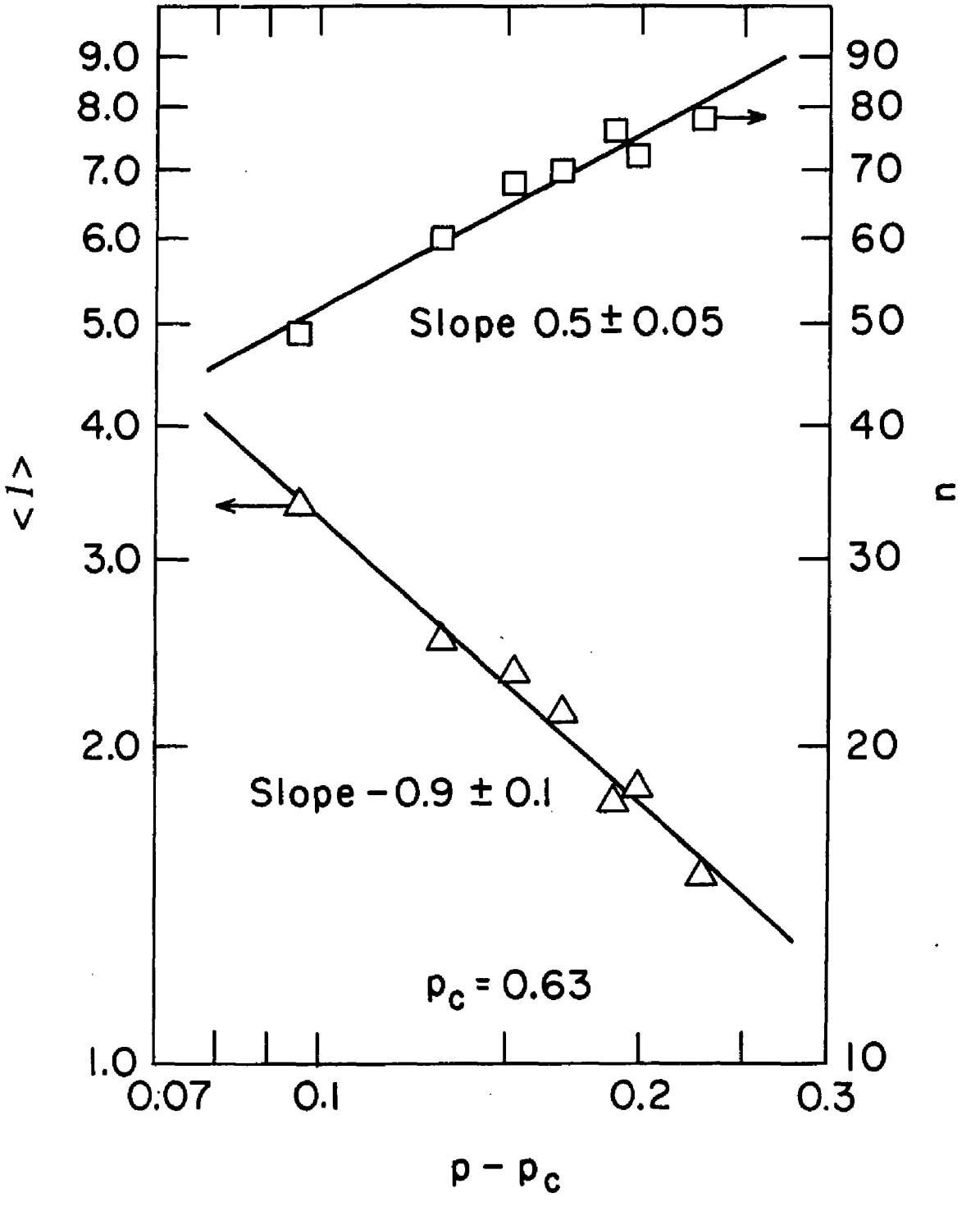

Figure 4.4 The average half-crack length (Δ), $<l>$, and number of the cracks (□), n, as a function of $(p\text{-}p_c)$ for the honeycomb lattice, where p_c=0.63.

In effect, as a result of the high linear density of cracks, we treat collinear cracks as connected to form a single crack of length $<l>$. In conjunction with the Griffith relation, these relations provide us with an understanding of the fracture stress in the scaling region. Substituting $E \sim (p-p_c)^{3.1}$ and, $<l> \sim (p-p_c)^{-0.9}$ for l into the Griffith relation yields:

$$\sigma \sim (p-p_c)^2 \tag{4.38}$$

The value of the fracture exponent from EMT is greater than that of the measurement which is $\sigma \sim (p-p_c)^F$, with $F = 1.7 \pm 0.1$.

B. The Square Lattice

For the square lattice, we examined the experimental data of average half-crack length, $<l>$, and the elastic modulus E near the percolation, Figure 4.5 and Figure 3.6 show that:

$$<l> \sim (p-p_c)^{-m}, \quad m \approx 0.47 \tag{4.39}$$

$$E \sim (p-p_c)^f, \qquad f \approx 3.05 \tag{4.40}$$

Applying the Griffith equation, we obtain:

$$\sigma \sim (p-p_c)^F$$

with,

$$F = (f+m)/2 = 1.76 \tag{4.41}$$

which is in good agreement with the experimental result of $F = 1.7$.

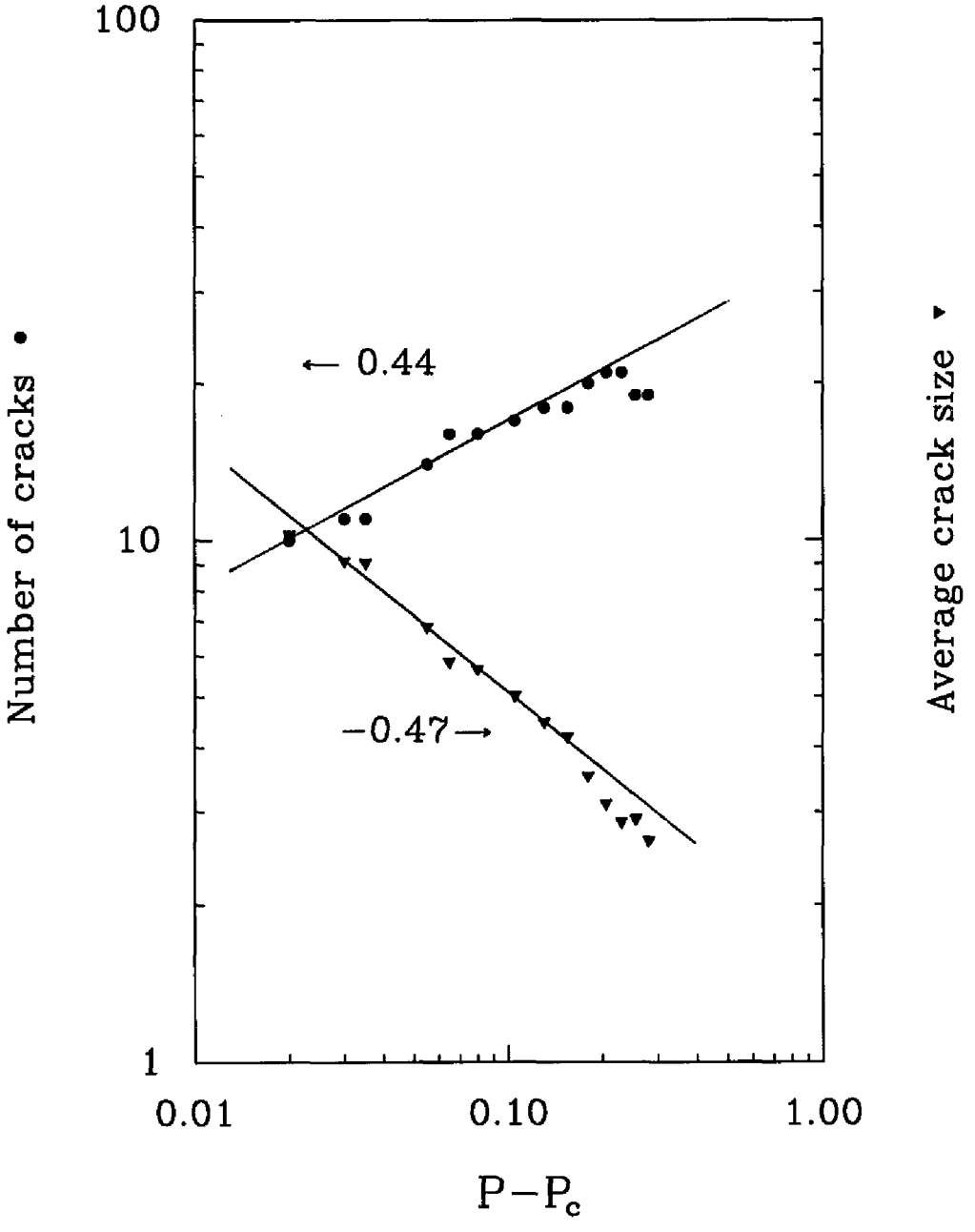

Figure 4.5 Double logarithmic plot of number of the cracks, and average crack size vs $(p\text{-}p_c)$ for the square lattice, with p_c=0.47.

4.5. Weibull Statistical Approach to Fracture Behavior

We considered the 2-D results in terms of the statistical analysis given in section 2.3. In our case, u' can be considered as a constant since in the very dilute region, the cracks produced by random cuts are widely distributed and each cut generates a new crack in the sample. Consider u'= 1 under these circumstances. As n, the crack density, increases, the modal local strength will decrease dramatically as we can see from equation (2.37).

If $(1-p)$ represents the percentage of the bonds being cut, the crack density, n, which is equal to the number of the cracks in specimen, can be written as:

$$n = N \cdot (1-p) \tag{4.42}$$

where N is the total number of the bonds for a perfect sample, which is equal to 1230 in Honeycomb lattice. The modal value of local fracture strength will be:

$$\sigma_u = (k/u'^{1/2})[N \cdot (1-p)]^{-1/2\alpha} \tag{4.43}$$

Since k, u' and N are constants, σ can be written in a simple form:

$$\sigma_u = B \cdot (1-p)^{-1/2\alpha} \tag{4.44}$$

where B is a constant. The value of α is unknown. As we mentioned before, $1/\alpha$ is a measure of the dispersion of the crack density distribution, so that the larger α, the more uniform the crack size.

If we have two samples with p_1 and p_2 respectively, we can rewrite the equation (4.44) as follows:

$$\sigma_1/\sigma_2 = [(1-p_1)/(1-p_2)]^{-1/2\alpha} \tag{4.45}$$

or,

$$\ln(\sigma_1)-\ln(\sigma_2) = 1/2\alpha \cdot [\ln(1-p_1)-\ln(1-p_2)] \tag{4.46}$$

The double log plot will determine the α value of such a system. We emphasize that we assumed that α is a constant in such a dilute region. The double log plot of Log(1-p) vs Log(σ) in the region of $0.98<p<0.9995$ shows that α value is about 6 under this assumption (Figure 4.6).

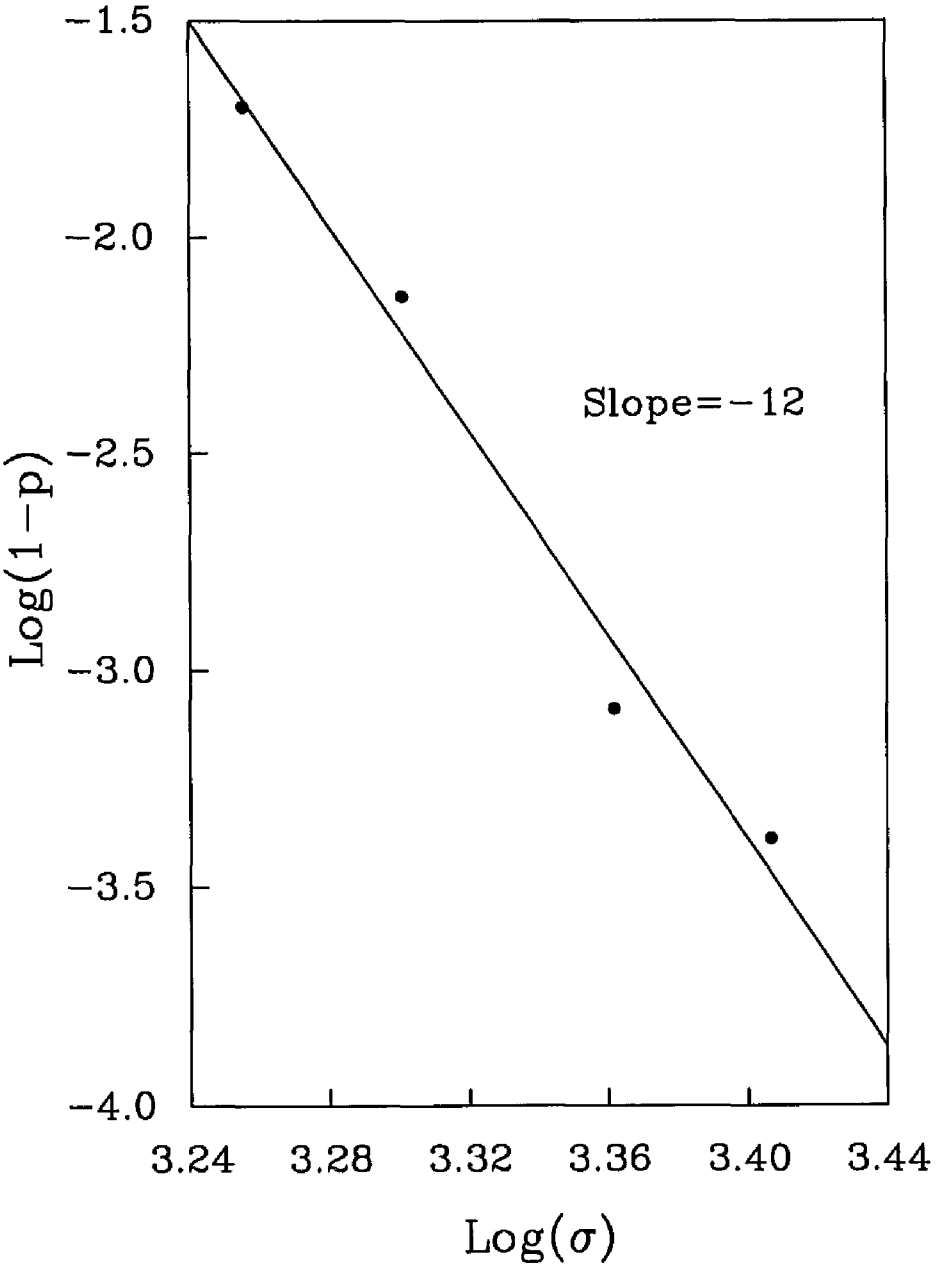

Figure 4.6 Double logarithms plot of (1-p) vs fracture stress, σ, for the honeycomb lattice in the region of $0.98<p<0.9995$. The slope equals -12, which leads to $\alpha=6$.

As discussed, $1/\alpha$ is a measure of the dispersion of the crack density distribution, and the larger α, the more uniform the crack size. For the very dilute region, all the crack sizes are unity. Therefore, we expect that the fracture behavior of the sample in the very dilute region will be brittle. When we examined the load-displacement curve, plastic deformation was relatively small before the load reached the maximum value corresponding to the first broken bond. In the region of $0.98<P<0.9995$, once one bond was broken, the sample failed by a bond-by-bond chain reaction. We then examined the mechanism of such brittle fracture.

The distribution function of the tensile strength, σ_t, is represented by:

$$F(\sigma_t)=1-\exp[-(\sigma_t/\sigma_{t0})^{2\alpha}] \tag{4.47}$$

Here, we replace σ with σ_t and let $\sigma_{t0}=\sigma_u n^{-1/2\alpha}$ in equation 2.34, then σ_{t0} represents the effective modal value of local strength, which counts the weak interaction between the cracks (remember σ_u is the modal value of local strength with crack length, u, without counting the effect of other cracks). When the crack density increases, the effective local strength value decreases by the factor of $n^{1/2\alpha}$. For simplification, let:

$$F^*(\sigma_t)=1-F(\sigma_t)=\exp[-(\sigma_t/\sigma_{t0})^{2\alpha}] \tag{4.48}$$

$$\ln[-\ln F^*(\sigma_t)]=2\alpha[\ln\sigma_t-\ln\sigma_{t0}] \tag{4.49}$$

$\sigma_{t0}=\sigma_u n^{-1/2\alpha}$ implies that there is a relation between the modal tensile strength of specimens of area A_1 and A_2 of the form:

$$\sigma_{t01}/\sigma_{t02}=(A_2/A_1)^{1/2\alpha} \tag{4.50}$$

The area effect on the distribution of tensile strength follows from equation (4.48), in which σ_{t0} is replaced by $\sigma_{u'}(A/A_0)^{-1/2\alpha}$:

$$\ln[-\ln F^*(\sigma_t)] = 2\alpha(\ln\sigma_t - \ln\sigma_{u'}) + \ln(A/A_0) \tag{4.51}$$

The probability of failure, P_F, of a tensile specimen under an applied tensile stress, σ, is obtained from equation (4.52), equation (4.53), and equation (4.54), as follows:

$$P_F = Pr\{\sigma_t \leq \sigma\} = 1 - \exp[-(\sigma/\sigma_{t0})^{2\alpha}] \tag{4.52}$$

$$\ln(\sigma/\sigma_{t0}) = (1/2\alpha)\ln[-\ln(1-P_F)] \tag{4.53}$$

$$2\alpha\ln(\sigma/\sigma_{t0}) = \ln[-\ln(1-P_F)] \tag{4.54}$$

where σ_{t0} is the modal value of local strength. For a given σ, if σ_{t0} increases, P_F, the probability of fracture decreases implying that $\exp[-(\sigma/\sigma_{t0})^{2\alpha}]$ increases, or $(\sigma/\sigma_{t0})^{2\alpha}$ decreases where σ/σ_{t0} must be positive:

$$0 \leq (\sigma/\sigma_{t0}),$$

Figure 4.7 shows the probability of failure, $P_F(\sigma)$, as a function of σ/σ_{t0}. The second derivative of $F(\sigma)$ with respect to (σ/σ_{t0}) is always negative as long as the latter is greater than one. The larger that the α is, the faster the probability of failure approaches one.

The larger the value of α, the narrower the dispersion of the distribution of element strength in the solid. A uniform element strength tends toward brittle type

behavior since most of the elements weaken at virtually the same instant. Figure 4.7 shows the dependence of the failure probability, $F(\sigma)$, on the applied stress σ/σ_{t0}. The larger α, the quicker $F(\sigma)$ approaches 1. For larger α, at small σ/σ_{t0}, $F(\sigma)$ is small. As σ/σ_{t0} becomes greater than 1, $F(\sigma)$ rises very quickly for large α. This relationship is indicative of brittle response. On the other hand, for small α, indicating a large dispersion on distribution width, $F(\sigma)$ is somewhat larger. In this case, as σ/σ_{t0} increases there is no dramatic change in the rate of approach of $F(\sigma)$ toward 1, *i.e.*, the second derivative of $F(\sigma)$ with respect to (σ/σ_{t0}) actually decreases as $F(\sigma)$ approaches to 1. Physically, this behavior reflects the finite possibility that failure of the weaker elements could result in failure of sample. In this event, the sample unfolds or stretches out during fracture and this process may be consider to be ductile.

Therefore, we might consider that there is a transition between ductile and brittle behavior which could be distinguished by the sign of the second derivative of $F(\sigma)$ with respect to (σ/σ_{t0}) as they across the value of $\sigma/\sigma_{t0}=1$. If the signs of the second derivative are the same, ductile fracture is indicated; otherwise, the fracture is brittle. In other words, we might say that the fracture behavior of a system would be considered to be more brittle if it had a larger α value. Physically, ductile materials undergo plastic deformation under external stress; therefore, to stretch the test specimen, more load is needed as there is greater plastic deformation. This is the reason that the probability of failure increases slowly with increasing external load. For perfect brittle materials, there is no plastic deformation in the specimen while it is undergoing the external stress, so that the chances of failure increase much faster with increasing load, and fracture occurs with 0% change in cross-section area.

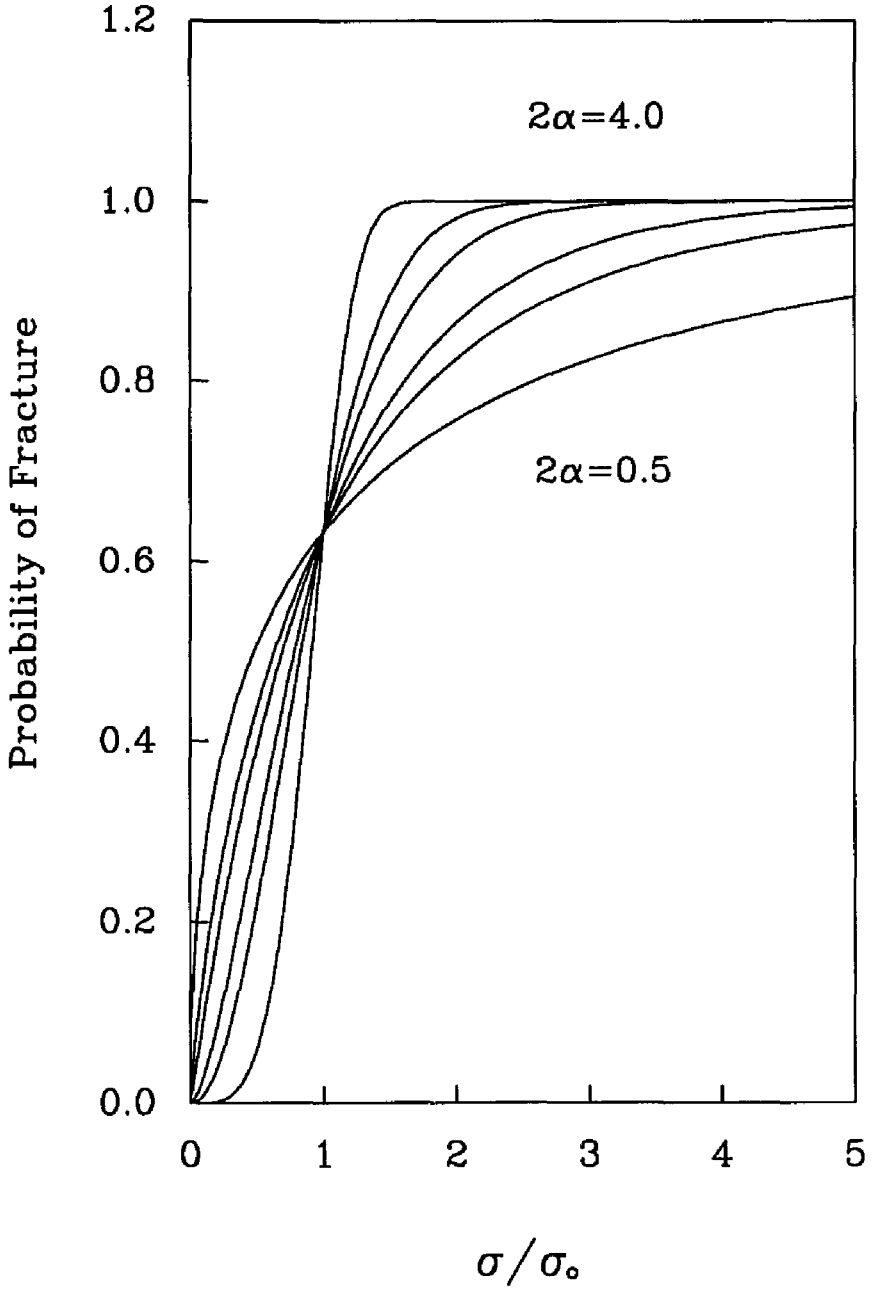

Figure 4.7 Probability of fracture, $F(\sigma)$ in the Weibull distribution, vs (σ/σ_{t0}), with 2α=0.5, 0.8, 1.0, 1.5, 2.0 and 4.0, respectively.

In order to have a specified probability of failure $F(\sigma)$ for the specimens (a constant $F(\sigma)$), the necessary relation between σ/σ_{t0} and the parameter α is of the form:

$$2\alpha\ln(\sigma/\sigma_{t0}) = \ln[-\ln(1-P_F)] = \text{constant} \tag{4.55}$$

which leads to:

$$\sigma_1/\sigma_2 = \sigma_{t01}/\sigma_{t02} = (A_{02}/A_{01})^{1/2\alpha} = (n_2/n_1)^{1/2\alpha} \tag{4.56}$$

Here, n_1, and n_2 represent the crack density for two different specimens, 1 and 2. Solving equation (4.56) for 2α yields:

$$2\alpha = [\ln(n_2)-\ln(n_1)]/[\ln(\sigma_1)-\ln(\sigma_2)] \tag{4.57}$$

This equation is exactly the same as equation (4.46) and which gave $\alpha \approx 6$ (see Figure 4.6)

Such a large α value indicates that the fracture will be brittle. As shown by the load-displacement curves, once the first bond of the sample was broken, the sample failed with no further increase in load. Actually, the specimen was so brittle compared with the specimens with low p values, that several (about 5 to 10) bonds broke almost simultaneously creating a huge crack which failed as the displacement increased. These arguments assume:

1. There are only few cracks in the system, and these cracks are all in unit length and uniformly distributed in the specimen.

2. There is no interaction or only the weakest interaction between cracks, so that the effect of a crack in each area element can be analyzed independently of that in any other area element, as if it were the only crack existing in the medium.

3. The strength of an area element is related to the severity of the crack it contains by Griffith's energy criterion.

4. The strength of any specimen is uniquely defined by the strength of the area that contains the most severe crack.

Let us consider what happens in the medium dilute regime. The crack density increases as p decreases or as ϕ increases, and the length of largest crack also increases. This situation is unlike the case in the very dilute region, where the crack length increases so slowly that it is virtually constant, and the crack density increases rapidly. In the medium dilute regime, there is a competition between the increasing crack density and the increasing crack length. Our experimental observations showed that the fracture path always passed through at least one of the largest cracks. Therefore, is the Weibull statistical method still applicable in this region?

In the medium dilute region, if u is the largest crack length in area A_0, and the modal value of crack length ($u' = u \cdot n^{1/\alpha}$) in area $A = n \cdot A_0$ (sample size), then substituting $\sigma_u = k \cdot u^{-1/2}$, $k = (2E\gamma/\pi)^{1/2}$, and $\sigma_{t0} = \sigma_u \cdot n^{-1/2\alpha}$ into equation (4.47), we obtain:

$$F(\sigma) = 1 - \exp[-B \cdot n \cdot (\sigma \cdot (u/E)^{1/2})^{2\alpha}] \qquad (4.58)$$

where B is a constant. To have a specified probability of failure, $1-F(\sigma)$ should be a constant. Taking a logarithm of $1-F(\sigma)$, yields:

$$2\alpha \cdot \ln[\sigma(u/E)^{1/2}] = -\ln(n) + \text{constant} \qquad (4.59)$$

and 2α can be obtained from this relation by a graphical method.

σ and E can be obtained from the load-displacement curves for the particular p, and u can be considered to be the largest crack length in the area A_0, which is also the largest crack(s) in the sample. In the very dilute regime, all of the cracks are almost the same size and they also occupy the same area (A_0), and so A/A_0 is the crack density. In the medium dilute regime, crack sizes vary over a factor 3~9, so that A/A_0 no longer represents a simple crack density. In effect, A/A_0 represents a density of the relevant cracks, *i.e.*, there may be many cracks of varying size in the sample but only the largest crack of length u is consider to be the relevant to the analysis. Justifying $n=A/A_0$ into equation (4.60) (let A_0 be the size of the largest crack) allows us to determine a value for α. Figure 4.8 shows that $\alpha\approx 2.15$ in the medium dilute region. Comparing this result with the one in the very dilute regime ($\alpha\approx 6$), we can say that in the very dilute regime the fracture behavior is quite brittle while in the medium dilute region the behavior of the material is less brittle.

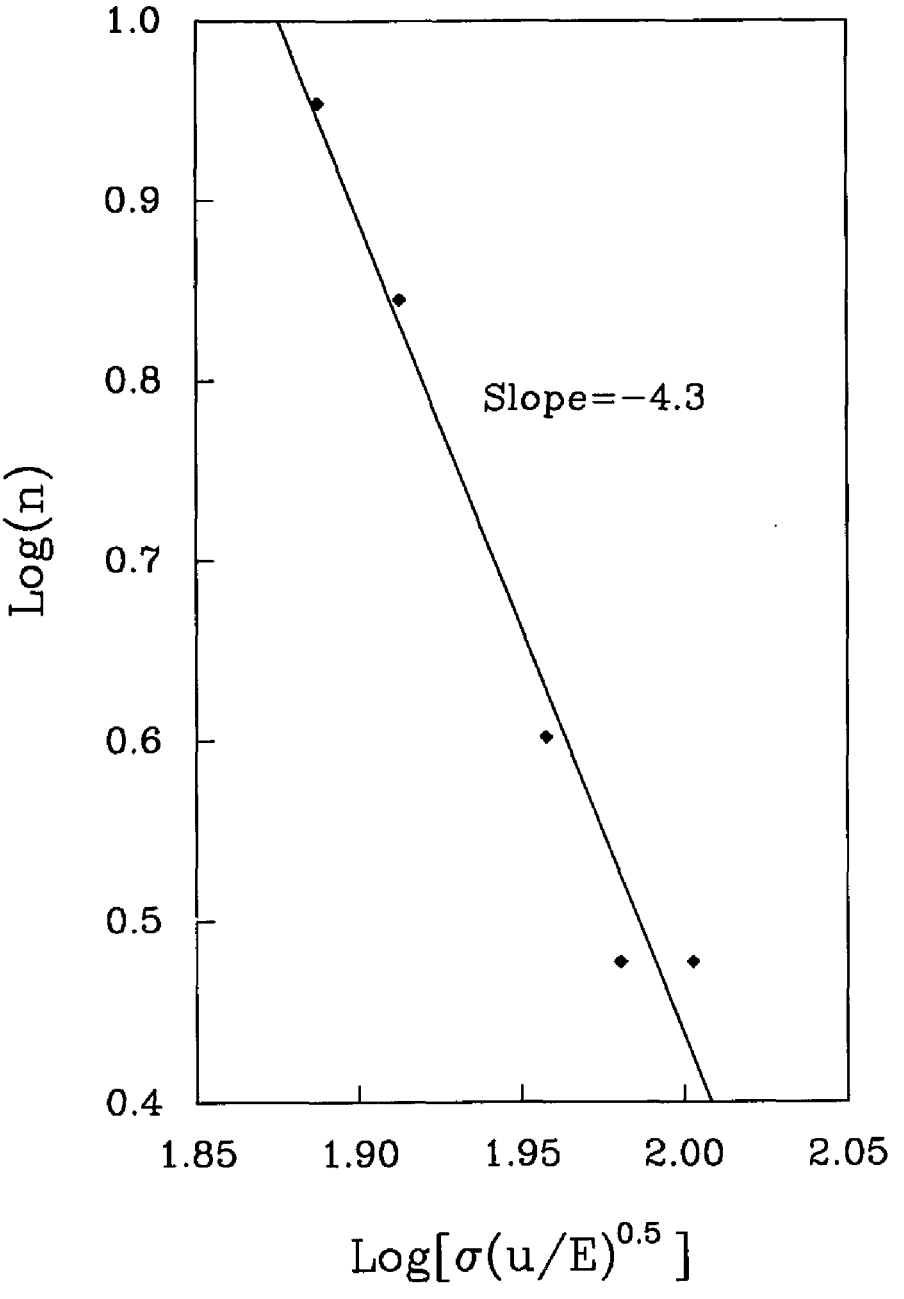

Figure 4.8 Double logarithmic plot of number of cracks, n, vs $\sigma(u/E)^5$ for the honeycomb lattice in the region of $0.88<p<0.98$, the slope equals -4.3, which gives $\alpha \approx 2.15$.

Qualitatively speaking, this behavior might due to competition between increasing crack size and crack density in this medium dilute region. In the very dilute region, where the corresponding α value is 6, when p decreases, crack density increases but the crack size or the crack length keeps as a constant (almost): but in the medium dilute region, the new cut may either (a) increase crack density by forming a new crack, or (b) increase the size of a crack by connecting two single cracks to form a larger one or extend the length of a single crack. This competition favors an increase in crack size rather than in crack density, and this might be the reason that α value drops in the medium dilute region.

From our experiments with the square lattice, We see that the fracture stresses and elastic modulus decrease linearly in the region in the p values from 0.95 to 0.70. therefore equation (4.57), the result of the Weibull distribution function described by equation (4.47), will be applied.

The double logarithm plot of crack density vs fracture stress in Figure 4.9 showed that $\alpha \approx 2.1$ in the region of $0.976 > P > 0.92$, and that $\alpha \approx 0.6$ in the region of $0.92 > P > 0.724$. These values are in good agreement with our observations of the fracture behavior of the samples. In the very dilute region, the fracture occurred abruptly, indicating that the specimens were quite brittle compared with the specimens with p values of $0.724 < P < 0.92$.

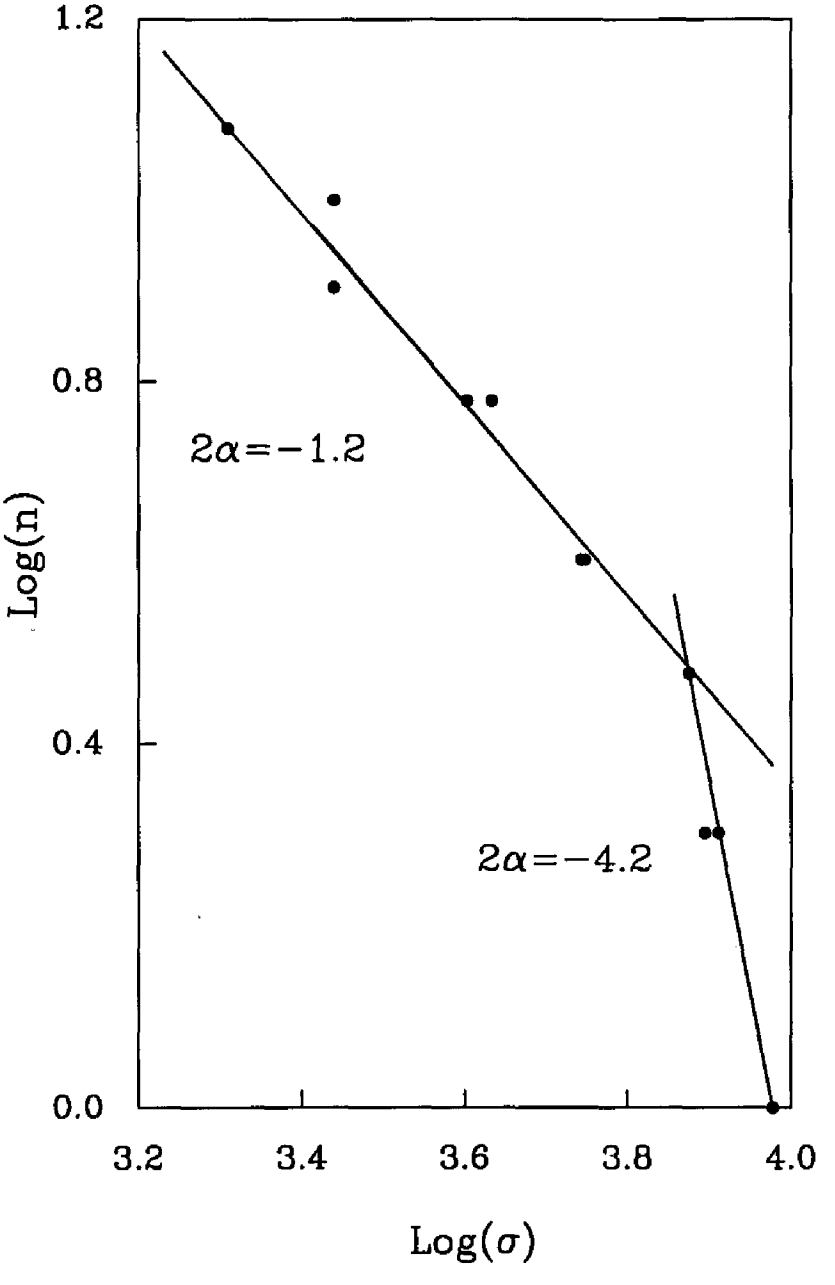

Figure 4.9 Double logarithmic plot of number of the cracks, n, vs fracture stress, σ, for the square lattice in the region of $0.724 < p < 0.976$.

5. 3-D EXPERIMENTS

5.1. Introduction

Three point bend tests [47, 48] of porous gold beams prepared by an electrochemical dissolution process [49, 50] were carried out to study the elastic modulus and the fracture behavior of porous solids in three dimensions. Selective dissolution [51, 52, 53] of the silver-gold (Ag-Au) alloy in perchloric acid leaves a porous Au structure [54, 55, 56]. The size scale of the porosity could be altered by varying annealing temperatures and times. Samples with different structures resulting from dealloying and subsequent annealing were characterized by the scanning electron microscope, digital image analysis, and by energy dispersion X-ray analysis.

The characterization of the samples suggested that virtually all of the Ag was removed from the Ag-Au alloy by dissolution. Annealing of the as-corroded material led to self-similar coarsening of the de-alloyed structure. Mechanical testing showed that samples with larger scale porosity had a lower Young's modulus and a higher fracture stress than samples with finer scale porosity. In addition to these differences in sample behavior, we discovered that there was a ductile to brittle transition dependent on the temperature of annealing.

The variation in the properties of the porous solids are discussed and explained in terms of subtle differences in the distribution of ligament element strength and a brittle-to-ductile transition driven by a size effect.

5.2. Preparation of the Samples

A selective dissolution process was used to prepare the 3-D porous Au samples. Selective dissolution (de-alloying) is the preferential removal of one of the components of an alloy in a corrosion process, which will occur if there is a large enough difference in reactivity between the components. This difference frequently plays an important role in the aqueous corrosion of metal alloys. The reason we chose the Ag-Au alloy is the equal lattice parameters of Ag and Au in the fcc structure. The phase diagram [57, 58] shown in Figure 5.1, displays the perfect solid solubility of the Ag-Au system at all compositions. The lattice parameter of these two FCC elements are 4.078Å for Au and 4.086Å for Ag. In choosing the composition of the alloy, there are many factors to be considered. We tested the de-alloying behavior of a series of compositions (from pure Ag to pure Au) in different concentrations of nitric acid, sulphuric acid, and perchloric acid, by electrochemical polarizing [49, 59] of the alloys. Finally we decided on a 0.45 molar perchloric acid. The gold is the noble element in the alloy and the silver is dissolved out in perchloric via a selective dissolution process. The corrosion or dissolution product, silver-perchlorate, is very soluble in perchloric acid, therefore there is no precipitation at the surface of the sample and no kinetic limitation is placed on the dissolution process.

The virgin alloys were obtained by melting Ag and Au of 99.999% purity at a prescribed composition in vacuum (10^{-3} τ) at 1100°C for 30 minutes, and then homogenizing the sample at 900°C for 170 hours (still under vacuum). This treatment results in a partial annealing out of the as-cast dendritic microstructure. The sample was then mounted in epoxy for the polarization experiments. The counter electrode we used is a platinum sheet with an approximately 8 cm^2 surface area to insure that the area of the working electrode, which is the alloy, is much smaller than that of counter electrode. Figure 5.2 shows a typical experimental set-up.

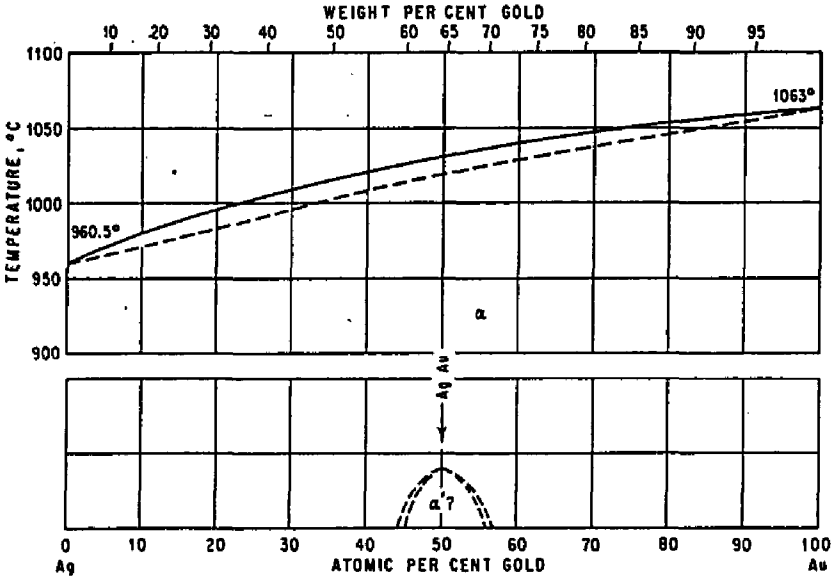

Figure 5.1 Phase diagram of Ag-Au alloy [57].

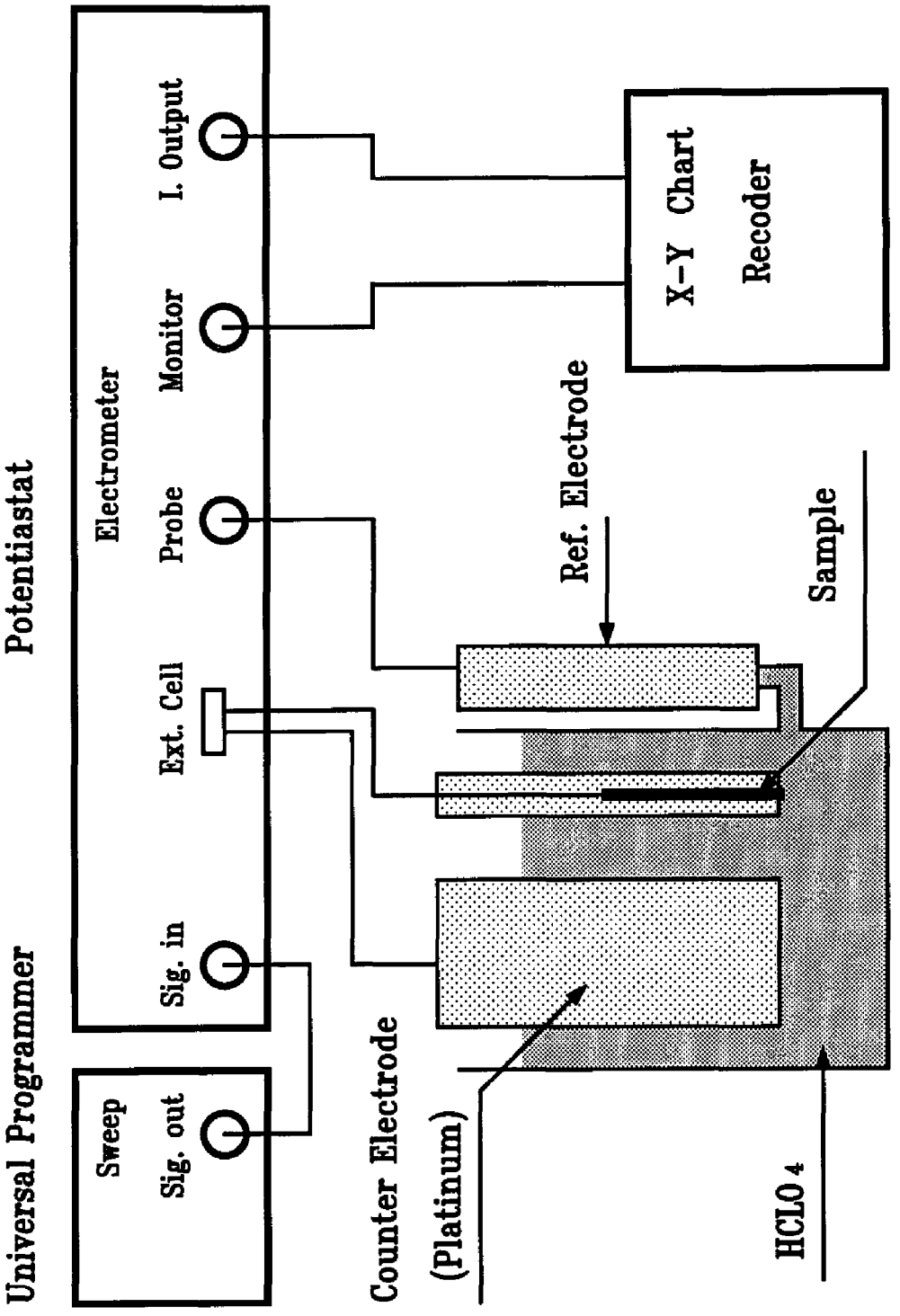

Figure 5.2 Experimental set-up for polarizing and selective dissolution of Ag from Ag-Au alloys.

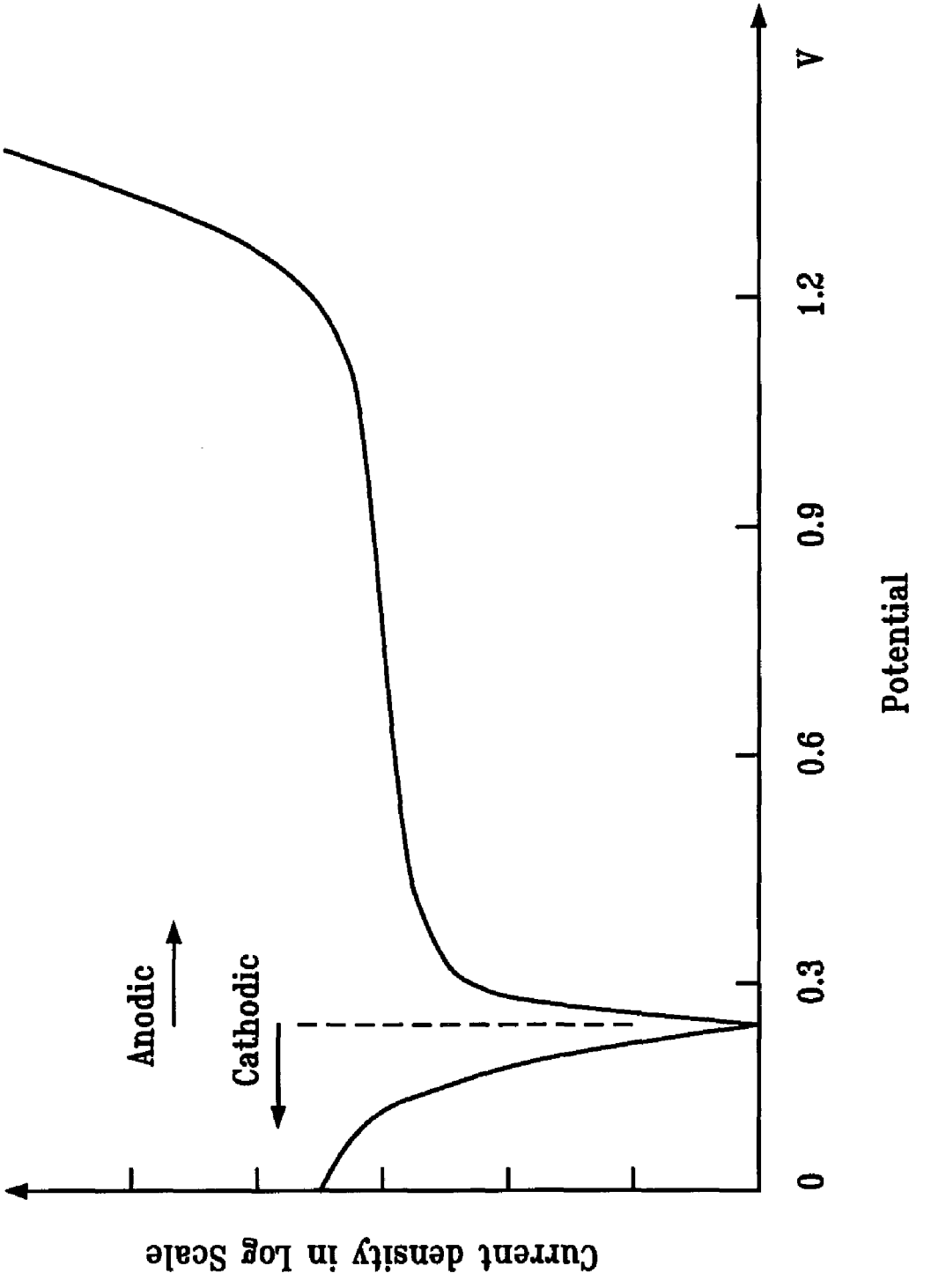

Figure 5.3 Polarization curve of $Ag_{0.7}$-$Au_{0.3}$ alloy in .45 mole perchloric acid.

A typical polarization curve of Ag-Au alloys is shown in Figure 5.3. To dissolve silver out of the alloy and keep gold in the solid, we chose an applied potential of 1.05V. At this potential we can obtain the maximum current density due to the dissolution of the silver and keep electrolyte from oxidizing.

The optimum composition of the alloy we finally decided on was 74 atomic percent silver and 26 atomic percent of gold. Which was chosen after examining a series of specimens within range from 10 at% gold to 90 at% gold. For the alloys with less than 70 at% Ag, we were not be able to effectively remove silver from solid at high rates. For the alloys with more than 80 at% Ag, it was easy to remove all of the silver from alloy (as we determined by X-Ray analysis), but the gold left in the solid could not maintain the geometry of the initial sample and sample collapsed.

After the ingots were prepared, the homogenized material was cut to form the beams with dimensions of 1.5mm x 1.5mm x 30mm. After light mechanical polishing, we re-annealed the specimens again at 900°C for 24 hours to remove any residual stress on the surface due to the mechanical polishing. During the 24-hour de-alloying procedure, the samples were supported on a platinum sheet to prevent gravitational forces from deforming the sample. We used a coulometer to record the charge accumulation resulting from dissolution to ensure that de-alloying was complete. The dealloyed sample was then transferred very carefully to a container with distilled water and left for 24 hours to dilute the remaining acid inside the porous specimen. The sample then was transferred to a stainless steel case and for annealing. Early in the work, we simply put the sample on a quartz plate and annealed it in the furnace; however, after annealing, the sample curved or warped which caused cracks to form. The warping might have been caused by surface stress due to temperature gradients which developed in the sample during initial stages of annealing. This problem was solved by using a stainless steel case as shown in Figure 5.4 which constrains the sample, maintaining its configuration during the annealing process. The sample in the stainless

steel case is then transferred into a pre-heated furnace for annealing for 10 minutes at temperatures ranging from 100°C to 800°C.

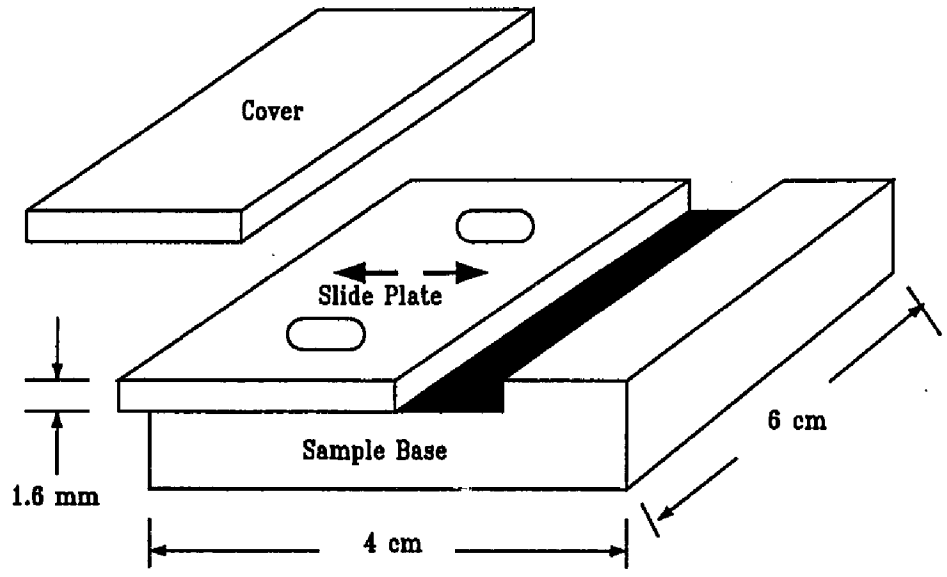

Figure 5.4 Stainless steel sample case for annealing.

5.3. Three-Point Bend Testing

The elastic modulus, E, and fracture stress, σ, for a system composed of a various gold ligament sizes and distributions prepared by dealloying and subsequent annealing were measured by three-point bending tests.

The tests were performed on an Instron universal testing machine. Figure 5.5 shows the experimental setup for the 3-point bending test. The span between the supports is 20 mm. The sample (1.5 x 1.5 x 30 mm porous gold rectangular beam) was freely supported at both ends and a concentrated load was applied at center of the beam. The load cell was attached and fixed on the Instron. While the support base gradually moved up, a concentrated load was applied to the center of the specimen. The deflection at the point of loading of the simple beam and the load were measured. The elastic modulus and fracture strength was obtained from the load-displacement curve. When a beam is loaded with transverse concentrated loads, tensile stresses develop on lower side of the neutral surface and compressive stresses develop on the upper side of the neutral surface. This loading causes the beam to curve and therefore to deflect from its original unstressed position.

Let L represent the span of the supports or the "length" of the beam, E, the elastic modulus of the beam, b, the width of the beam, and h, the depth of the beam (the cross section area of the rectangular beam then is b•h). Consider the deflection of a beam with a concentrated load on it [60]. As shown in Figure 5.6, for a small deflection:

$$dy/dx = \tan\theta \approx \theta \tag{5.1}$$

$$ds \approx dx \tag{5.2}$$

$$1/\rho = d\theta/dx = d^2y/dx^2 \tag{5.3}$$

Figure 5.5 Photograph of a three-point bending test. The sample's span is 25 mm.

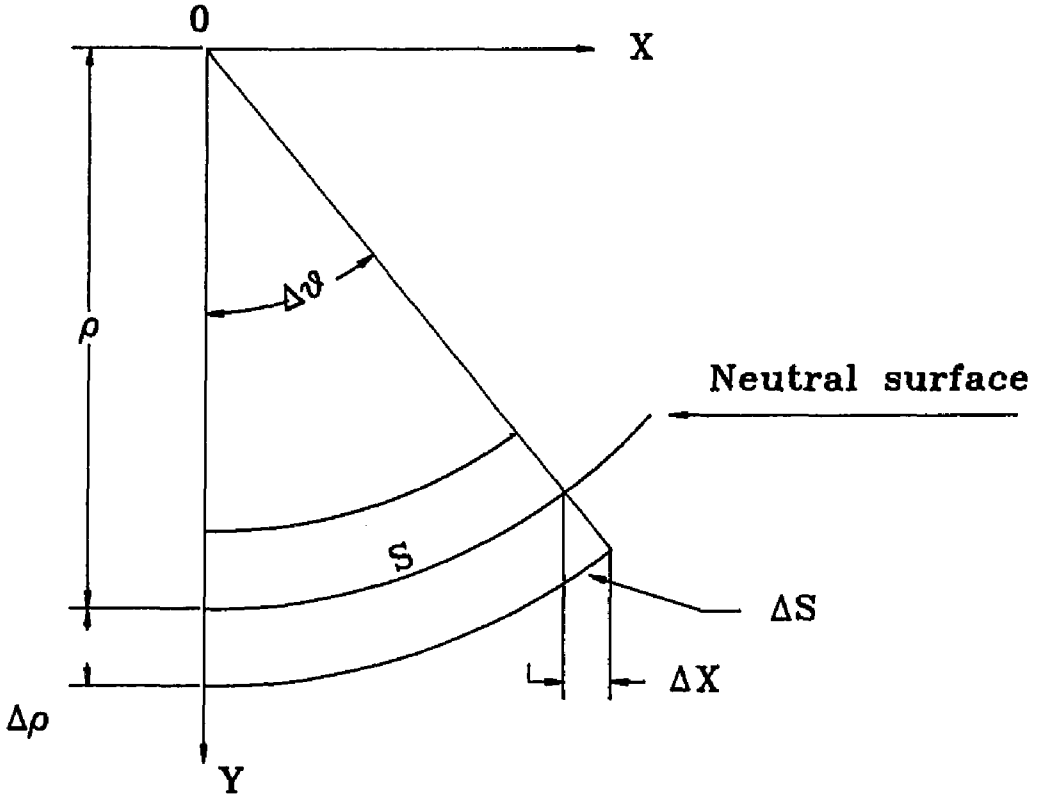

Figure 5.6 Simple beam-bending diagram.

In pure bending, we have [61,62]:

$$1/\rho = M/(E \cdot I) \tag{5.4}$$

$$M = P \cdot b \cdot x/L \tag{5.5}$$

where, M is the bending moment, and I is the moment of inertia with respect to the neutral surface or neutral axis (x-axis, initially). Substituting equation (5.4) and equation (5.5) into equation (5.3):

$$(E \cdot I)d^2y/dx^2 = P \cdot L/4 \tag{5.6}$$

Integrating this equation twice:

$$E = -(P \cdot L^3)/(48I \cdot y) \tag{5.7}$$

or,

$$P = -(4bh^3/L^3) \cdot E \cdot y \tag{5.8}$$

From the load-displacement curve, we measure P vs y. The elastic modulus is determined from the linear part of load-displacement curve.

The fracture load will be defined by the maximum load of the load displacement curve. The fracture strength will be:

$$\sigma(\text{fracture}) = P(\text{fracture}) \cdot 3 \cdot L/(2 \cdot b \cdot h^2) \tag{5.9}$$

5.4. Calibration of the Force Transducer

A Schaevitz model FTD-G-10 10 grams and model FTD-G-100 100 grams force transducer were used to measure the elastic modulus and fracture stress of the beams. These load cells are of the spring type, which means that under a tension or compression, the load cell operates by yielding a displacement. The total displacement we measured in the test is the sum of the displacement undergone by the sample and the displacement of the load cell.

When the sample moves up (supported by base), a compressive force is transferred to the load cell through the central contact point and the transducer pin moves up. The force acting on the load cell is P_1 and the displacement of it is ΔY_1, the force on the center of the beam is P_2 and the displacement of it is ΔY_2. Applying Newton's second law and Hook's law to this series spring system yields:

$$P_1+P_2=0=k_1\Delta Y_1+k_2\Delta Y_2 \qquad (5.10)$$

here, k_1 and k_2 are the spring constants of the force transducer and the beam respectively.

If ΔY represents the total displacement of the system and k represents the spring constant of the system, then:

$$\Delta Y=\Delta Y_1-\Delta Y_2 \qquad (5.11)$$

$$k_2=k_1k/(k_1-k) \qquad (5.12)$$

k could be measured from the elastic part of the load-displacement curve, and k_2, which

is the spring constant of the beam, could be obtained assuming we know the spring constant of the force transducer.

k_1 was obtained from the load cell calibration. We used a rigid steel bar instead of compliant sample as we did in the three-point bending test, so that the displacement we measured was that of the force transducer only. The results for k_1 are:

$$k_1 \approx 120.9 \text{ (g/cm)} \quad \text{for 10 grams transducer} \tag{5.13}$$

$$k_1 \approx 3{,}000 \text{ (g/cm)} \quad \text{for 100 grams transducer} \tag{5.14}$$

We also examined the linearity of the load cells in their calibrated region. The results showed that the deviation is within 0.5%.

5.5. Characterization of the Samples

5.5.1 SEM Results

Scanning electron microscopy and X-ray examination of the composition and porous structure of the porous Au solid show that almost all the Ag in the alloys is removed successfully (the final compositions are less than 6 atomic percent of the Ag and approximately 95 atomic percent of the Au). The various porous structures were obtained by annealing the solid at different temperatures for different times. Figure 5.7 and Figure 5.8 show the 74 atomic percent Ag, and Figure 5.9 shows the 80 atomic percent Ag photomicrographs. The pore size could be increased by three orders by varying the annealing temperature of corroded (at 25°C) porous Au.

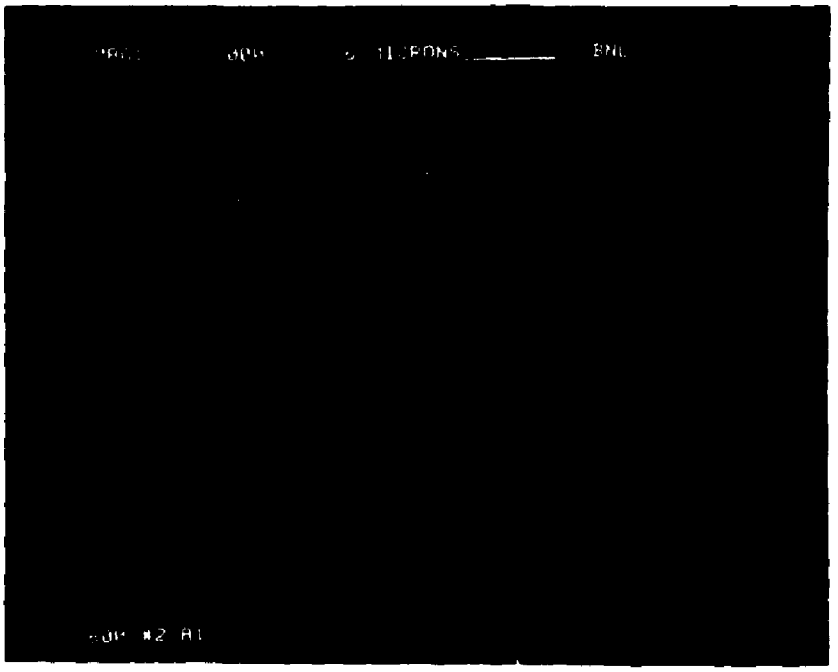

(a) 6 μm

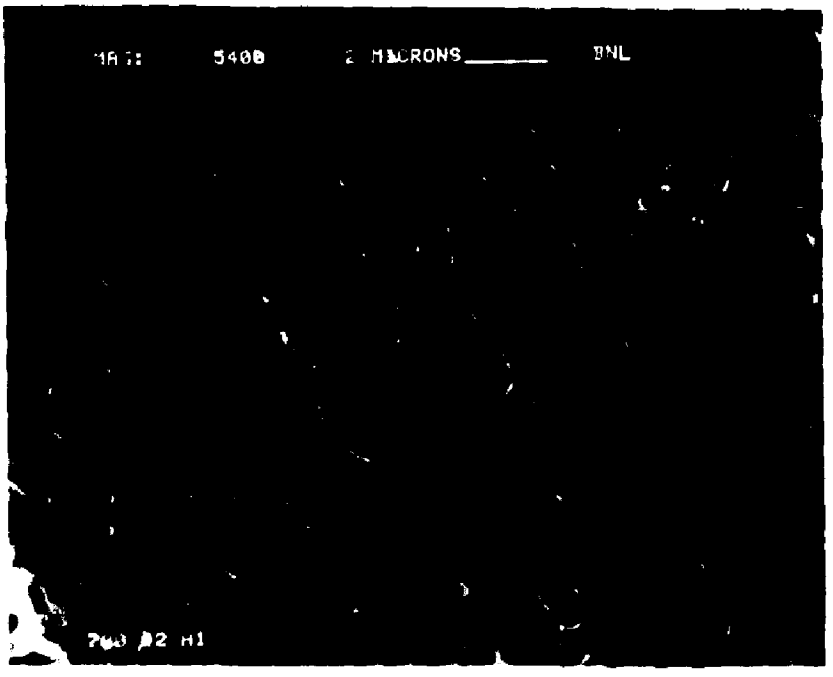

(b) 2 μm

Figure 5.7 SEM photograph of porous Au after de-alloying (form Ag_{74}-Au_{26}). Each sample was annealed for 10 minutes at the following temperature: (a) 800°C, (b) 700°C, (c) 600°C, (d) 500°C, (e) 400°C, and (f) 300°C.

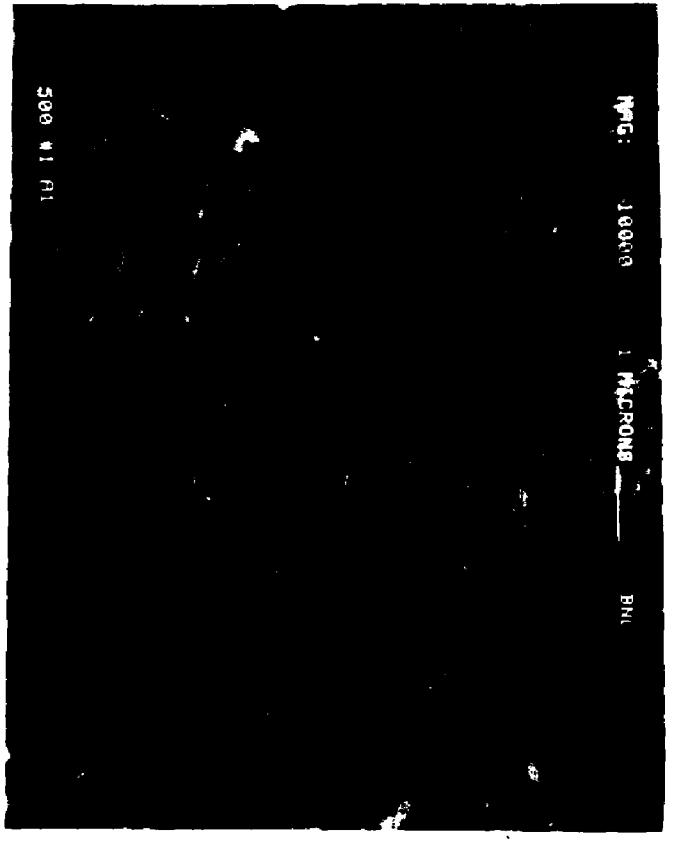

(d) 1 μm

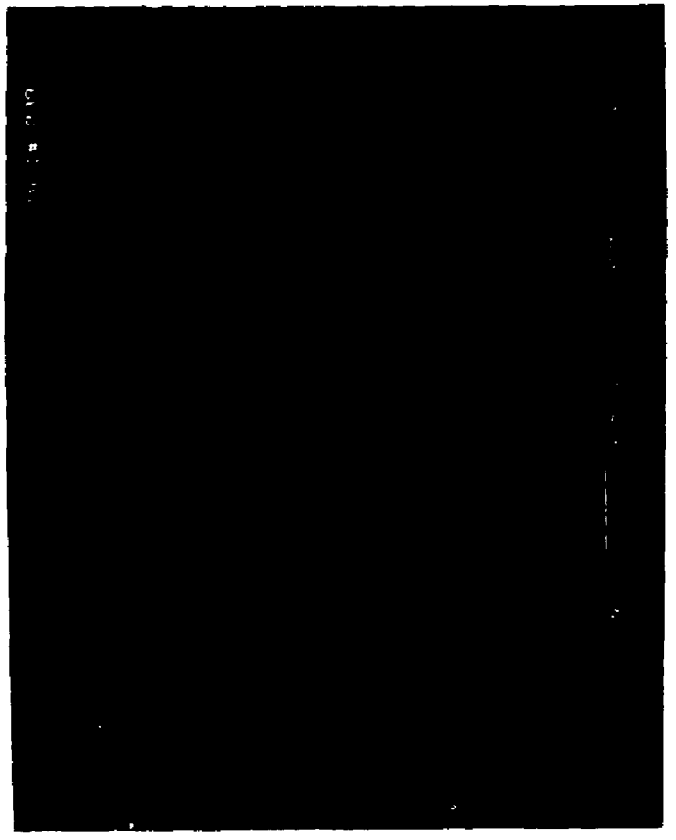

(c) 2 μm

(f) 0.1 μm

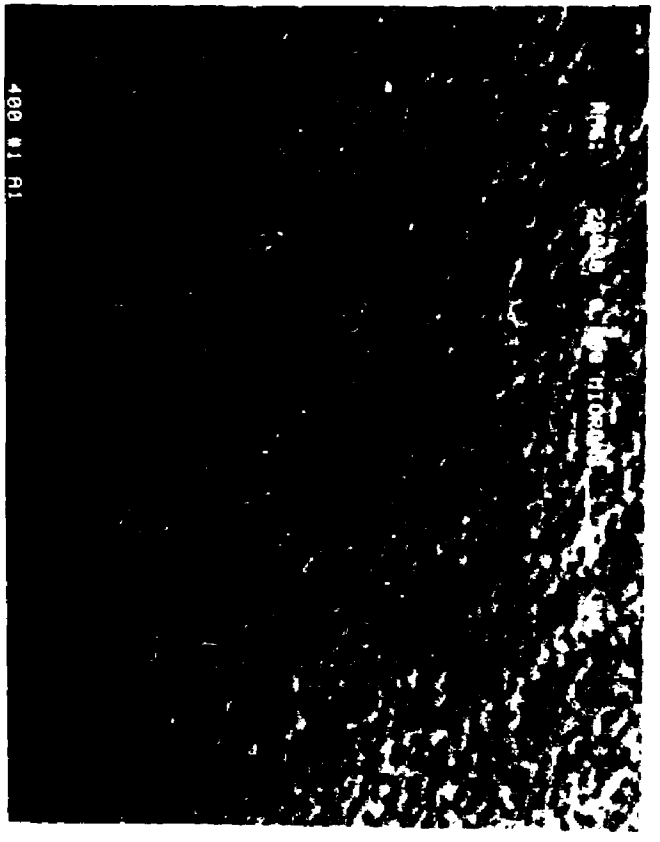

(e) 0.6 μm

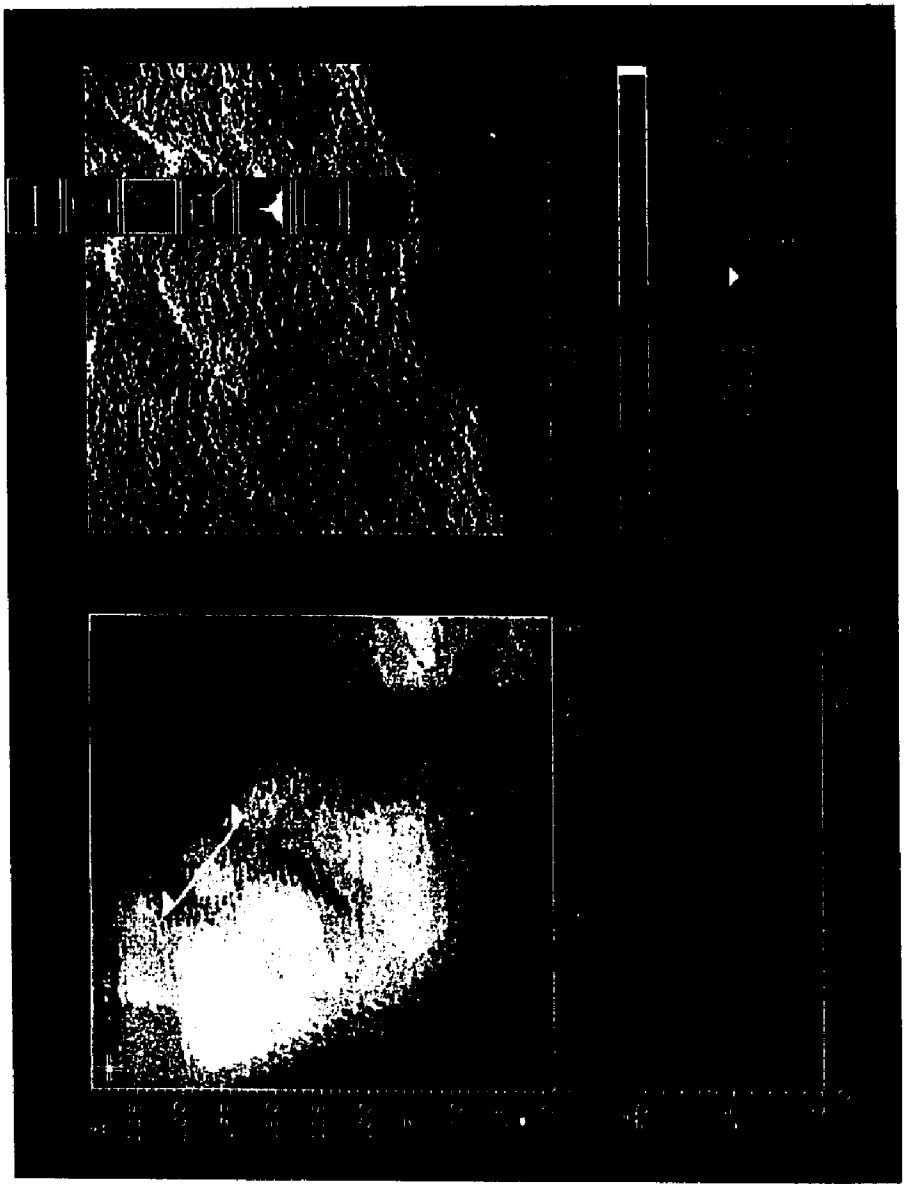

Figure 5.8 STM (scanning tunneling microprobe) picture of porous Au annealed for 10 minutes at 100 °C.

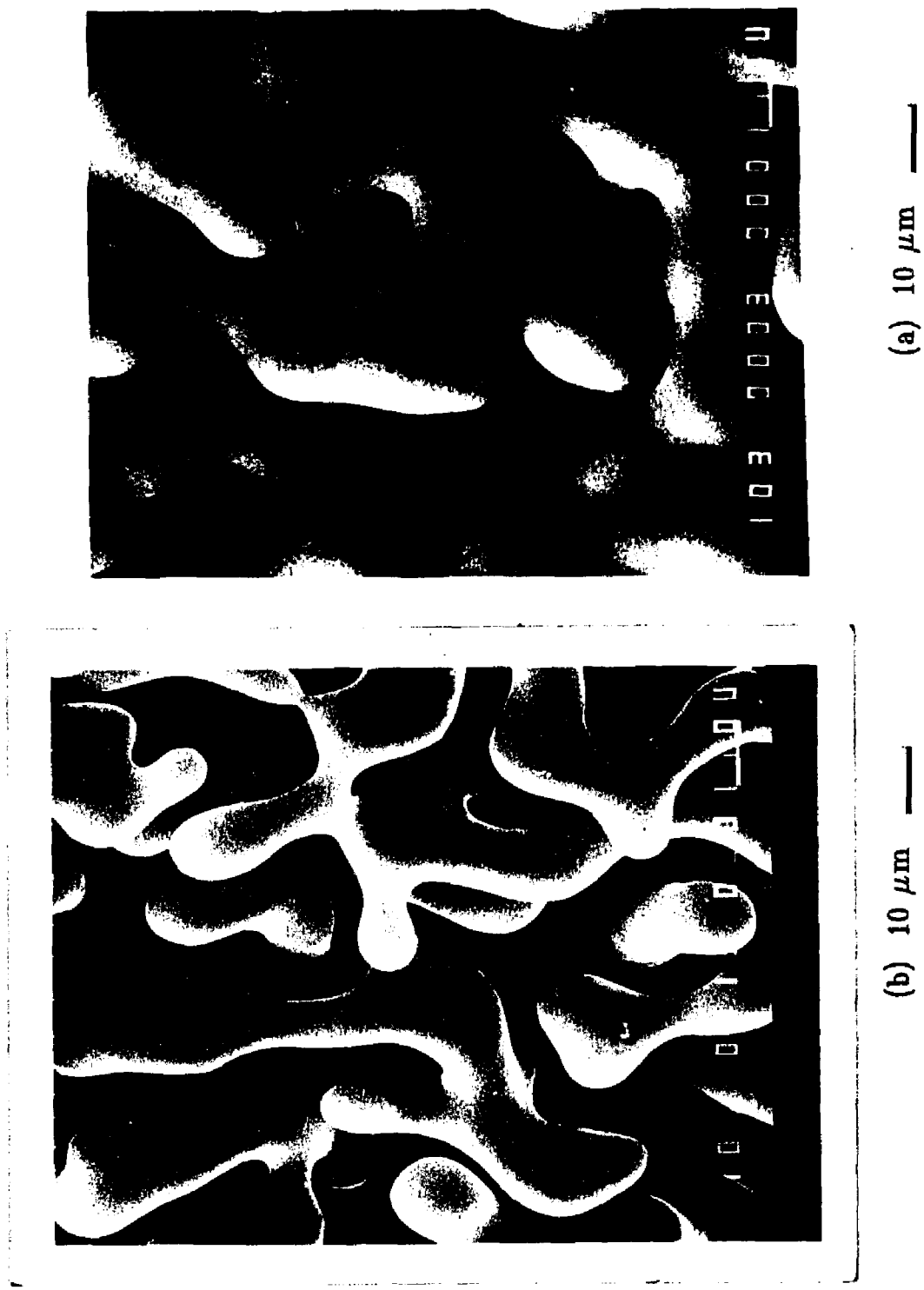

Figure 5.9 SEM photomicrograph of porous Au after de-alloying (Ag_{80}-Au_{20}). Each samples was annealed for 10 minutes at : (a) 800°C, (b) 700°C, (c) 600°C, (d) 500°C, (e) 400°C, (f) 300°C, (g) 200°C, and (f) 100°C.

(d) 10 μm

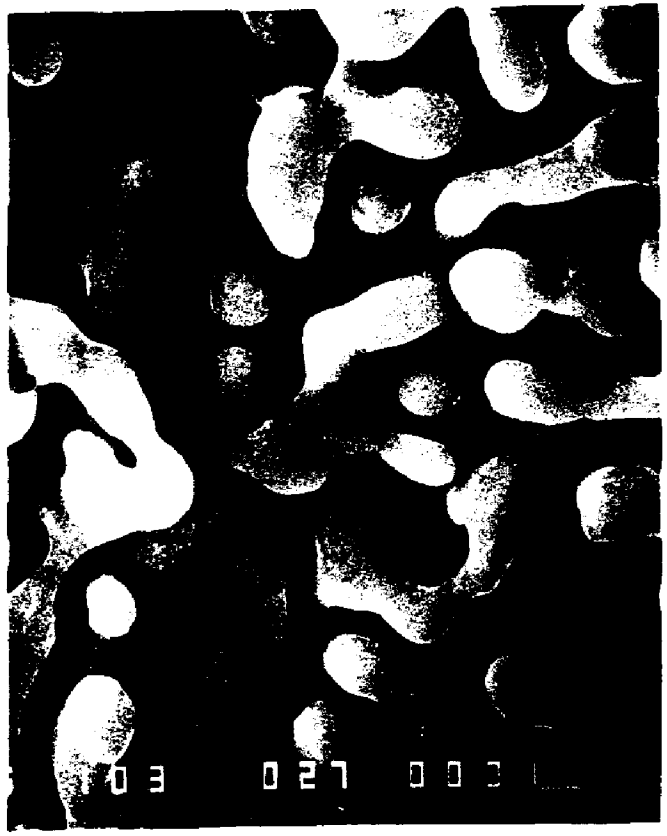

(c) 10 μm

(f) 10 μm

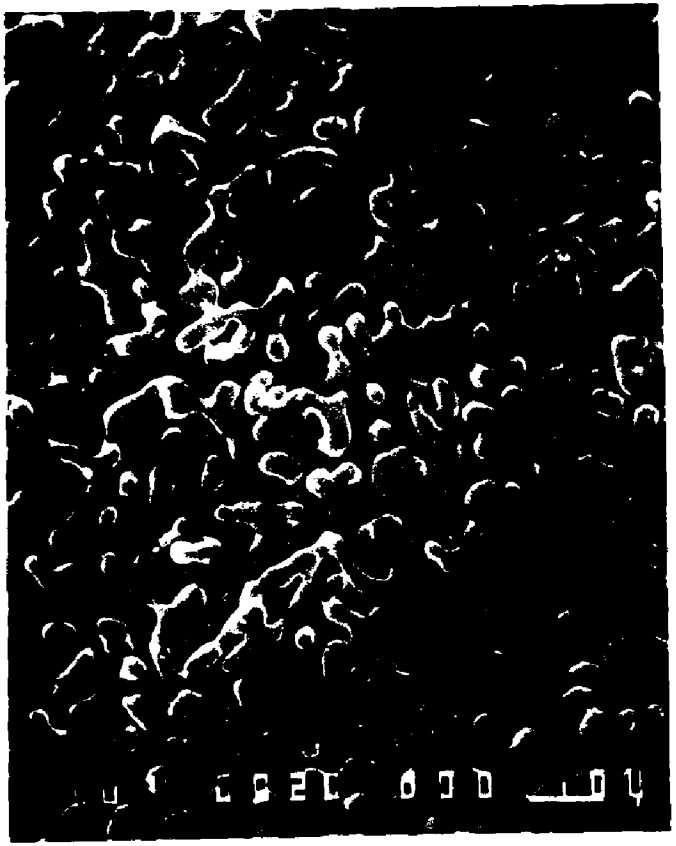

(e) 10 μm

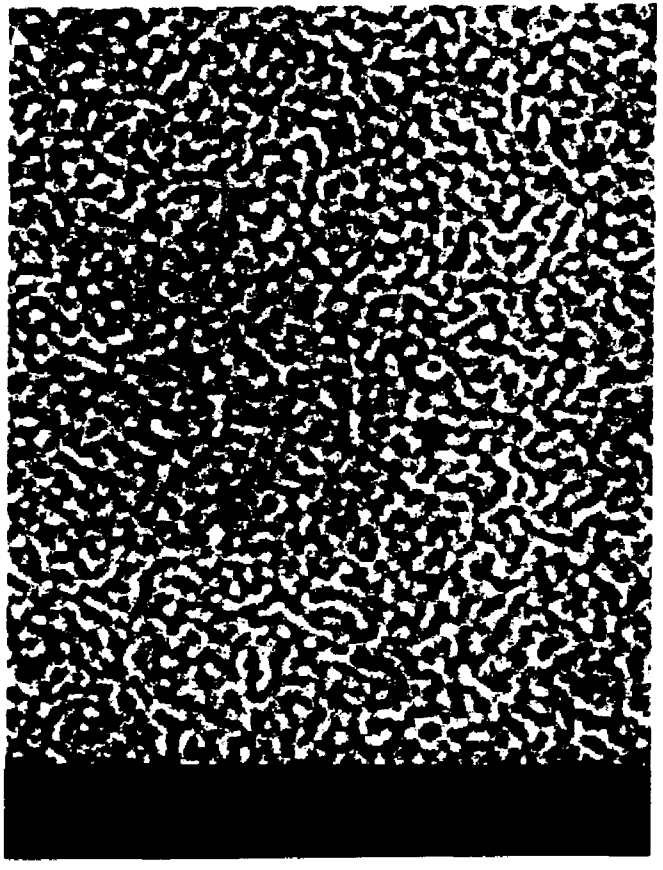

(h) 0.1 μm

(g) 10 μm

5.5.2 Image Analysis

To characterize the samples, we examine the them under a scanning electron microscope (JOEL 35) mapping the image to an image analyzer (Tracor Northern Series X-Ray Analyzer) which enables us to estimate the porosity in any cross-sectional area. A digital image is generated by the image analyzer from the secondary electron image in the microscope. Grey levels [63] are manually set which are used in generating a binary image. Figure 5.10 shows the typical binary image obtained by this procedure.

The grey level is not easy to select for a 3-D sample because the edge of the clusters (islands) usually extend in the z direction. We examined the fracture's cross-section and also checked many other areas of the samples by breaking them in several pieces. We found that the porous structure is uniform in any one sample, which allowed us to pick a reasonably flat surface to perform the digital analysis. We also rotated the images and examined the "isotropy" of the sample. All the samples were very isotropic. As shown in Figure 5.10 (the black area represents the gold island), there is no discontinuity of islands, *i.e*, they are all connected; the white areas are the porous channels in the sample.

We obtained the following information on the pores from the digital image analysis: areas, perimeters, and diameters measured by choosing the center of a pore and then measuring the distance from center to the edge of pore every 22.5°; length, width, and aspect ratio, which is defined as the ratio of length and width of each voids [see Figure 5.11 for the definition].

We then randomly drew lines crossing the binary image of the samples and measured the ligament width, t. The distribution of area and aspect ratio as a function of number of pores are shown in Figure 5.12 and Figure 5.13. Figure 5.14 shows the distribution of ligament width as a function of metallic channels. The similar shapes of these three distribution indicates the similar structure of the porous Au solids.

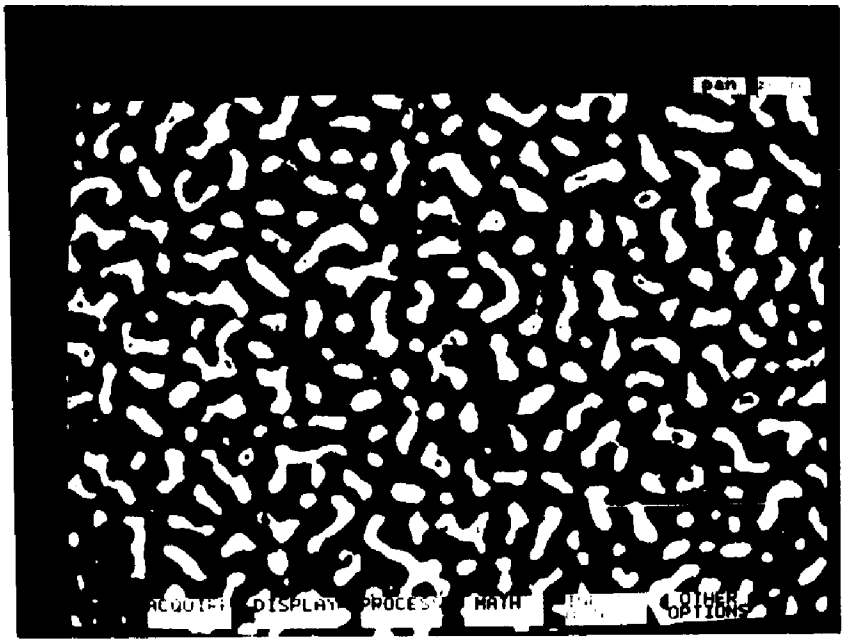

Figure 5.10 Binary image of the porous Au.

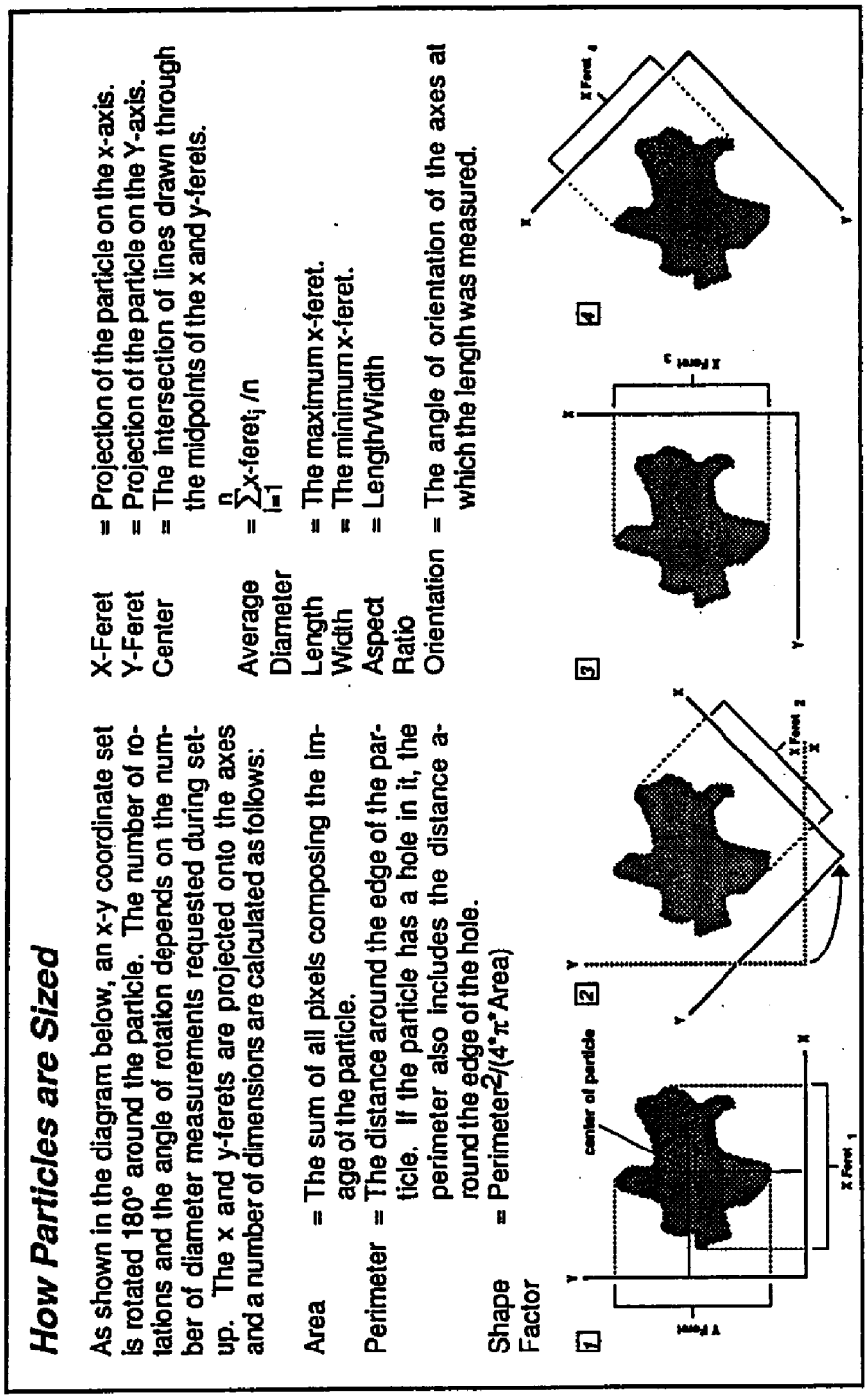

Figure 5.11 The definition of the digital image analysis terms from [63].

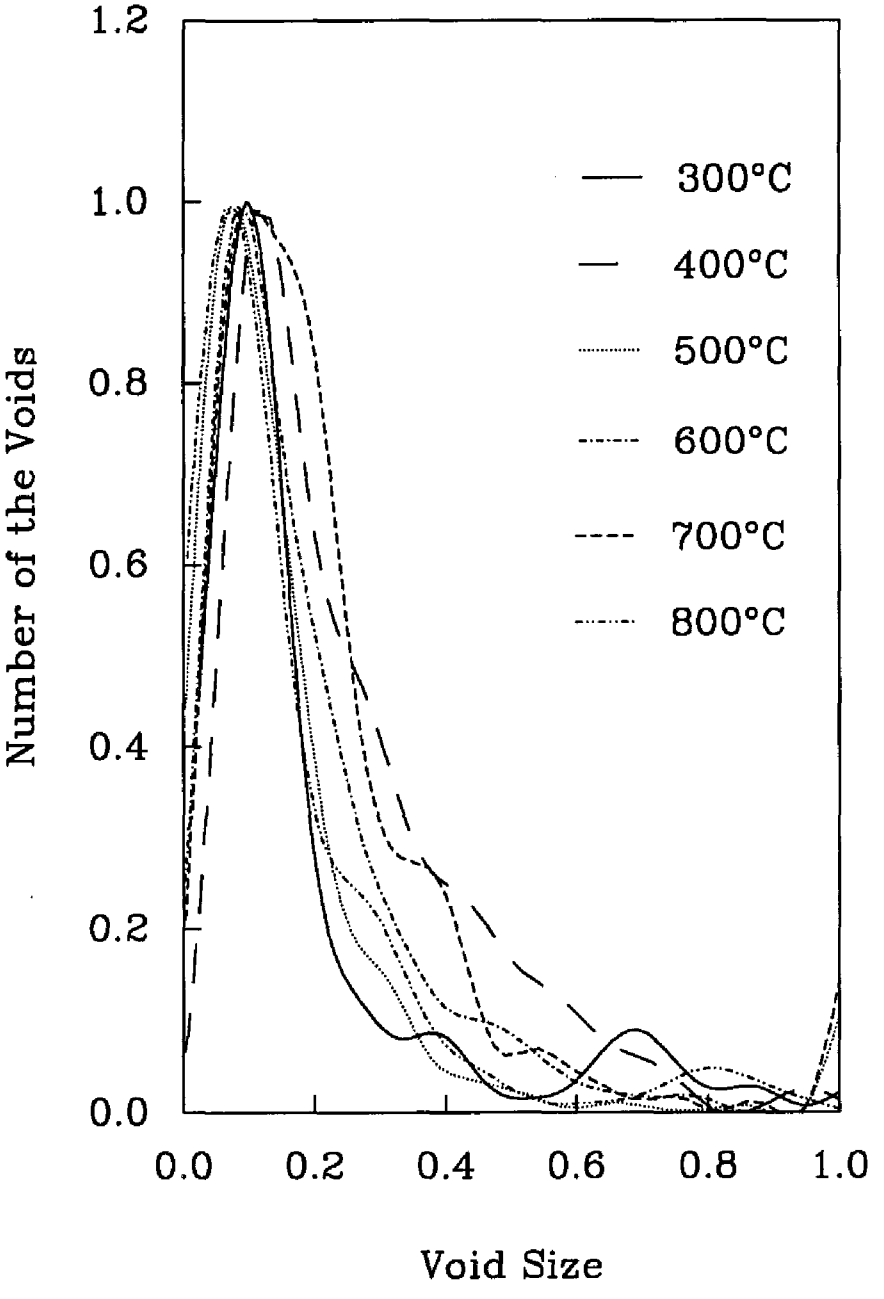

Figure 5.12 The normalized voids-size distribution of porous Au formed from $Ag_{0.74}$-$Au_{0.26}$ alloy. The alloys were annealed for 10 minutes at indicated temperatures.

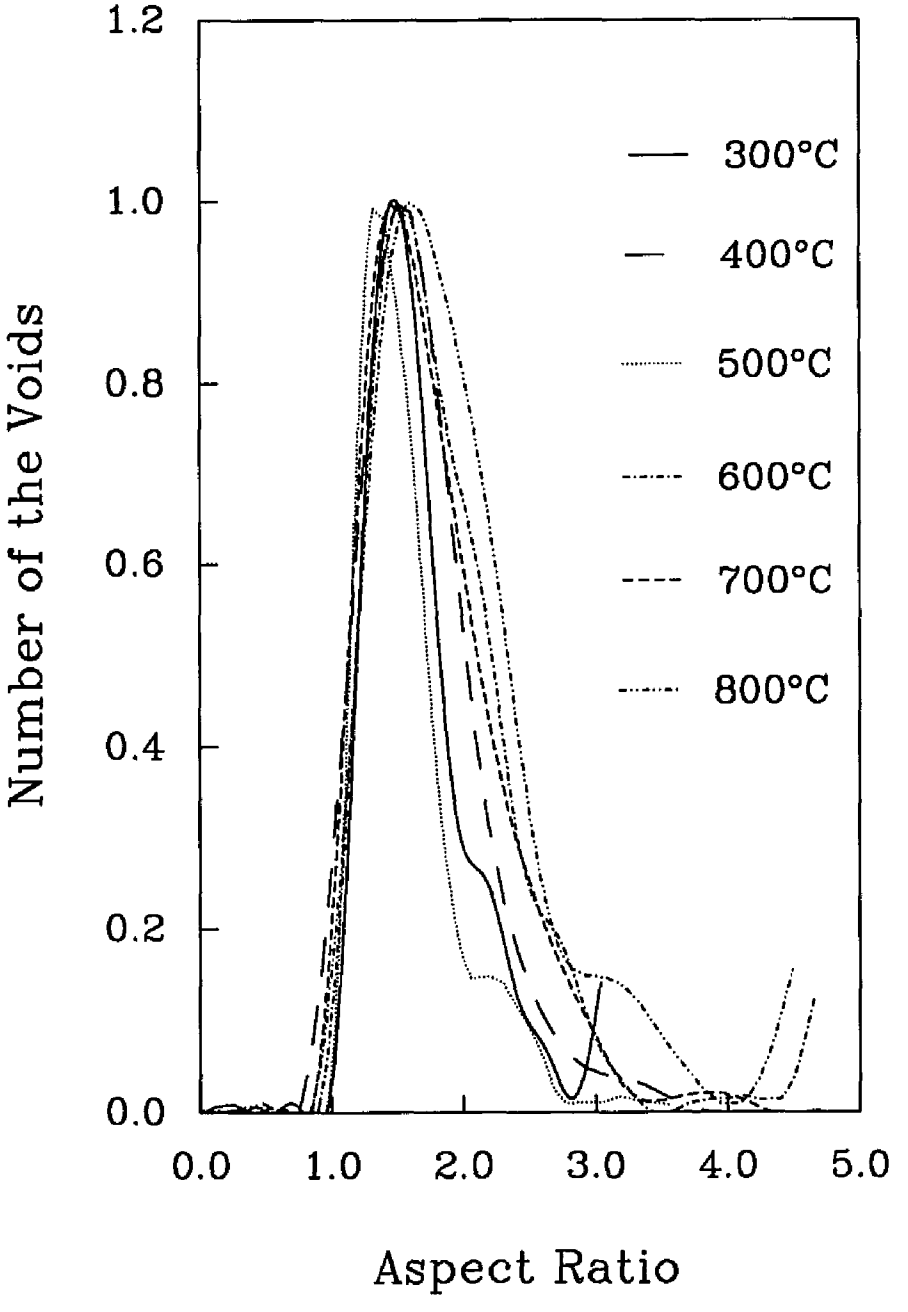

Figure 5.13 The normalized aspect-ratio distribution of porous Au formed from $Ag_{0.74}$-$Au_{0.26}$ alloy. The alloys were annealed for 10 minutes at the temperatures shown.

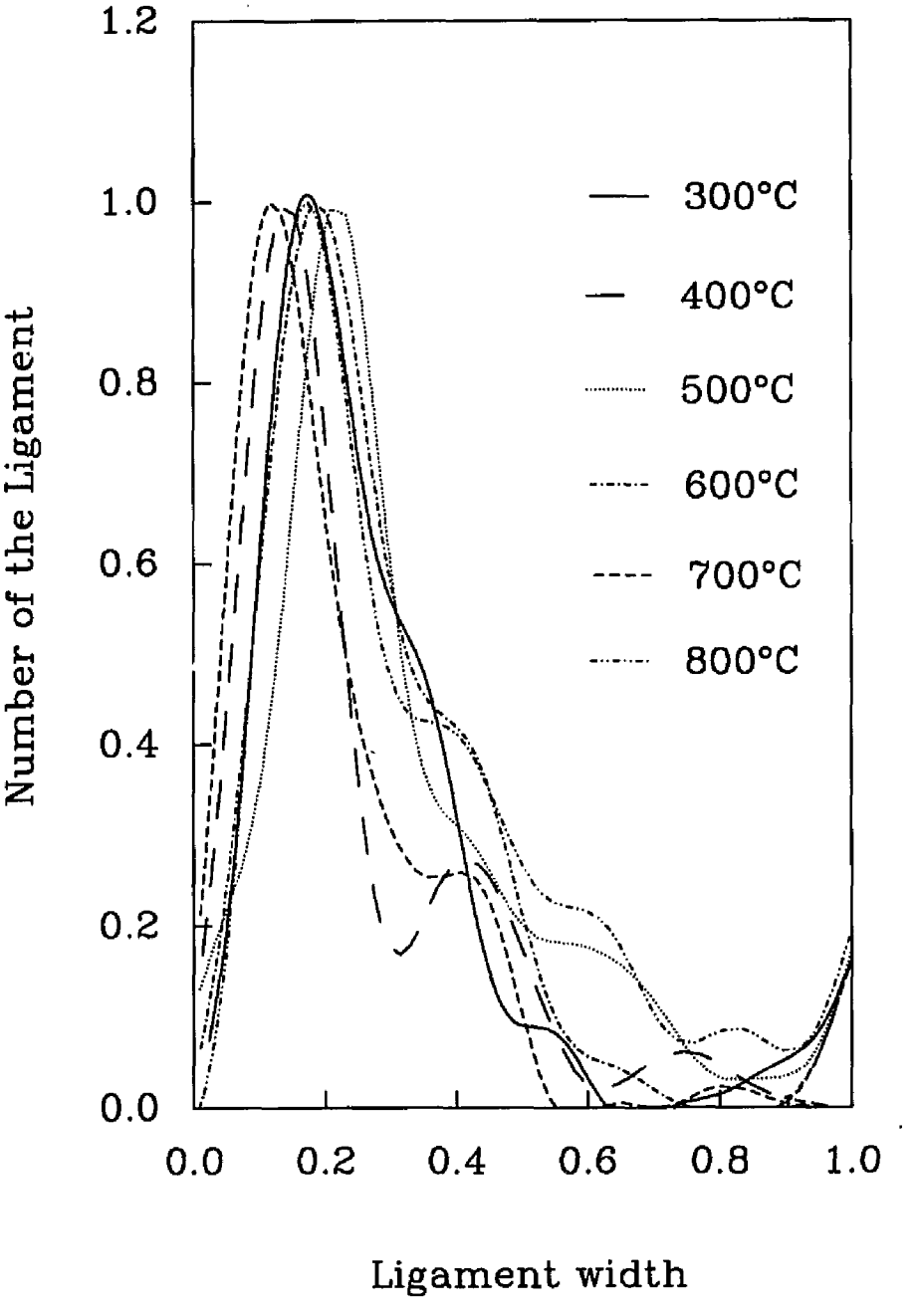

Figure 5.14 The normalized distribution of ligament width of porous Au formed from $Ag_{0.74}$-$Au_{0.26}$ alloy. The alloys were annealed for 10 minutes at the temperatures shown.

5.5.3 Determination of Fine Porosity by Extrapolation

We could no analyze samples with an annealing temperature below 300°C because of the resolution limit of the scanning electron microscope. Plots of Log(N/A) and Log<t> (where N/A is the number of the pores per unit area and <t> is the average ligament width) are linear with temperature, as shown in Figure 5.15 and Figure 5.16, and extrapolation of Log(N/A) to 100°C yields an N/A value of 3000/μm^2. In the other words, the average void size is of the order of 10^3 $Å^2$, and the linear dimension of the voids is of the order of 10 Å. We believe that this extrapolation must be close to the real value. Extrapolation of <t> from Figure 5.16 yields a value of 50 Å for the 100°C sample. The STM image of 100°C sample in Figure 5.8 suggests that the ligament width is ≈ 30Å.

Table (5.1) shows the characteristic of the porous gold made from the 74 atomic percent of Ag and 26 atomic percent of Au alloy, where:

N/A: the average number of the voids per μm^2

<t>: the average ligament width

Table 5.1 Image analysis results of porous Au

Temp. °C	Area μm^2	Perimeter µm	Diameter µm	Length µm	Width µm	Aspect Ratio	<r> µm	N/A μm^{-2}
100	***	***	***	***	***	***	5.000E-3	3000
300	1.13E-3	2.20E-1	4.42E-2	5.39E-2	3.34E-2	1.639	2.354E-2	251
400	2.81E-3	2.41E-1	6.32E-2	8.33E-2	4.75E-2	1.717	8.476E-2	62.5
500	1.12E-2	5.50E-1	1.28E-1	1.59E-1	1.00E-1	1.590	1.148E-1	18.1
600	6.67E-2	1.18	3.35E-1	4.40E-1	2.36E-1	1.839	2.493E-1	3.698
700	1.80E-1	2.01	5.50E-1	7.06E-1	3.87E-1	1.793	5.019E-1	1.408
800	1.72E	7.85	1.89	2.44	1.28	1.946	1.044	0.145

*** Not available.

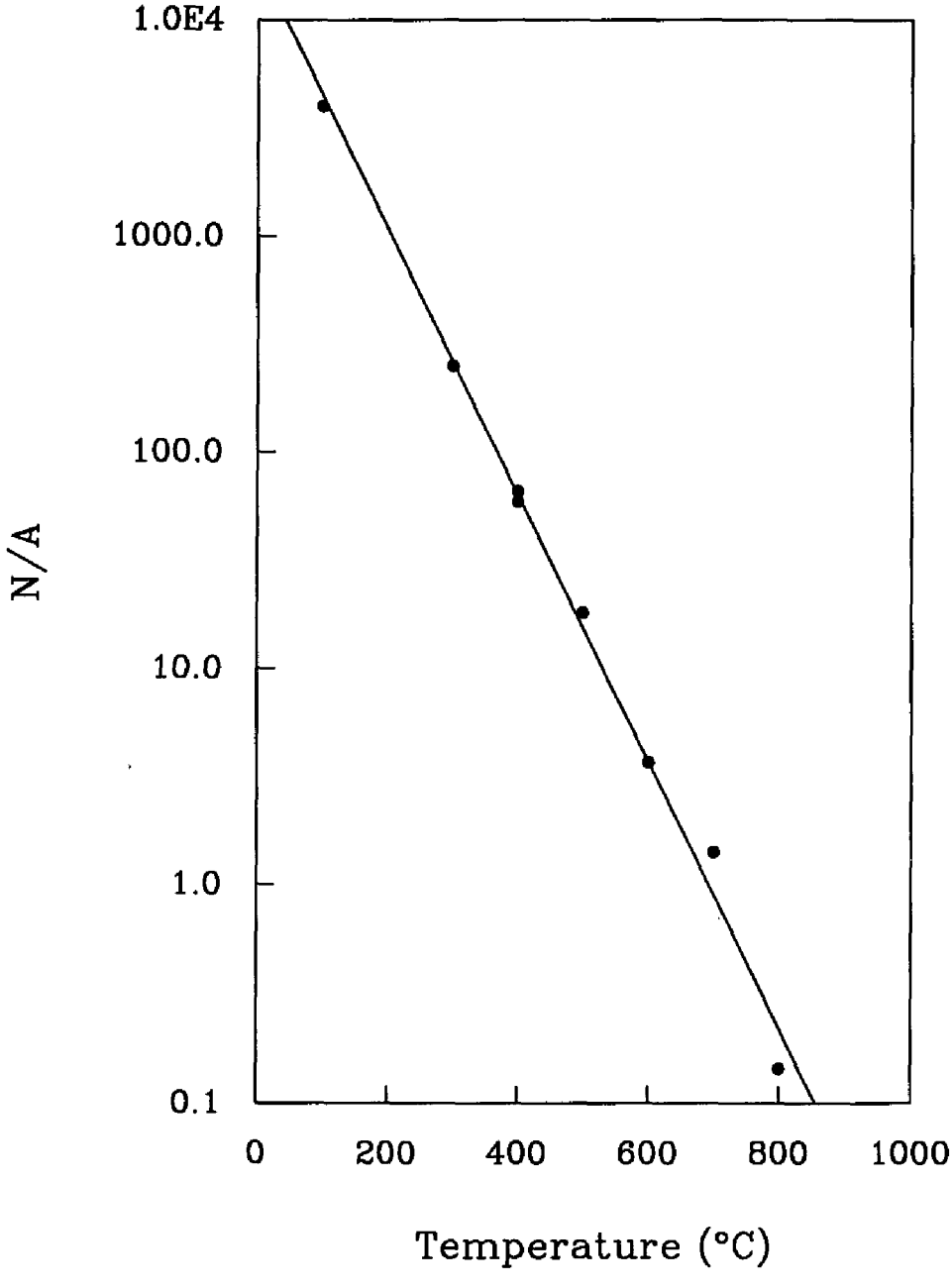

Figure 5.15 Annealing temperatures, T, vs. Log(N/A) from the $Ag_{0.74}$-$Au_{0.26}$ alloy. The last point was obtained by extrapolation.

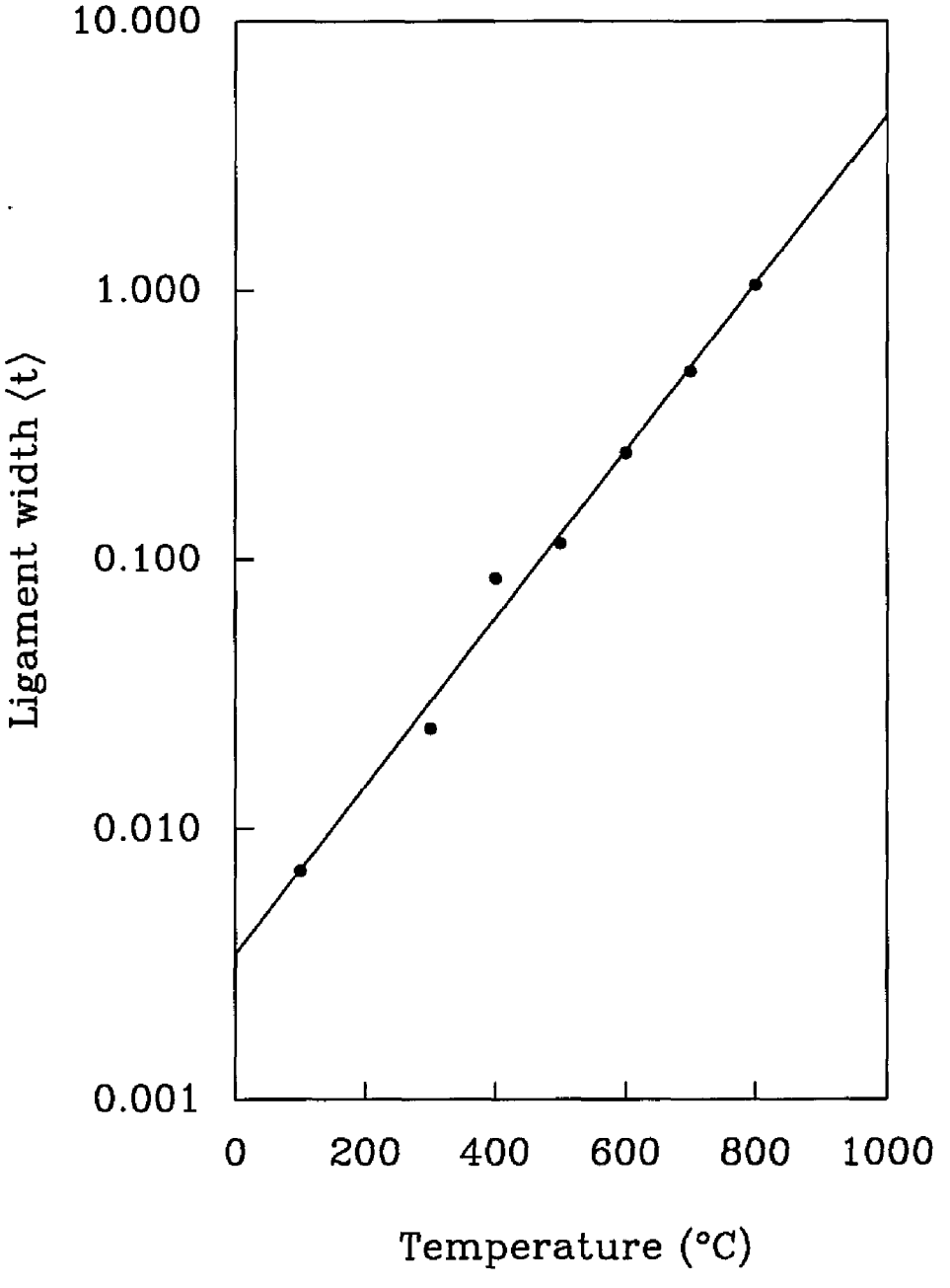

Figure 5.16 Annealing temperature, T, vs. Ligament width, <t>. The last point has been extrapolated.

5.6. Results of the Mechanical Tests

In this section, we present the results of the three-point bend test. Table (5.2) shows the elastic modulus, and the fracture stresses of the samples investigated. Here, k_2 is the force constant of the specimen, E is the elastic modulus, P_f is the fracture load, σ is the fracture stress, δ_f is the displacement of the sample corresponding to P_f or σ in load displacement curve. The energy consumed during the fracture is defined as the area under the load-displacement curve up to the fracture point.

Table 5.2 Mechanical test results of porous Au beam

Sample °C	k_2 dyne/cm	E dyne/cm^2	P_f grams	σ dyne/cm^2	Energy consumed ergs	δ_f cm
100.1	7.86E+05	2.43E+09	8.15	1.15E+07	40	0.0101948
300	8.43E+05	2.23E+09	12.55	1.29E+07	102	0.0159255
300.1	6.55E+05	1.93E+09				
300.2	5.62E+05	1.66E+09	11.25	1.56E+07	108	0.0196268
400.2	3.49E+05	1.08E+09	13.7	1.96E+07	294	0.0436618
400.3	4.72E+05	1.21E+09	14.7	2.22E+07	223	0.0312420
500	3.57E+05	1.14E+09	16	2.40E+07	381	0.0491786
600.1	2.35E+05	9.70E+08	15.9	2.85E+07	562	0.0717868
700.2	.91E+05	7.41E+08	20.2	2.56E+07	1035	0.0705536
700.3	1.84E+05	5.63E+08	13.7	1.90E+07	790	0.1032573
800.1	2.09E+05	5.47E+08	19	2.59E+07	1048	0.1068389
800.2	3.96E+05	1.19E+09	43	6.05E+07	2451	0.1033479

Figure 5.17 shows the elastic modulus, E, as a function of Log(N/A). The normalized value, *i.e*, E_{tmp}/E_{100}, shows that the elastic modulus of 800°C sample is about 23% of E_{100}. As the porous size increase [Log(N/A) decreasing], the modulus of the specimen with the same volume fraction decreases. Stated another way, fracture stress increases as the pore size increases in the sample, as shown in Figure 5.18. Figure 5.19 and Figure 5.20 show that during fracture, a sample with coarser porosity would have undergone a larger displacement and consumed a larger amount of energy than a sample with finer porosity.

Generally speaking, for samples with the same size (length, width, depth) and the same volume fraction, the coarser sample has a lower elastic modulus, a higher fracture stress, has consumed more energy and has undergone a longer displacement. These findings suggest that a coarser sample is more ductile than a finer sample.

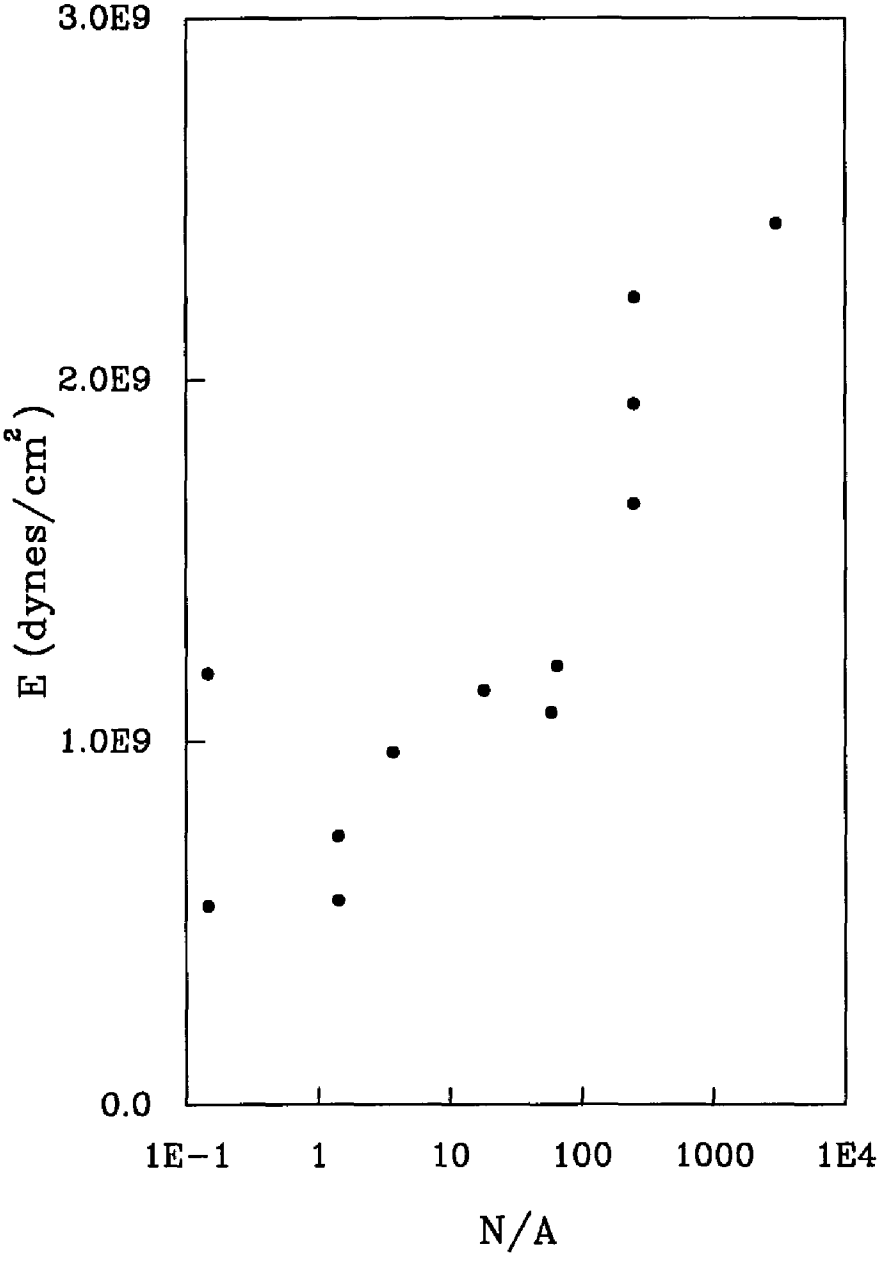

Figure 5.17 Elastic modulus, E, vs Log(N/A) for porous Au.

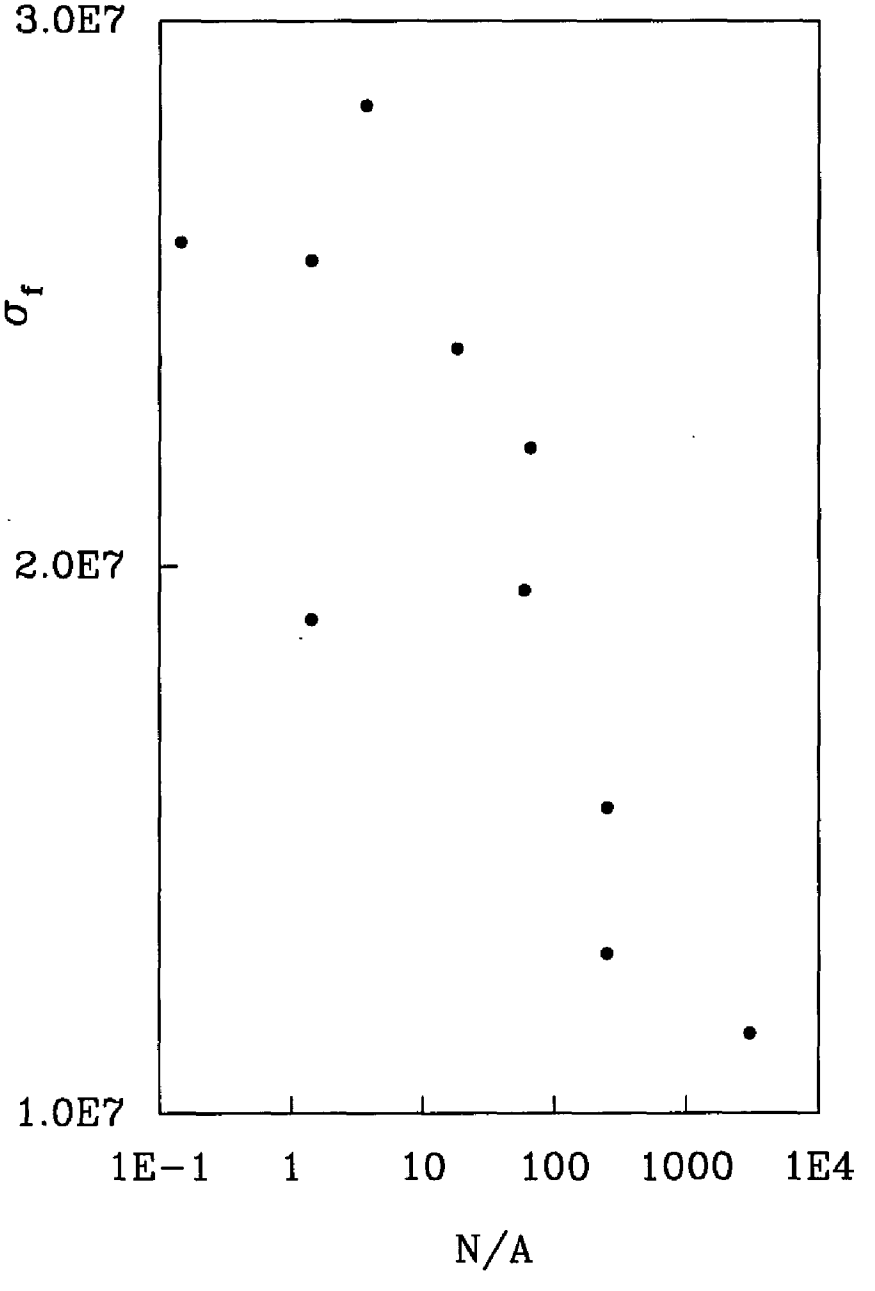

Figure 5.18 Fracture stress, σ_f, vs. Log(N/A) for porous Au.

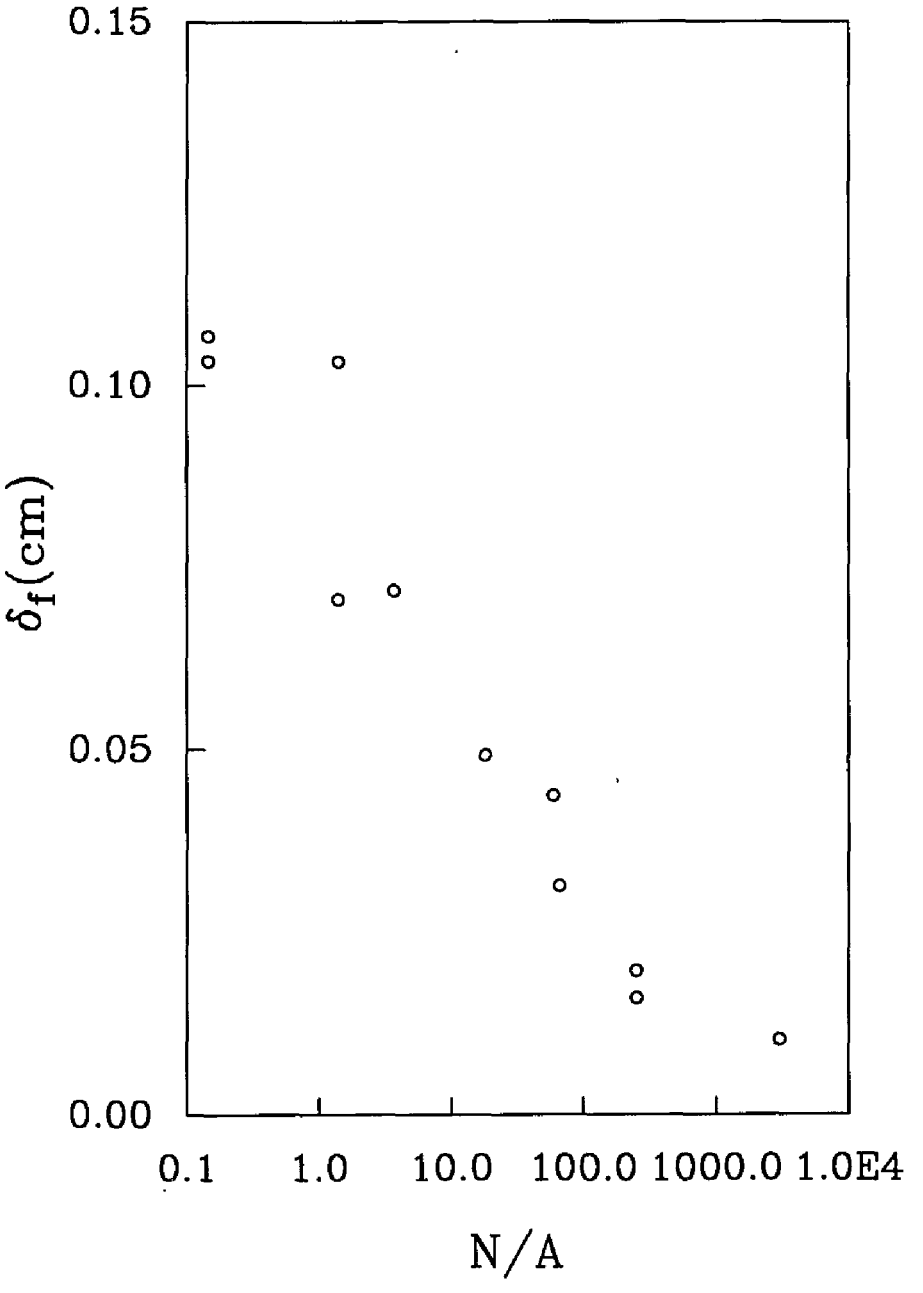

Figure 5.19 Results of the three-point bend tests of displacement, δ_f, corresponding to the maximum load in load displacement curve vs Log(N/A).

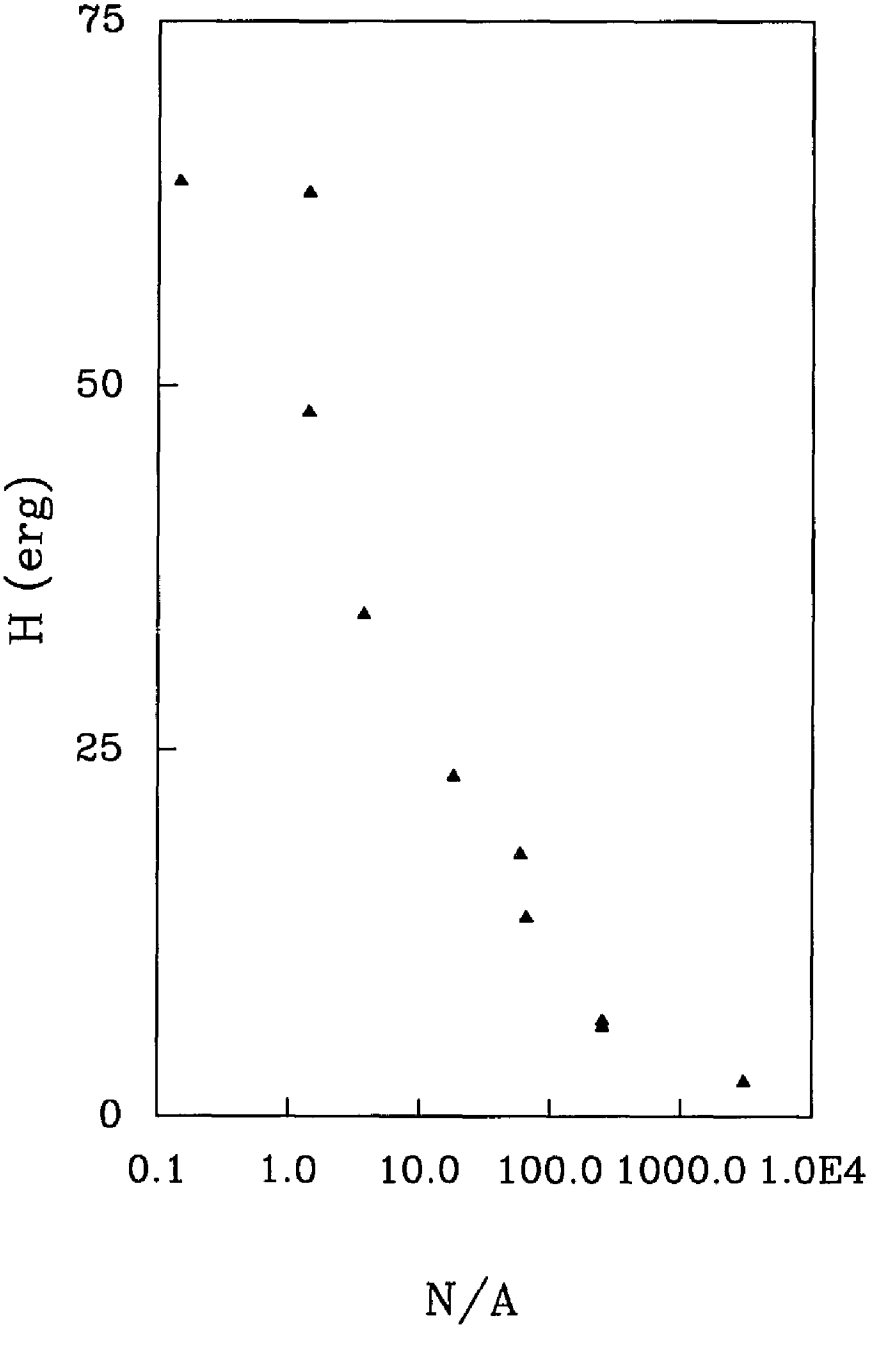

Figure 5.20 Energy absorbed in the fracture process, H, defined as the area under the load displacement curve up to the maximum load vs. Log(N/A).

5.7. Discussion of Results

5.7.1 Elastic Modulus

Maiti, Gibson, and Ashby [64] studied the mechanical properties of the uniform cellular materials shown in Figure 5.21.

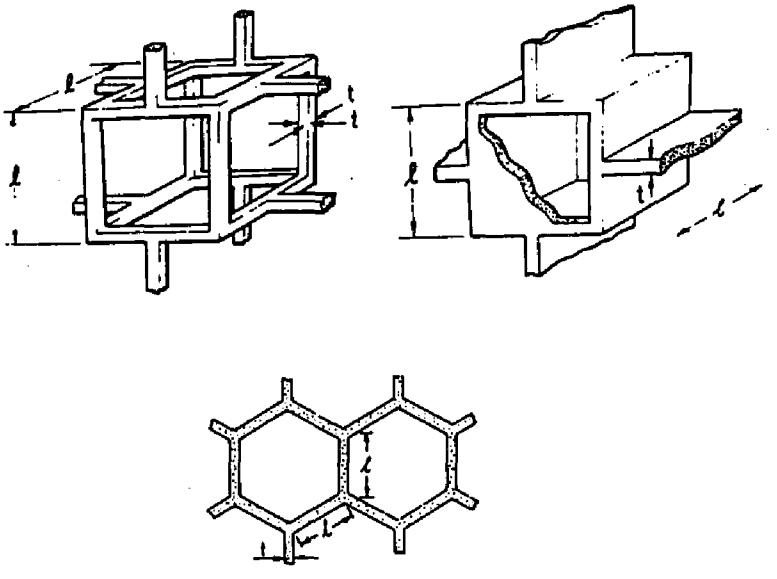

Figure 5.21 Figures of uniform cellular solids [64].

Their experimental results showed that the relation between the elastic modulus and the volume density of cellular materials could be described by:

$$E^*/E_s = C(\rho/\rho_s)^2 \qquad (5.15)$$

where C is a constant, E^* is the Young's modulus of cellular solid, E_s is the Young's modulus of cell-wall material, ρ is the initial density of cellular solid, and ρ_s is the density of cell wall material. The relative density ρ/ρ_s follows from cellular geometry:

$$\rho/\rho_s \propto (t^2 \cdot l/l^3) = (t/l)^2 \qquad (5.16)$$

where t is the ligament width and l is the ligament length (pore size).

Considering two samples with the aspect ratio $a_1=(t_1/l_1)$ and $a_2=(t_2/l_2)$, elastic modulus E_1 and E_2 respectively. According to the results of Maiti *et al*:

$$E_1/E_2 \propto (a_1/a_2)^4 \qquad (5.17)$$

It is apparent from the normalized curves of ligament width and pore size distribution [Figure 5.14 and Figure 5.12] that there are only small differences between the samples. Nevertheless, since the parameter a is raised to the fourth power, small differences in these distributions can lead to significant differences in the Young's modulus. The value of the ratio $E_{400}/E_{800} \approx 2.1$ requires that the variation in a values as measured by the ratio a_{400}/a_{800} should be only 1.2. We do not believe that our image analysis techniques are sensitive enough to discriminate such fine differences, and so we cannot further analyze the results obtained on Young's modulus.

5.7.2 Fracture Behavior

To understand the fracture behavior of a porous solid, we constructed a two-dimensional self-similar cellular system; for simplicity we used a square lattice, where the system was composed of L^2 bonds, where L is the linear dimension of the sample. Each bond has equal length l and equal width t but a different fracture strength, σ.

Following Kahng *et al.* [40], let σ_- and σ_+ represent the minimum and maximum values of the strength of the bonds in the system. We consider that there is a uniform distribution, $N(\sigma)$, of width, ω, of L^2 bonds. As the extended load reaches σ_- the weakest bond in the system fails. There are stresses at the tip of a newly formed crack which are equal to $K\sigma_-$, where K is the stress concentration factor. If $K\sigma_- > \sigma_+$ then this crack necessarily grows and the sample fails in a trivial manner by the growth of a single crack. On the other hand, if $K\sigma_- < \sigma_+$ then the system is stable and further increases in load are required to cause the sample to fail. For a uniform distribution between $\sigma_- = 1-\omega/2$ and $\sigma_+ = 1+\omega/2$, the value of ω at which trivial behavior occurs (ω_0) is given by the condition $K\sigma_- = \sigma_+$ or:

$$K\cdot(1-\omega_0/2) = 1+\omega_0/2 \tag{5.18}$$

Solving for ω_0 yields:

$$\omega_0 = 2\cdot(K-1)/(K+1) \tag{5.19}$$

Consider the situation where $K\sigma_- < \sigma_+$. For a uniform distribution of width ω, all the bonds are uniformly distributed over ω, so that the typical difference between two adjacent breaking strengths will be $\sim \omega/L^2$. The average breaking strength of the nth weakest bonds is then:

$$\langle\sigma_{n-}\rangle \approx \sigma_- + n\cdot\omega/L^2 \tag{5.20}$$

When a crack forms, the total number of crack-tip bonds increases by 2. After n single bonds crack form, in analogy to equation (5.20), the average breaking strength of the weakest 2n edge bonds is:

$$<\sigma_e(n)> = \sigma_. + \omega/(2n) \qquad (5.21)$$

After n cracks form, the stress at the end of each crack is $K<\sigma_{n.}>$. For a stable network:

$$[K<\sigma_{n.}>] < [<\sigma_e(n)>] \qquad (5.22)$$

In the other words, if the stress at the tip of each crack is less than the average breaking strength of the 2n edge bonds, the system is stable. However, as the number of broken bonds increases, the breaking strength of the edge bonds decreases. Equation (5.22) can be solved for the number of bonds, so defining the instability of the sample. For large system, *i.e.*, as L approaches to infinity, the value of n defining the instability is given by:

$$N_c \approx [1/\omega_0 - 1/\omega]\cdot\omega/(2\sigma_.) \qquad (5.23)$$

For a finite L, N_c is given approximately by $L/(2K)^{1/4}$, so that if $N_c/L<1$ "brittle" failure will occur. On the other hand, if $N_c/L>1$ the tendency to fail will be by a gradual or "ductile" separation process. These types of transition occur as a function of the annealing temperature for the porous Au samples examined in this study. The distribution functions characterizing the porous Au samples were self-similar (see Figure 5.12, Figure 5.13 and Figure 5.14). The length scale of the porosity varies considerably from sample to sample and can be used to define an effective sample size

for each sample annealed at a different temperature. This effective sample size is given by L_{tmp}:

$$L_{tmp} = L/\langle l \rangle \tag{5.24}$$

where L is the smallest relevant sample dimension and $\langle l \rangle$ is the average pore diameter in a sample annealed at a particular temperature. We can estimate the number of broken bonds to initiate failure in the porous Au from the load displacement curves. Assume that each broken ligament of average diameter $\langle t \rangle$ requires a displacement g to fail, where $g \sim (A/N)^{1/2}$. Then, the number of broken bonds N_c may be estimated by:

$$N_c \sim \delta_f/g \tag{5.25}$$

where δ_f is the displacement corresponding to the maximum load on the load displacement curve.

Figure 5.22 shows δ_f vs L_{tmp} and Figure 5.23 shows N_c vs L_{tmp} evaluated as described above. The behavior of the ratio N_c/L_{tmp} vs L_{tmp} is shown in Figure 5.24. The double logarithmic plot shows two regions of behavior:

(1) a brittle region where, N_c is independent of the effective sample size, and

(2) a ductile region, where N_c is a decreasing function of L_{tmp}.

In purely brittle case N_c/L_{tmp} is identically 1, as sample failure when a single crack formed which spreads across the sample. In the brittle cracking region, $N_c < L_{tmp}$ or $N_c \approx L_{tmp} + \text{const}$, so that $N_c/L_{tmp} \sim \text{const.}/L_{tmp}$. This expression denotes precisely the behavior we observed, *i.e.*, as L_{tmp} approaches to infinity, the slope of the double logarithmic plot in Figure 5.24 approaches -1.

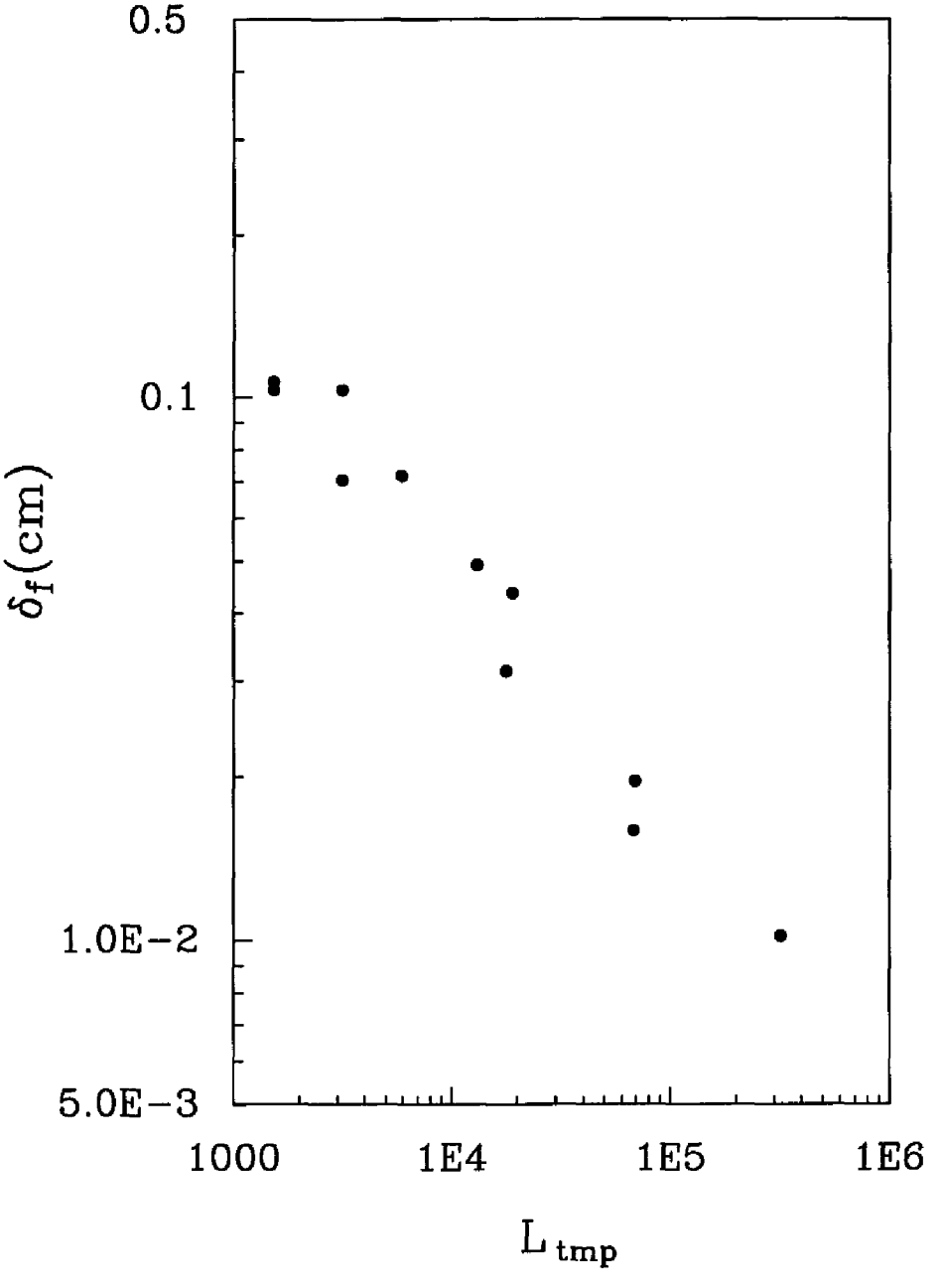

Figure 5.22 Results of the three-point bending tests of the displacement corresponding to the maximum load in load displacement curve, δ_f vs. L_{tmp}.

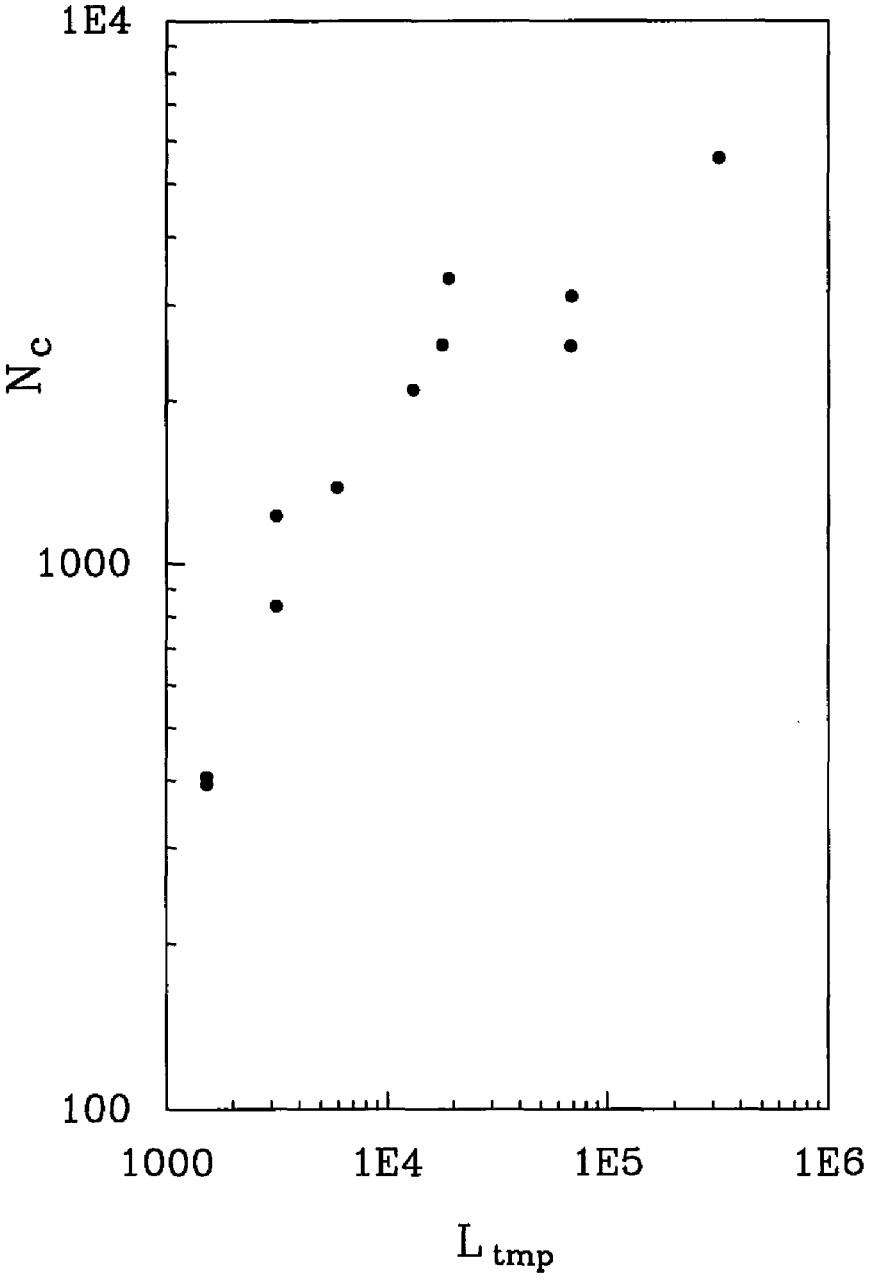

Figure 5.23 The number of the broken bonds which leads to the fracture of the porous Au solid, N_c vs. L_{tmp}.

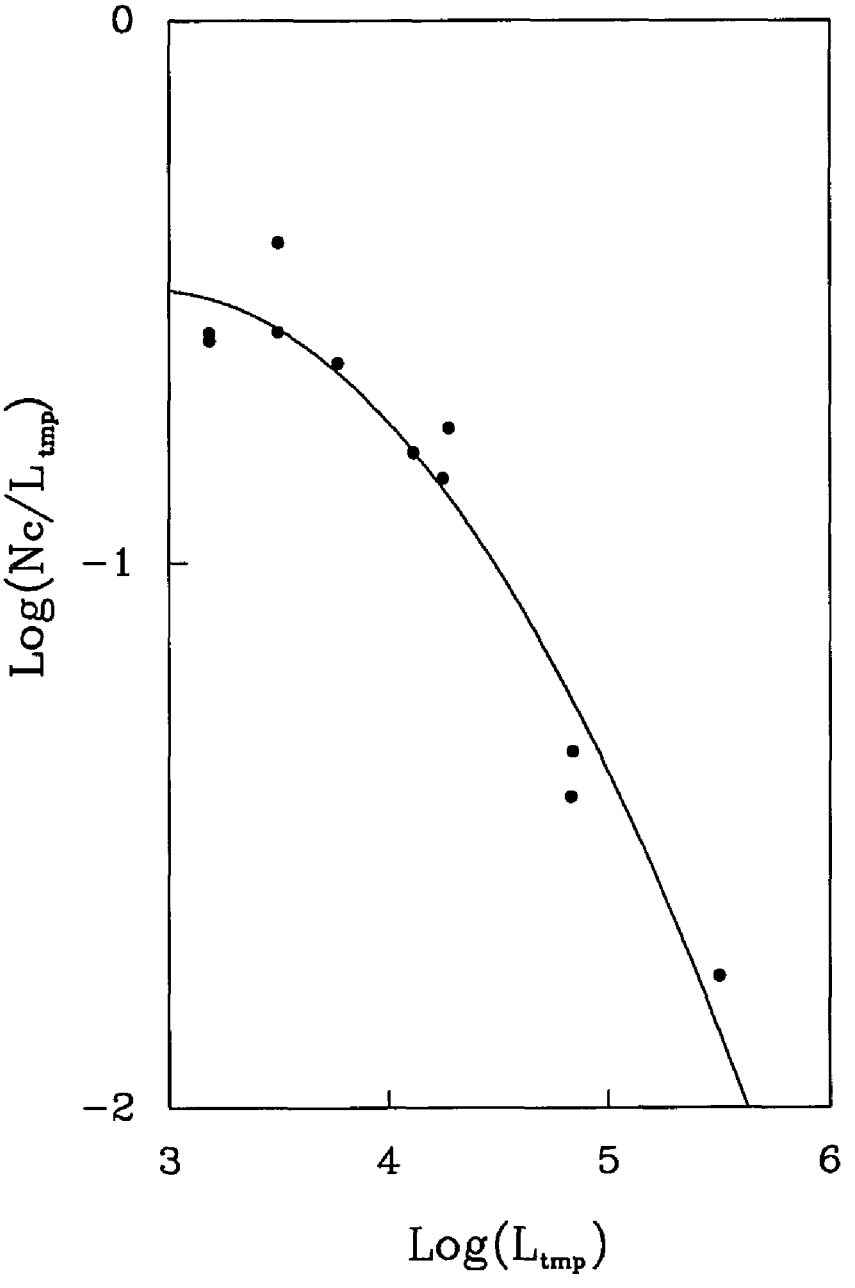

Figure 5.24 A plot of N_b/L_{tmp} vs L_{tmp}.

6. CONCLUSIONS

6.1. 2-D Work

To obtain a detailed understanding of the mechanical properties of a disordered medium or a multiply-cracked body, We used two 2-D models of different configurations with random porosity.

Several methods were used to analyze the experimental results; a modified Griffith relation incorporating an effective medium theory, a Weibull statistic method, and a percolation analysis in the scaling region.

The Griffith energy criterion was applied through the analysis. As we discussed in the review chapter, for metals overcoming the surface tension of the crack surface is not enough to lead the extending of a crack, as much of the work is required to produce a new plastic zone at the tip of an advancing crack. These small plasticity effects do not affect our results since the size of the plastic zones which developed in our 2-D experiments were of the order of the sample thickness, i.e ., the sample was under the small scale-yielding condition.

In the very dilute region, where there are only a few cracks and most of them are of unit crack length, all the cracks are treated as if they were the same length: any crack interactions were ignored. The elasticity and fracture stress could be described by an effective modulus derived from effective medium theory which predicted that in the dilute region, both E and σ decrease linearly with decreasing p. The effective medium theory predicts that $E \sim (1-\alpha\phi)$, with $\alpha \approx 3.6$ for a honeycomb lattice, and ≈ 2 for a square lattice. EMT also predicted that the initial slope of the fracture stress as a function of ϕ should be approximately 3 for a honeycomb lattice, and 1.8 for a square

lattice. As shown in Figure 3.3 and Figure 3.5 , these predictions fit our experimental data quite well.

In the scaling region, where the fraction of remaining bonds, p, is very close to the percolation threshold, the elastic modulus and fracture stress will drop to zero. Percolation concepts in conjunction with the Griffith relation were used to study the behavior of the fracture stress. The experimental results show that the elastic modulus exponent, $f \approx 3.1 \pm 0.2$, which governs the behavior near the percolation threshold are in a good agreement with theoretical and simulation results, which gave approximately 3.5 for the discrete lattice model in 2-D. The fracture exponent, F, agrees with our experimental results, and is 1.7 and 1.8 for a honeycomb lattice and a square lattice, respectively.

Fracture behavior in the dilute and medium dilute region were examined by a statistical Weibull approach. Several assumptions were made:

1. There is no interaction or only the weakest interaction between cracks, so that the effect of the crack in each area element can be analyzed independently of that in any other area element as if it were the only crack existing in the medium.
2. The strength of an area element is related to the severity of the crack it contains by Griffith's theory of crack instability.
3. The strength of any specimen is uniquely defined by the strength of that area that contains the most severe crack.

The fracture behaviors of the system can be identified by the α value, which describes the dispersion of crack size distributions of the specimen; the larger the α, the more uniform the distribution and the more brittle the solid. There is a brittle-to-ductile transition as cracks are generated gradually at random in solids. At the very beginning, each new cut tends to create a new crack instead of connecting two smaller ones or extending a single crack. The cracks are almost the same size and uniformly distributed in the solid, and the fracture behavior is brittle because of the large α value. As the

number of the cracks increases, some of the smaller cracks will be linked by the new cut, forming larger cracks, and the size distribution of the cracks will broaden. The fracture behavior, then, is considered to be less brittle or ductile and this change is reflected in the small α value. According to our assumption and the results of our analysis, there is a brittle-to-ductile transition in the fracture behavior of both 2-D systems, and this transition could identified by the degree of dispersion in the distribution of crack size.

6.2. 3-D Work

This experiment involved a unique technique to prepare specimens for a three-point bend test, namely an electrochemical dissolution process and a subsequent annealing process which gave porous Au structures. Samples with various pore sizes were characterized by the scanning electron microscope, digital image analysis, and X-ray analysis.

Due to the resolution of the microscope, we could not analyze samples formed below 300°C annealing temperature. The self-similar structure of the samples showed there was a linear relation between temperature and Log(N/A), which allows us to extrapolate the characteristics of samples annealed at lower temperatures.

The results of three-point bend tests showed that samples with larger scale porosity had a lower Young's modulus and a higher fracture stress than samples with finer scale porosity. In addition to these analytical differences in sample behavior, we discovered the existence of a ductile-to-brittle transition. We believe that this transition is related to the effect of finite sample size. The fracture properties of the porous Au were understandable in terms of the recent analysis of Kahng *et. al.* [40].

6.3. Suggestions for Future Work

There are several interesting experiments which could be done to study the mechanical properties of porous solids.

First, for finer porous samples (annealing temperature below 300°C), it might be possible to use STM to examine their structure, especially for the samples formed at room temperature.

Fracture behavior is sensitive to both ligament distribution and to the sample's size. The latter effect could be examined by varying the macroscopic size of the sample; for our 3-D samples the linear dimension was 1.5 mm, but it is possible to make it smaller. With four orders of magnitude of variation in the ligament or voids size and three orders of magnitude of variation in the sample size, the brittle-to-ductile transition would be clearer.

Also, the voids size and shape can be altered by controlling annealing temperature and annealing time. We found that the porous structure could be either a channel-island structure (as we having), or a Swiss-cheese structure, depending upon the annealing time. These two different structures represent the discrete and continuum models of the percolating system, respectively.

We kept the volume fraction as a constant in all of our samples. One might use an alloy of different composition, such as 50 atomic percent of Ag, and so on. In this case, we could examine the mechanical properties of the samples with similar porous structure but with different volume fraction.

In our samples, the porous structure was similar, from the 100°C sample to the 800°C sample. If samples were annealed at different temperatures and then sintered, we would obtain a specimen with a wide distribution of voids size (or ligament width, length) that would open many new prospects for study.

7. REFERENCES

1. M. C. Smith, Principles of Physical Metallurgy, Harper & Brothers Publisher, New York, (1956).

2. D. Mclean, Mechanical Properties of Metals, John Wiley and Sons, Inc., New York, (1962).

3. R. W. Cahn, Physical Metallurgy, John Wiley and Sons, Inc., New York, (1965).

4. A. S. Argon, Mechanical Behavior of Materials, Addison-Wesley Publishing Company, Inc., MA., USA, (1966).

5. G. E. Dieter, Jr., Mechanical Metallurgy, McGraw-Hill Book Company, New York, (1986).

6. D. Broek, Elementary Engineering Fracture Mechanics, Martinus Nijhoff Publishers, Dordrecht, (1974).

7. M. M. Eisenstadt, Introduction to Mechanical Properties of Materials, Macmillan Company, New York, (1971).

8. A. M. Freudenthal in Fracture Vol. 2, edit by H. Liebowitz, Academic Press, N.Y., N.Y. (1968) pp. 592-618

9. R. J. O'Connell and B. Budiansky, Journal of Geophysical Research, **79**, 5412, (1974).

10. D. Stauffer, Introduction to Percolation Theory, Mid-County Press, London, (1985).

11. H. E. Stanley, On Growth and Form, Martinus Nijhoff Publishers, Dordrecht, (1986).

12. E. Orowan, Welding Journal, **34**, 1575 (1955)

13. B. Budiansky, J. Mech. Phys. Solids, **13**, 223 (1965)

14. B. Budiansky and R. J. O'Connell, Int. J. Solid Struct., **12**, 81, (1976)

15. M. Kachanov, Int. J. Fracture, **28**, r11, (1985)

16. M. Kachanov, International Journal of Solid and Structure, **23**, 23, (1987).

17. R. Hill, J. Mech. Phys. Solids, **13**, 213, (1965)

18. R. Zallen, The Physics of the Amorphous Solids, John Wiley & Sons, Inc., New York, (1983).

19. V. K. S. Shante and Scott Kirkpatrick, Advances in Physics, **20**, 325 (1971)

20. Y. Kantor, J. Phys. A: Math. Gen. **17**, L843, (1984)

21. P. G. deGennes, J. Physique Lett., **37**, L1, (1976)

22. Y. Kantor and I. Webman, Phys. Rev. Lett., **52**, 1891, (1984)

23. B. I. Halperin, S. Feng and P.N. Sen, Phys. Rev. Lett, **54**, 2391, (1985)

24. D. Sornette, J. Physique, **48**, 1843 (1987)

25. D. J. Bergman, Phys. Rev. B., **31**, 1696, (1985)

26. D. J. Bergman and Y. Kantor, Phys. Rev. B. **53**, 551, (1984)

27. S. Feng and P. N. Sen, Phys. Rev. Lett., **52**, 216 (1984)

28. S. Feng, P. N. Sen, B. I. Halperin and C. J. Lobb, Phys. Rev. B, **30**, 5386 (1984)

29. S. Feng and M. Sahimi, Phys. Rev. B, **31**, 1671, (1985)

30. S. Feng and M. Sahimi, Phys. Rev. B. **31**, 276, (1985)

31. S. Feng, M. F. Thorpe and E. Garboczi, Phys. Rev. B, **31**, 276, (1985)

32. P. Ray and B. K. Chakrabarti, J. Phys. Rev. C., **18**, L185, (1985)

33. P. Ray and B. K. Chakrabarti, Solid State Communications, **53**, 477, (1985)

34. C. J. Lobb and D. J. Frank, J. Phys. C., **12**, L827, (1979)

35. A. Gilabert, C. Vanneste, D. Sornette and E. Guyon, J. Physique, **48**, 763, (1987)

36. P. M. Duxbury, P. D. Beale and P. L. Leath, Phys. Rev. Lett, **57**, 1052, (1986)

37. P. D. Beale and D. J. Srolovitz, Phys. Rev. B. **37**, 5500, (1988)

38. P. D. Beale and P. M. Duxbury, Phys. Rev. B., **37**, 2785, (1988)

39. M. D. Stephens and M. Sahimi, Phys. Rev. B, **36**, 8656, (1987)

40. B. Kahng, G. G. Batrouni, S. Redner, L. de Arcangeli, H. J. Herrmann, Phys. Rev. B., **37**, 7625, (1988)

41. L. Benguigui, Phys. Rev. Lett., **53**, 2028 (1984)

42. L. Benguigui, P. Ron and D. J. Bergman, J. Physique **48**, 1547 (1987)

43. L. C. Allen, B. Golding, and W. H. Haemmerle, Phys. Rev. B., **37**, 3710, (1988)

44. D. Deptuck, J. P. Harrison and P. Zawadzki, Phys. Rev. Lett, **54**, 913, (1985)

45. K. Sieradzki and R. Li, Phys. Rev. Lett., **56**, 2509, (1986)

46. J. Aboudi and Y. Benveniste, Engineering Fracture Mechanics, **26**, 171, (1987)

47. A. P. Poorman, Strength of Materials, McGraw-Kill Book Company, Inc., New York, (1945).

48. A. J. Fenner, Mechanical Testing of Materials, Philosophical Library Inc., New York, (1965).

49. H. H. Uhlig, Corrosion and Corrosion Control, John Wiley & Sons Inc., New York, (1971).

50. J. O. Bockris and A. K. N. Reddy, Modern Electrochemistry, Plenum Press, New York, (1970).

51. J. I. Gardiazåbal and J. R. Galvele, J. Electrochem. Soc., 255, (1980)

52. H. W. Pickering and C. Wagner, J. Electrochem. Soc., 696, (1967)

53. M. S. Fontana, Corrosion Engineering, McGraw-Hill Inc., New York, (1967).

54. R. P. Tischer and H. Gerischer, Zeitschrift für Elektrochemic, **62**, 50, (1958)

55. A. J. Forty and P. Durkin, Phil. Mag. A., **42**, 295, (1980)

56. A. J. Forty, Phil. Mag. A. **43**, 171, (1981).

57. P. M. Hansen, Constitution of Binary Alloy (Metallurgy and Metallurgical Engineering Series), McGraw-Hill Inc., New York, (1958).

58. B. P. Elliott, Constitution of Binary Alloys, First Supplement, (Material Science and Engineering Series), McGraw-Hill Inc., New York, (1965).

59. H. W. Pickering, Corrosion Science, **23**, 1107, (1983)

60. H. W. Reddick and F. H. Miller, Advanced Mathematics for Engineering, John Wiley & Sons, Inc., New York, (1955).

61. L. C. Urquhart, Civil Engineering Handbook, McGraw-Hill Inc., New York, (1940).

62. O. W. Eshbach, Handbook of Engineering Fundamentals, John Wiley & Sons, Inc., New York, (1952).

63. IPP Operator's Manual, (Tracor Northern Series II X-Ray Analyzer Manual), Tracor Northern, Inc. Wisconsin, USA., (1987).

64. S. K. Maiti, L. J. Gibson and M. F. Ashby, Acta Metall. **32**, 1963, (1984)